Seasonal Variability of Microseism Sources: Characterization and Impact on Noise Correlation

with the aim of achieving a doctoral degree

at the Faculty of Mathematics, Informatics and Natural Sciences

Department of Earth System Sciences

at University of Hamburg

submitted by

Mahsa Safarkhani

Hamburg, 2025

Department of Earth Sciences	
Date of Oral Defense:	02.07.2025
Reviewers:	Prof. Dr. Céline Hadziioannou Prof. Dr. Jean-Paul Montagner
Members of the examination commission:	Chair Prof. Dr. Conny Hammer Prof. Dr. Céline Hadziioannou Prof. Dr. Jean-Paul Montagner PD Dr. Habil. Stefanie Donner PD Dr. Thomas Pohlmann
Chair of the Subject Doctoral Committee	
Earth System Sciences:	Prof. Dr. Hermann Held
Dean of Faculty MIN:	Prof. DrIng. Norbert Ritter

Hiermit erkläre ich an Eides statt, dass ich die vorliegende Dissertationsschrift selbst verfasst und keine anderen als die angegebenen Quellen und Hilfsmittel benutzt habe. Sofern im Zuge der Erstellung der vorliegenden Dissertationsschrift generative Künstliche Intelligenz (gKI) basierte elektronische Hilfsmittel verwendet wurden, versichere ich, dass meine eigene Leistung im Vordergrund stand und dass eine vollständige Dokumentation aller verwendeten Hilfsmittel gemäß der Guten wissenschaftlichen Praxis vorliegt. Ich trage die Verantwortung für eventuell durch die gKI generierte fehlerhafte oder verzerrte Inhalte, fehlerhafte Referenzen, Verstöße gegen das Datenschutz- und Urheberrecht oder Plagiate.

Ort, Datum

Unterschrift

Abstract

Microseisms are the most persistent and continuous seismic signals on Earth, generated primarily by oceanic processes. These signals arise from two distinct mechanisms, defining the link between primary and secondary microseisms. Previous research has demonstrated that continuous seismic noise records can be effectively used to extract information about the Earth's subsurface. Specifically, cross-correlation of ambient seismic noise between two stations allows for the approximation of Green's function, offering insights into seismic wave propagation.

A key focus of this thesis is the characterization of microseism sources from multiple perspectives. First, we investigate their contribution to cross-correlation wavefields between station pairs, addressing the question of whether microseisms influence the coda of correlation wavefields. Our findings confirm that oceanic source regions and their seasonal variations are imprinted throughout the coda, challenging the conventional assumption that the coda consists purely of scattered waves. This suggests a need to reconsider how coda waves are interpreted in noise-based seismic applications.

Another major aspect of this research is the improved understanding of microseism sources and their generation mechanisms. Using well-established three-component seismic array beamforming, we analyze the locations of dominant Rayleigh and Love wave microseism sources in two different regions, the United States and Europe across both primary and secondary microseism bands. Additionally, with the increasing demand for full ground motion analysis, we evaluate the potential of array-derived rotation methods for microseism studies. A comparative analysis suggests that array-derived rotation can be effectively applied to microseism source characterization. By examining the regions of study in the United States and Europe, this research further explores the distinct microseism generation mechanisms of the North Pacific and North Atlantic Oceans. These findings are particularly relevant for future developments in seismic monitoring based on microseism recordings.

Contents

1	Intr	oducti	ion	1
	1.1	Ambie	ent seismic noise origin	4
	1.2	Ocean	ic microseisms	5
		1.2.1	Primary microseism	6
		1.2.2	Secondary microseism	7
		1.2.3	Seasonal variation	10
	1.3	Ambie	ent seismic noise interferometry	13
		1.3.1	Correlation wavefield application	15
2	The	ory an	nd Methods	18
	2.1	Correl	lation technique	18
	2.2	Pre-pr	rocessing correlation computation	20
		2.2.1	Time-domain normalization	20
			2.2.1.1 One-bit normalization	21
			2.2.1.2 Running average normalization	21
		2.2.2	Frequency-domain normalization	22
		2.2.3	Retrieving the reference correlation wavefields	23
	2.3	Beamf	forming	24
		2.3.1	Single-component beamforming	26
		2.3.2	Three-component beamforming	27
	2.4	Rotati	ional seismology	29
		2.4.1	Array-derived rotation	32
		242	Rotational beamforming	33

3	Dat	a availability	37
	3.1	Data availability for correlation wavefield	37
		3.1.1 Data availability for single-component beamforming	39
	3.2	Data availability for three-component beamforming	40
	3.3	Data availability for rotational beamforming	42
4	Imp	orints of microseism noise sources on coda of the correla-	
	tion	wavefield	44
	4.1	Continuous isolated noise sources induce repeating waves in the	
		coda of ambient noise correlations	45
	4.2	Imprints of time-dependent microseism source distributions on	
		the coda of correlations (Journal Submission) $\ \ \ldots \ \ \ldots \ \ \ldots$	46
	4.3	Introduction	48
	4.4	Method	50
		4.4.1 Approach	50
		4.4.2 Beamforming	52
	4.5	Results	53
		4.5.1 Beamforming on different correlation windows	53
		4.5.2 Temporal variation of correlations' coda: impact of sea-	
		sonal ocean microseism variation	56
		4.5.3 Influence of the master station	57
	4.6	Discussion	59
	4.7	Conclusion	64
5	Seas	sonal variations in Rayleigh and Love waves: A compari-	
	son	of Pacific and Atlantic oceans	66
	5.1	Seasonality of microseisms in southern California from 6C ground	
		motions	66

	5.2	A com	aparison of Pacific and Atlantic oceans	68
		5.2.1	Introduction	68
		5.2.2	Method	69
		5.2.3	Results	70
			5.2.3.1 Array-derived rotation (United States)	70
			5.2.3.2 Three-component beamforming (United States)	73
			5.2.3.3 Array-derived rotation (Europe)	76
			5.2.3.4 Three-component beamfomring (Europe)	78
		5.2.4	Discussion	80
		5.2.5	Conclusion	84
6	Sun	nmary	and Outlook	85
\mathbf{A}	Sup	pleme	ntary material	89
	A.1	Contin	nuous isolated noise sources induce repeating waves in the	
		coda c	of ambient noise correlations	89
		A.1.1	Introduction	91
		A.1.2	Beamforming the correlation wavefield	93
		A.1.3	A repeating impulsive isolated noise source	95
		A.1.4	Continuously acting isolated noise sources	101
		A.1.5	Discussion	104
		A.1.6	Conclusion	112
	A.2	Season	nality of microseisms in southern California from 6C ground	
		motion	ns	115
		A.2.1	Introduction	117
		A.2.2	Methods	119
			A.2.2.1 Azimuth estimation of surface waves from a	
			single 6C observation	119
			A.2.2.2 Azimuthal seismic anisotropy from 6C ampli-	
			tude measurements	120
		A.2.3	Data	121
		191	Roculto	199

	A.2.4.1	Atmospheric pressure effect on array-derived
		rotational motions
	A.2.4.2	Seasonal azimuth variation of microseismic sources 126
A.2.5	Discussi	on
	A.2.5.1	Local seismic anisotropy by seasonal azimuth
		variations
	A.2.5.2	Origin of microseismic Rayleigh and Love wave
		sources
A.2.6	Conclusi	ion

List of Figures

1.1	Seismic noise spectrum for the vertical recorded at the seismic	
	station IN.SK04. Power Spectral Density (PSD) plot illustrating	
	the characteristics of seismic background noise. The color bar	
	indicates the probability distribution of noise across different	
	frequencies. NHNM represents the New High Noise Model, while	
	NLNM denotes the New Low Noise Model. The upper and lower	
	white dotted lines correspond to the 10th and 90th percentiles	
	of the PSD. The black dashed, dotted, and solid lines depict the	
	mean, median, and mode of the PSD, respectively. The upper	
	and lower solid green lines define the maximum and minimum	
	PSD envelopes (Uthaman et al., 2022)	4
1.2	(a) Power spectral density for 3 days in 2021 recorded at the	
	GRA1 broadband seismic station in the Gräfenberg array in	
	Germany. (b) Location of the station	5
1.3	Cartoon illustrating (a) the primary microseism generation mech-	
	anisms. Where ocean waves interact with the seafloor. This	
	process primarily occurs in shallow waters and is driven by the	
	direct impact of ocean wave energy on the seabed. (b) The	
	secondary microseism with meeting of two trains of ocean waves	
	in opposite directions and with the same frequency. (Ebeling,	
	2012)	7

1.4	Schematic of wave conditions in noise-generating situations. (a)	
	Storm 1 is rapidly moving so that waves generated at C become	
	swell that can meet the wind-sea at point A' . In this case, the	
	noise generated by the local wind-sea alone at point C (class	
	I: wind-generated waves with a wide directional spectrum) can	
	be much stronger at point A' because of the wider directional	
	distribution. (b) Noise generated when waves reflect off the	
	coast (class II: coastal reflection), and (c) noise generated when	
	waves from two distinct storms cross, here at point A (class III:	
	the interaction of two independent wave systems; Ardhuin et al.	
	(2011))	9
1.5	Swell wave height output from the WAVEWATCH III model for	
	12 months of 2019	11
1.6	Seasonal variation of the location of P wave seismic noise sources	
	in the secondary microseismic band (0.1–0.3 Hz). Landès et al.	
	$(2010) \ldots \ldots$	12
1.7	(a) Two years stacking of the correlation wavefield between	
	IV.BRMO-GR.GRA1. Considerable asymmetry in amplitude	
	can be observed in the positive and negative elapsed time sides.(b)	
	the location of two regional scale seismic stations, IV.BRMO in	
	the Italian seismic array and GR.GRA1 in the Gräfenberg array	
	in Germany, with a distance between stations of 700 km	15
2.1	Isotropic distribution of noise sources surrounding stations lo-	
	cated at \mathbf{X}_A and \mathbf{X}_B . The thick dashed lines represent the	
	Fresnel zones. (b) Cross-correlation of the recorded responses at	
	the receiver locations, where the primary contributions originate	
	from sources within the Fresnel zones, marked by the dashed	
	vertical lines. (c) Summation of the cross-correlations shown in	
	(b).(Wapenaar et al., 2010)	19

2.2	Schematic illustration of a plane wave emitted from a source	
	(red star) propagating across the seismic array (black triangles).	
	Due to a specific slowness, the wavefield reaches each station at	
	different times. (a) The incidence angle (i) of the incoming plane	
	wavefront is defined in the vertical plane, while the backazimuth	
	(θ) is defined in the horizontal plane. Incoming plane wavefront	
	is indicated by green dashed lines. Adapted from Schweitzer	
	et al. (2012)	24
2.3	Three types of motion for solid particles in classic elasticity. (a)	
	Translational motion, (b) deformation, and (c) rigid rotational	
	motion. solid line, original body; Dot line, new body shape	29
2.4	Rotational motions induces by Rayleigh (yellow line) and Love	
	(red line) waves (Kislov and Gravirov, 2021)	35
3.1	The location of the Gräfenberg array in Germany (purple tri-	
	angles) along with six single master stations distributed across	
	different azimuthal ranges (yellow markers). The master stations	
	are located in Italy (IV.BRMO, IV.MESG), Poland (PL.OJC),	
	France (FR.CLF), Finland (FN.OUL), and Portugal (PM.PESTR).	38
3.2	(a) Geometry of the Gräfenberg seismic array, consisting of 13	
	broadband stations with three components and an aperture of	
	100 km. (b) Schematic representation of the cross-correlation	
	computation, where PL.OJC is considered as the master station	
	(virtual source), and the stations within the Gräfenberg array	
	act as receivers	38
3.3	Two years reference cross correlations computed between master	
	stations and GRA1 station in Gräfenberg array. This signal	
	filtered in the Secondary microseism frequency band (0.1-0.3 Hz)	39

3.4	Arrays used for the three-component beamforming method: (a)	
	The NOA array in Norway which consists of multiple three-	
	component stations with subset arrays. Each sub-array is	
	equipped with one three-component broadband sensor, with	
	an aperture diameter of 73.9 km (b) A combination of 21 three-	
	component broadband stations from the CI and AZ networks in	
	California, with a total aperture of 173.9 km	41
3.5	Arrays used for the Array-Derived Rotation (ADR) method: (a)	
	The ARCES array in Norway, consisting of four three-component	
	stations with an aperture of 1.7 km. (b) The Piñon Flat array	
	in California, comprising 13 three-component stations with an	
	aperture of 1.08 km	43
4.1	The Gräfenberg seismic stations (depicted by purple triangles)	
	are located in Germany, while the master stations (depicted by	
	yellow triangles) are in Poland (PL.OJC), Finland (FN.OUL),	
	France (FR.CRF), Portugal (PM.PESTR), and Italy (IV.MESG,	
	IV.BRMO). The upper and lower inside panels feature a zoomed-	
	out and zoomed-in view of the seismic array, its location, and	
	geometry.	50

4.2 Distribution of maximum beam power values for slowness and back azimuth grid searches. (a) illustrates the reference noise correlation function (NCF) used as the primary signal for the beamforming method. The grey shadows represent the 10 minute windowing function centered around the direct Rayleigh waves and later parts of the correlation wavefield. The windows are labelled according to the wavetypes in the correlation wavefield, consisting of the "Direct Arrival", "Early Coda", "Mid Coda" and "End Coda" on both casual and acasual elapsed time sides. Panels (b) and (c) demonstrate the distribution of back azimuths and slowness that correspond to the maximum value of beam power in each sliding window (160 seconds) using the beamforming process. Red dashed lines illustrate the converging and diverging wavefield between the master station and seismic array (master-receiver) on the positive (ca. 180°) and negative (ca.

4.3	Evaluation of beamforming results on 10-minute correlation wave-	
	field windows within the primary microseism frequency band	
	(0.05-0.1 Hz). Slowness values ranging from 0 to 0.5 s/km are	
	indicated with dashed line circles. This analysis includes all vi-	
	able master station pairs, namely IV.BRMO, PL.OJC, FR.CLF,	
	IV.MESG, FN.OUL, and PM.PESTR. Distinct segments are la-	
	belled to indicate the location of the wavetypes in the correlation	
	wavefields including, the direct arrivals highlighted in gray, early	
	coda, mid coda, and end coda on both positive and negative	
	elapsed time sides. The spatial arrangement/geometry of the	
	Gräfenberg (GR) seismic array and master stations is depicted	
	by red triangles based on azimuth and backazimuth. Based on	
	the master-receiver wavefield contribution, most coherency in	
	Direct arrivals observed in location of master station and GR	
	array in negative and positive lapse time sides. Due to the	
	large distance between the Master stations FN.OUL, IV.MESG, $$	
	PM.PESTR and GR array, the direct arrival is still visible in the	
	early coda segment even though it arrives after 10 minutes. The	
	upper panel of the figure presents the result of beamforming on	
	the continuous raw data recorded within the GR seismic array	
	stations	55
4.4	Seasonal variation of coda correlation wavefields in the secondary	
	microseism band (0.1-0.3 Hz) with respect to the oceanic regime	
	for the IV.BRMO and PL.OJC master stations during summer	
	and winter. Dashed line circles indicate slowness values from 0-	
	$0.5~\mathrm{s/km}.$ The gray window highlights direct arrivals in positive	
	and negative lapse time sides. Non-direct arrivals including early,	
	mid and end coda are titled and red triangles show the geometry	

4.5	Applying correlation beamforming on random/artificial recorded	
	data in the primary frequency band (0.05-0.1 Hz). Dashed	
	line circles indicate the slowness values from 0-0.5 s/km. (a)	
	illustrates the reference noise correlation function (NCF) between	
	the master station recording of random-generated noise and	
	GRA1 station. A 10-minute windowing function was applied	
	to the NCF prior to beamforming, with each window being	
	labelled according to the position of wave types in the correlation	
	wavefield. The beamforming results of dim grey windows are	
	shown in (b)	59
4.6	Seasonal variation shown in the beamforming results of the	
	raw data recordings at 13 stations of the Gräfenberg seismic	
	array within 12 month of 2019 in the secondary frequency band	
	(0.1 - 0.3 Hz). Dashed line circles indicate the slowness values	
	from 0-0.5 s/km. Top panel shows the 6 month related to the	
	boreal summer (i.e. April-September). Bottom panel shows the	
	beamforming results for 6 months related to winter (i.e October-	
	March)	60
4.7	Swell wave height output from the WAVEWATCH III model. in	
	summer (a) and winter (c) 2019. The purple triangle indicates	
	the location of the Gräfenberg seismic array. The distribution of	
	maximum beam power values versus backazimuth is shown for	
	one of the master stations during summer (b) and winter (d).	
	The color map displays the slowness values for maximum beam	
	dots ranging from 0-0.5 s/km in summer and winter	61

5.1	(a) The 30-minute earthquake signal from January 1, 2024, in	
	Japan with a magnitude of M7.5 is displayed.(c) Purple dot	
	shows the location of the earthquake relative to the center of the	
	Piñon Flat array in California (yellow triangle).(b) The results	
	of the rotational beamforming for Rayleigh waves polarization	
	are shown. This is done by calculating the correlation coefficient	
	of the vertical acceleration with the horizontal rotation signals.	
	The black dots in the figures represent the maximum values	
	obtained in each sliding window, while the dashed line indicates	
	the actual back azimuth of the earthquake (309.6°)	71
5.2	The rotational beamforming results for Pinon Flat in the primary	
	microseismic frequency band (0.05–0.1 Hz, 10–20 s) for Rayleigh	
	(a) and Love (b) wave types. The color map illustrates the	
	distribution density of the computed correlation coefficient over	
	backazimuth for a duration of four years (2016.01-0.1–2019.12.01).	72
5.3	The rotational beamforming results for Piñon Flat in the sec-	
	ondary microseismic frequency band (0.1–0.2 Hz, 5–10 s) for	
	Rayleigh (a) and Love (b) wave types. The color map illustrates	
	the distribution density of the computed correlation coefficient	
	over backazimuth for a duration of four years (2016–2020)	73
5.4	The results of three-component beamforming for a combination	
	of stations of AZ and CI arrays in California, specifically the	
	Rayleigh wave (a) and the Love wave (b) for the primary fre-	
	quency band (0.05-0.1 Hz, 10-20 sec), and the Rayleigh wave	
	(c) and the Love wave (d) for the secondary frequency band	
	(0.1-0.2 Hz, 5-10 sec). The color map illustrates the mean of the	
	estimated beam values for a 600-second sliding window over a	
	period of four years (2016.01.01-2019.12.01) for a back azimuth	
	versus slowness (0-0.5 s/km) grid search	74

5.5	The results of three-component beamforming for a combination	
	of stations of AZ and CI arrays in California, specifically the	
	Rayleigh wave (a) and (b), the Love wave (c) and (d) for the	
	primary frequency band (0.05-0.1 Hz, $10\text{-}20$ sec). The color	
	map illustrates the mean of the estimated beam values for a	
	600-second sliding window over a period of four years (2016-	
	2020) for boreal summer (April-December) and boreal winter	
	(December-March) for a back azimuth versus slowness (0-0.5	
	s/km) grid search	75
5.6	The results of three-component beamforming for a combination	
	of stations of AZ and CI arrays in California, specifically the	
	Rayleigh wave (a) and (b), the Love wave (c) and (d) for the	
	secondary frequency band (0.1-0.2 Hz, 5-10 sec). The color map	
	illustrates the mean of the estimated beam values for a 600-	
	second sliding window over a period of four years (2016-2020) for	
	boreal summer (April-December) and boreal winter (December-	
	March) for a back azimuth versus slowness (0-0.5 s/km) grid	
	search	76
5.7	(a) The 30-minute earthquake signal from January 1, 2024, in	
	Japan with a magnitude of M7.5 is displayed.(c) Purple dot shows	
	location of the earthquake relative the center of the ARCES	
	array in Norway.(b) The results of the rotational beamforming	
	for Rayleigh waves polarization are shown. This is done by	
	calculating the correlation coefficient of the vertical acceleration	
	with the horizontal rotation signals. The black dots in the figures	
	represent the maximum values obtained in each sliding window,	
	while the dashed line indicates the actual back azimuth of the	
	earthquake (56.4°)	77

5.8	The rotational beamforming results for ARCES array in the	
	primary microseismic frequency band (0.05–0.1 Hz, 10–20 s)	
	for Rayleigh (a) and Love (b) wave types. The color map	
	illustrates the distribution density of the computed correla-	
	tion coefficient over backazimuth for a duration of four years	
	(2016.01.01–2019.12.01)	77
5.9	The rotational beamforming results for ARCES array in the	
	secondary microseismic frequency band (0.1–0.2 Hz, 5–10 s)	
	for Rayleigh (a) and Love (b) wave types. The color map	
	illustrates the distribution density of the computed correla-	
	tion coefficient over backazimuth for a duration of four years	
	(2016.01.01–2019.12.01)	78
5.10	The results of three-component beamforming for a combination	
	of stations of NOA arrays in Norway, specifically the Rayleigh	
	wave (a) and (b), the Love wave (c) and (d) for the secondary	
	frequency band (0.1-0.2 Hz, 5-10 sec). The color map illustrates	
	the mean of the estimated beam values for a 600-second sliding	
	window over a period of four years (2016-2020) for boreal summer	
	(April-December) and boreal winter (December-March) for a back	
	azimuth versus slowness (0-0.5 s/km) grid search	79
5.11	The results of three-component beamforming for a combination of	
	stations of NOA arrays in Norway, specifically the Rayleigh wave	
	(a) and (b), the Love wave (c) and (d) for the primary frequency	
	band (0.05-0.1 Hz, 10-20 sec). The color map illustrates the mean	
	of the estimated beam values for a 600-second sliding window	
	over a period of four years (2016-2020) for boreal summer (April-	
	December) and boreal winter (December-March) for a back	
	azimuth versus slowness (0-0.5 s/km) grid search	79

5.12	The results of three-component beamforming for a combination	
	of stations of NOA arrays in Norway, specifically the Rayleigh	
	wave (a) and (b), the Love wave (c) and (d) for the secondary	
	frequency band (0.1-0.2 Hz, 5-10 sec). The color map illustrates	
	the mean of the estimated beam values for a 600-second sliding	
	window over a period of four years (2016-2020) for boreal summer	
	(April-December) and boreal winter (December-March) for a back	
	azimuth versus slowness (0-0.5 s/km) grid search	80
5.13	Projection of dominant microseismic noise sources in California	
	arrays. (a) Noise sources estimated for AZ and CI stations in	
	the primary microseism band (10–20 s), focusing on Rayleigh	
	waves. (b) Same as (a) but for Love waves. (c) Noise sources	
	in the secondary microseism band (5–10 s) for Rayleigh waves.	
	(d) Same as (c) but for Love waves estimations were performed	
	using three-component beamforming. This results shows in the	
	same order for Pinon Flat using array-derived rotation method	
	in (e-h) Yellow shading represents boreal summer, while purple	
	shading represents boreal winter	82
5.14	Projection of dominant microseismic noise sources in Norway	
	arrays. (a) Noise sources estimated for NOA stations in the	
	primary microseism band (10–20 s), focusing on Rayleigh waves.	
	(b) Same as (a) but for Love waves. (c) Noise sources in the	
	secondary microseism band (5–10 s) for Rayleigh waves. (d)	
	Same as (c) but for Love waves estimations were performed	
	using three-component beamforming. This results shows in the	
	same order for ARCES sismic array using array-derived rotation	
	method in (e-h) Yellow shading represents boreal summer, while	
	purple shading represents boreal winter	83

A.1	Beamforming the correlation waveheld between the Grafenberg	
	array in Germany (blue triangle) and master station IV.BRMO,	
	Italy (yellow triangle), in the secondary microseism frequency	
	band (0.1 to 0.3 Hz). a) Overview map with master station and	
	array stations. The orange line and purple area correspond to the	
	dominant directions detected by beamforming. b) Beamforming	
	results: sample cross-correlation between the master station and	
	one array station (top), mean Pearson correlation-coefficient of	
	correlation functions with best-fitting beams in each window	
	(second panel), detected direction of arrival (third panel), and	
	estimated phase velocity (bottom). Detected directions corre-	
	spond to the correlation wavefield converging onto and diverging	
	from the master station (orange lines), and a range of directions	
	pointing towards the Atlantic Ocean (purple area)	93
A.2	Same as Figure A.1, but for master station PL.OJC, Poland.	
	The directions detected by beamforming corresponding to the	
	diverging and converging part of the correlation wavefield change	
	with master station as expected (orange lines), whereas the range	
	of directions towards the Northern Atlantic remains constant	
	(purple area). Note that the converging part of the correlation	
	wavefield points towards West, similar to one of the dominant	
	directions detected pointing towards the Atlantic Ocean for	
	master station IV.BRMO (Figure A.1)	94

A.3	A repeating isolated noise source produces repeating direct waves	
	in correlation functions, depicted in time domain. a) Auto-	
	correlation of the wavelet $ W_I ^2$. b) Auto-correlation of the	
	excitation pattern $ E_I ^2$ with a regular 20 sec. interval, excited	
	5 times. Note that amplitudes decay by $1/5$ every interval away	
	from 0 sec. lapse time. c) Cross-correlation of the Green's	
	functions between the isolated noise source and both station	
	locations for an arbitrary geometry. d) Second term of the	
	correlation wavefield (Equation A.3, the convolution of a-c),	
	where each arriving wavelet represents a direct wave emitted	
	from the isolated noise source at \mathbf{r}_N	97
A.4	Schematic illustration of the correlation wavefield in the presence	
	of a repeating impulsive source (5 excitations, 20 sec. interval,	
	same as in Figure A.3). We remove the wavelet for improved	
	clarity. a-g) Snapshots of the correlation wavefield at different	
	lapse times, indicated by dashed lines in h). The contributions	
	of the isolated source (purple lines) and boundary sources sur-	
	rounding the master and array stations (yellow line) propagate	
	through the medium. Line thickness indicates amplitude. h)	
	Correlation function between the array station and the master	
	station, color-coded by isolated source and boundary source con-	
	tribution (purple and yellow, respectively). Dashed vertical lines	
	mark the lapse time snapshots displayed in a-g. The acausal part	
	of the correlation function contains repeating waves propagating	
	from the isolated source and the boundary source contribution	
	converging onto the master station (a-d). At lapse time $\tau = 0$,	
	both the main arrival of the isolated source contribution and the	
	boundary source contribution reach the master station (e). At	
	causal lapse time, the last arrivals of the isolated source reach	
	the array station (f) and finally the diverging contribution of	
	the boundary sources (g)	98

A.5	Beamforming synthetic cross-correlation functions detects re-	
	peating direct waves from the regularly repeating isolated noise	
	source. a) Overview map: master station (orange triangle), ar-	
	ray stations (blue triangle), boundary sources in a small circle	
	surronding the stations (red stars) and the isolated noise source	
	Southwest of Iceland (purple star). b) Beamforming results:	
	sample cross-correlation between master station and one array	
	station, mean correlation-coefficients between windowed corre-	
	lation functions and beams, detected direction of arrival, and	
	estimated phase velocity. The boundary source contribution to	
	the correlation wavefield converging onto and diverging from	
	the master station (orange lines, first term in Equation A.2) is	
	detected as well as repeating direct waves from the isolated noise	
	source (purple line, second term in Equation A.2)	100
A.6	Contribution to the correlation wavefield by a continuously acting	
	isolated noise source. a) Source term for a secondary microseism	
	source, if all harmonics between 0.1 and 0.3 Hz are excited with	
	a uniformly random phase $\Phi_i \in [0, 2\pi)$ and equal amplitude	
	A=1 (Equation A.4). b) Auto-correlation of the source term	
	$ N_I ^2$. c) Convolution of $ N_I ^2$ with the same Green's function	
	cross-correlation as in Figure A.3c, i.e., the second term of the	
	correlation wavefield (Equation A.2), with a main arrival and	
	low-amplitude, repeating direct waves throughout the coda	102
A.7	Same as Figure A.5 but for secondary microseism source terms	
	for both boundary and isolated sources. Both contributions to	
	the correlation wavefield are scaled to have similar amplitudes.	
	Distinct main arrival (the "spurious" arrival) of the isolated	
	noise source at ~ -100 sec. lapse time. For this arrival and	
	throughout the coda, direct waves from the isolated source are	
	detected as most coherent	103

A.8	Same as Figure A.7 but for a cluster of isolated sources. Am-	
	plitudes of the summed isolated noise source contribution is	
	scaled to $1/10$ of the boundary source contribution. No distinct	
	spurious arrival but coda still dominated by repeating direct	
	waves from the isolated noise source cluster	103
A.9	Same as Figure A.8 but for two clusters of isolated noise sources.	
	The additional cluster is placed Northwest of the Iberian Penin-	
	sula. The backazimuth to that cluster is indicated by a purple	
	dashed line (a & b, third panel). Amplitudes of the isolated noise	
	source contribution is scaled to $1/10$ of the boundary source	
	contribution. No distinct spurious arrival. Beamforming detects	
	either of the two clusters at a given lapse time in the coda as	
	dominant.	104
A.10	Impact of pre-processing scheme on the detection of repeating	
	direct waves for master station IV.BRMO. a) Same as Figure	
	A.1b. b) Sample correlation function and beamforming result, if	
	only temporal normalisation is applied. c) Results when both	
	whitening and temporal normalisation are applied. d) Results	
	when neither pre-processing is applied.	109

A.11(a) Schematic diagram of the principle (see Equations 1-3) of
azimuth estimation for a single 6C station. r is the Pearson
correlation coefficient between vertical acceleration and trans-
verse rotation rate. ψ_0 and ψ_1 are the maximum and minimum
values of the first-order partial derivative of r with respect to
ψ , respectively. Ψ is the real backazimuth of surface waves.
(b) Distributions of selected 8 broadband seismic arrays in the
Pinon Flat Observatory. The small array can be regarded as a
virtual 6C station. The maximum aperture of this array is about
500m. (c) PSD of 6C microseisms in the winter (2018.September-
2018.December and 2018.January-2018.February). The double
white arrows indicate the identifiable period range of the ampli-
tude anomaly on PSD. 'R' and 'L' represent the Rayleigh and
Love wave, respectively. 'Pm' and 'Sm' represent the primary
microseisms and secondary microseisms, respectively 123
A.12 Air pressure effect on the amplitude of microseisms. (a) The scat-
ter density spectra between the pressure PSD (dB/Hz) and the
seismic noise PSD (dB/Hz) of two months data (2018. June-
2018.July) in the period range of 10-20s. The coherence
(Coh<0.1) between pressure and acceleration (A) is much smaller
than the coherence (Coh >0.4) between pressure and rotational
rate (Ω) . (b) Coherence comparison between acceleration-
pressure (left panel) and rotation-pressure (right panel) in dif-
ferent periods (3-40s). In the left panel, red, green, and blue
lines represent the vertical, east, and north acceleration com-
ponents, respectively. In the right panel, red, green, and blue
lines represent the vertical, east, and north rotational compo-
nents, respectively. 'Sm' and 'Pm' with arrows represent the
period range of the secondary microseismic noise and the primary
microseismic noise

A.13 Seasonal variations in microseismic backazimuth and velocity
from 2016 to 2020 using the array-derived 6C observation. (a)
and (b) represent the seasonal backazimuth variation of the
secondary microseismic Rayleigh and Love wave (5-10s), respec-
tively. (c) and (d) represent the seasonal backazimuth variation
of the primary microseismic Rayleigh and Love wave (10-20s),
respectively. (e) and (f) represent the backazimuth and phase
velocity of secondary microseismic Rayleigh wave (5-10s), re-
spectively, where the black data points are obtained by using
Equations (1-4) with a one-day smoothing window. Here we only
keep the backazimuth between 200 and 260 degrees and velocity
between 2.8 and 4.0 km/s. The red and blue lines in (e-g) are the
smoothing result using the black data points with a three-month
time moving window. (h) The anisotropy model is obtained by
tang2024seismic using the 6C cross-correlation method. The
observation data represents the phase velocity variation with a
10 degrees smoothing window based on the black data points of
(e-f)
A.14 Projection of dominant microseismic noise sources in 2016-2017.
(a-d) represent the noise source estimated using the 6C method
based on the PFO.6C array. (e-h) represent the noise source
estimated using the beamforming method based on a large seis-
mic array (see Figures S5-S7, the aperture is about 180km).
The yellow and purple shaded zones represent the noise source
projections in summer and winter, respectively. The grey shaded
zone in (g) indicates the overlap of the yellow and purple shaded
zones. The black pentagram in Figure 4a and Figure 4e indi-
cates the location of the main secondary microseismic Rayleigh
wave source obtained by combining observations and numerical
simulations Obrebski et al. (2012)

Chapter 1

Introduction

As seismic instruments have become increasingly sensitive, they now measure continuous ground motion even in the absence of significant earthquakes or other transient seismic events. These signals, known as ambient seismic noise, differ from earthquake-generated waves in being omnipresent rather than episodic and localized. Ambient seismic noise consists of weak, permanent vibrations and has become an invaluable resource for seismologists, enabling innovative techniques like noise-based imaging and monitoring without requiring earthquakes or active sources.

The main sources of ambient seismic noise are broadly categorized into human activities and natural phenomena. Low-frequency seismic noise (<1 Hz), primarily generated by the interaction of ocean waves with the seafloor, appears as microseisms in seismic records from both land and ocean-bottom detectors. Microseisms can be further divided into primary and secondary types: primary microseisms have the same period as ocean waves (0.05–0.1 Hz), while secondary microseisms occur in a frequency band around 0.1–0.3 Hz, typically originating in the open ocean. This natural noise strongly dominates the seismic background below 1 Hz, making it particularly useful for imaging the lithosphere and global structures.

In contrast, high-frequency noise (>1 Hz) is primarily generated by human activities such as traffic, industrial operations, and urban development. These

high-frequency vibrations are typically used to sample the uppermost crust, allowing seismologists to investigate shallow structures such as sedimentary layers and near-surface geological features.

Over the past two decades, ambient seismic noise has gained importance in passive seismology. Through techniques such as seismic interferometry, crosscorrelation of noise recorded between two sensors can reveal the Earth's impulse seismic response. The continuous nature of ambient seismic noise enables repeated measurements, making it a robust tool in regions with limited earthquake activity. This capability allows researchers to study seismic properties in both tectonically active and stable areas. By cross-correlating noise recordings between pairs of seismometers, both direct surface wave travel times and the multiply scattered parts of the noise correlation wavefield can be extracted. These components specifically coda of correlation wavefields are highly sensitive to seismic velocity changes, making them useful for tomography and imaging. These studies have been widely used to map crustal and upper mantle structures, while temporal monitoring has provided insights into subsurface property changes. A key parameter, such as the propagation velocity of seismic waves which plays a crucial role in studying volcanic activity, tectonic stress, material properties, and subsurface reservoirs is retrieved using the coda of the correlation wavefield technique.

However, the successful extraction of meaningful information from noise cross-correlations depends heavily on the characteristics and distribution of noise sources. In practice, assumptions of wavefield equipartition or homogeneously distributed noise sources are often unmet. Although ambient noise is continuous, its properties vary over time due to changes in the intensity and distribution of its sources. For instance, oceanic microseisms exhibit seasonal variations, with higher amplitudes during stormy winter months in the Northern Hemisphere and more dominant sources in the Southern Hemisphere during summer.

Secondary microseisms, in particular, dominate noise recordings and serve as an important signal source for tomography and monitoring. However, this variability introduces challenges in interpreting subsurface properties in both temporal and spatial analyses. One focus of this research is to investigate how microseism energy contributes to correlation wavefields when these wavefields are used for other purposes, such as characterizing subsurface material properties. By clarifying the contribution of the most dominant sources in correlation techniques, understanding the location and behavior of seismic noise sources can provide insights into the underlying physical processes driving them and enhance the applications of ambient noise analysis. In the second part of this thesis, we aim to investigate microseismic sources in terms of their location and generation mechanisms. The following research questions are hereby proposed for investigation:

- How do persistent microseism noise sources influence the different parts of correlation wavefields?
- Do seasonal variations affect the stability of the direct arrival or later parts of the correlation wavefield?
- What are the locations of microseismic sources during summer and winter and how can microseism noise be decomposed into distinct wavefield components, such as Rayleigh and Love waves?

To answer these key questions, we employ techniques such as seismic interferometry, seismic array beamforming, and seismic array-derived rotation, which are discussed in detail in the subsequent chapters. The first two questions are addressed in Chapter 4, while the last question is covered in Chapter 5.

This chapter provides an introduction to the key concepts underlying ambient seismic noise, with a focus on ocean microseisms and ambient seismic noise interferometry. First, we present an overview of how microseismic noise is generated and its seasonal behavior. Next, we explore the technique of noise correlation and its application in studying subsurface properties. Finally, the main research objectives are outlined alongside the structure of this thesis.

1.1 Ambient seismic noise origin

Environmental noise studies have identified different sources responsible for generating seismic signals across various frequency ranges. These sources can be broadly divided into two main categories. The first category involves high-frequency noise (greater than 1 Hz), which is primarily associated with human activities. The energy of these signals varies over time, influenced by factors such as urbanization, with higher intensities observed during the daytime and on weekdays. These variations also depend on the specific region under observation (Bonnefoy-Claudet et al., 2006; Groos and Ritter, 2009).

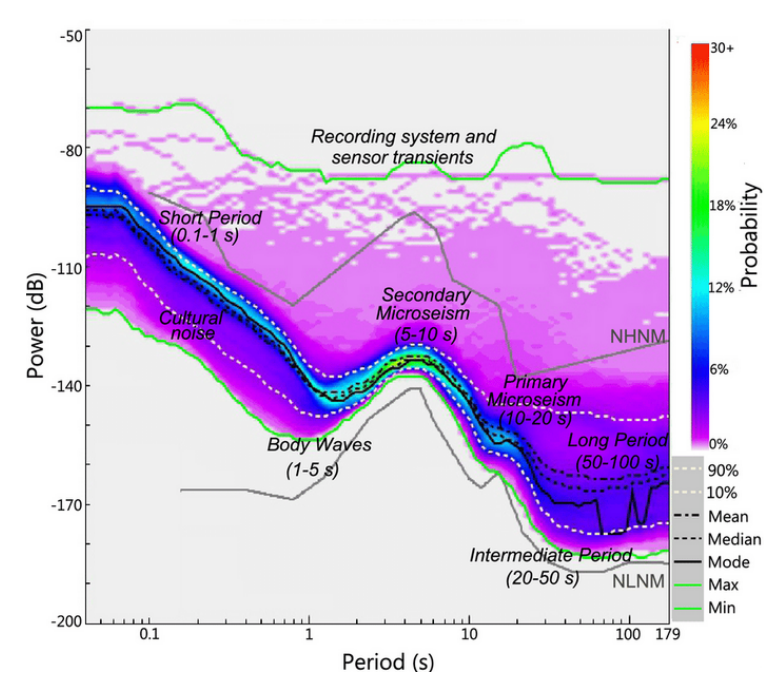


Figure 1.1: Seismic noise spectrum for the vertical recorded at the seismic station IN.SK04. Power Spectral Density (PSD) plot illustrating the characteristics of seismic background noise. The color bar indicates the probability distribution of noise across different frequencies. NHNM represents the New High Noise Model, while NLNM denotes the New Low Noise Model. The upper and lower white dotted lines correspond to the 10th and 90th percentiles of the PSD. The black dashed, dotted, and solid lines depict the mean, median, and mode of the PSD, respectively. The upper and lower solid green lines define the maximum and minimum PSD envelopes (Uthaman et al., 2022).

The second category relates to lower-frequency noise, originating from the coupling processes among the atmosphere, ocean, and seafloor. Unlike human-induced noise, these signals are relatively stable over time intervals of several

hours. They can be further classified into three distinct groups based on their frequency ranges: seismic hum (1–20 mHz), primary microseisms (0.02–0.1 Hz), and secondary microseisms (0.1–1 Hz). Figure 1.1 shows the probabilistic power spectral density (PPSD) for the characteristics of seismic background noise.

1.2 Oceanic microseisms

Seismologists began identifying microseisms as early as the 19th century when they observed continuous oscillations of the ground that were unrelated to earthquakes. Over time, advancements in technology, particularly the development of continuously recording broadband digital seismic stations, have significantly enhanced the ability to detect and study microseisms on a global scale. These oscillations were attributed to microseismic activity generated by interactions between ocean waves and the seabed in regions of deep water (Gutenberg, 1936, 1958). Microseisms dominate the energy spectrum of background seismic noise within the range of 0.05–0.3 Hz and are distinct due to their persistent nature. They are present continuously, 24 hours a day, throughout the year, with amplitudes generally ranging from 0.1 to 10 μ m (Haubrich, 1965; Steim, 2015).

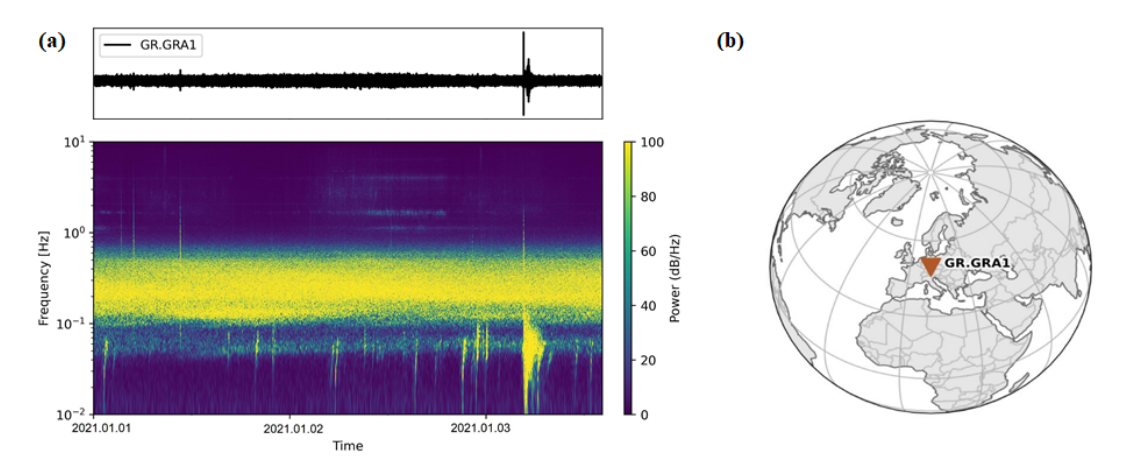


Figure 1.2: (a) Power spectral density for 3 days in 2021 recorded at the GRA1 broadband seismic station in the Gräfenberg array in Germany. (b) Location of the station

Figure 1.2 provides an illustration of the power spectral density (PSD) derived

from three days of vertical-component seismic data collected at the GR.GRA1 station within Gräfenberg array in Germany. Within the spectrum, two significant high-power densities are evident: the first, occurring in the range of 5–10 seconds, corresponds to secondary or double-frequency microseisms, while the second, observed in the range of 10–20 seconds, represents primary or single-frequency microseisms (Bernard, 1990; Cessaro, 1994; Bromirski and Duennebier, 2002; Ardhuin et al., 2015; Retailleau and Gualtieri, 2019). These microseism peaks are evident in spectra from any site, even far from the coast.

1.2.1 Primary microseism

Primary microseisms are generated through the interaction of surface gravity waves with the seafloor, typically in shallow coastal regions where the water depth is less than the wavelength of the incident ocean waves. The pressure fluctuations associated with ocean waves decrease exponentially with depth, making primary microseisms most prominent in areas where the seabed is directly influenced by wave motion. These oscillations are characterized by a frequency that aligns with the ocean waves responsible for their generation with the predominant frequency in 0.06 Hz (Hasselmann, 1963; Nakata et al., 2019).

The fundamental mechanisms behind primary microseism generation were initially explored theoretically by Hasselmann (1963). His study considered a simplified model with a uniformly sloping seafloor to evaluate the seismic response within the 0.05–0.1 Hz frequency range. Ardhuin et al. (2015) extended this approach to account for slowly varying seafloor topography by modeling the amplitude of the vertical component of the seismic waves which is composed primarily of Rayleigh waves. This studies laid the groundwork for understanding how ocean waves interact with the seafloor to generate seismic waves, providing a theoretical framework that primarily focused only on the generation of Rayleigh waves.

However, previous studies have shown that Love waves also contribute sig-

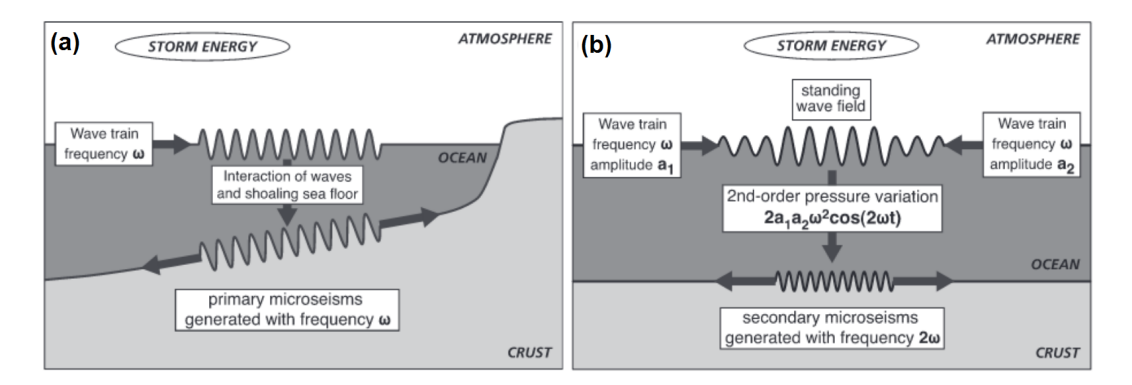


Figure 1.3: Cartoon illustrating (a) the primary microseism generation mechanisms. Where ocean waves interact with the seafloor. This process primarily occurs in shallow waters and is driven by the direct impact of ocean wave energy on the seabed. (b) The secondary microseism with meeting of two trains of ocean waves in opposite directions and with the same frequency. (Ebeling, 2012)

nificantly to the primary microseismic wavefield. In fact, the contributions of Love waves have been found to be comparable to, or even greater than, those of Rayleigh waves in some cases (e.g., Friedrich et al., 1998; Lin et al., 2008; Nishida et al., 2008; Juretzek and Hadziioannou, 2016). These findings highlighted the need to consider mechanisms involving horizontal forcing, which are more likely to occur through interactions between ocean waves and the solid Earth in shallow oceanic regions.

Saito (2010) demonstrated that the shear traction of ocean waves on the seafloor can generate Love waves. He introduced a framework to account for horizontal forces generated by surface waves interacting with complex topographic features. Ardhuin (2018) incorporated both horizontal and vertical forces into their analysis, further highlighting the importance of coupling between surface waves and fine-scale random topography. These developments have significantly advanced the understanding of primary microseism generation. An illustration of the primary microseism generation mechanism is shown in Figure 1.3a.

1.2.2 Secondary microseism

In contrast to primary microseisms, secondary microseisms are generated by the interaction of two opposing ocean wave trains traveling at the same frequency.

When these waves meet, they generate standing waves, characterized by pressure fluctuations that do not attenuate with depth. These second-order pressure forces act on the ocean floor, inducing elastic seismic waves that propagate through the Earth. The resulting seismic waves have a frequency that is double that of the interacting ocean waves (Longuet-Higgins, 1950; Ardhuin et al., 2011; Nakata et al., 2019). A cartoon of its generation mechanism is shown in Figure 1.3b).

Secondary microseisms represent the dominant source of seismic energy in the absence of significant earthquakes and are typically observed with a peak frequency around 0.14 Hz. Unlike primary microseisms, which are generally confined to shallow coastal waters, secondary microseisms can originate both near coastlines and in deep oceanic regions. Studies have shown that secondary microseisms are generated in diverse environments, including coastal zones (Yang and Ritzwoller, 2008), pelagic regions (Stehly et al., 2006), and even areas influenced by both coastal and open-ocean wave activity (Chevrot et al., 2007). Bromirski and Duennebier (2002) for instance, demonstrated that secondary microseisms are primarily driven by nearshore gravity wave interactions, with shore reflections providing the necessary opposing wave components, especially for wave periods exceeding 8 seconds. On the global investigation, Hillers et al. (2012) showed microseism sources are predominantly located near coastlines but can also originate in the deep ocean.

Ardhuin et al. (2011) identified three possible mechanisms responsible for the generation of secondary microseisms (see Figure 1.4). (A) An ocean storm at location A generates outwardly propagating waves. If the storm moves faster than these waves, they interact with waves generated by local winds in the opposite direction, creating a pressure source that leads to wave-wave interactions. (B) Ocean waves reflect off a coastline, producing a wave train that propagates in the opposite direction. (C) Two different storms generate independent swell systems that travel in opposite directions. However, the interaction of opposing swells from two storms has been shown to produce the most intense microseisms (Ardhuin et al., 2011).

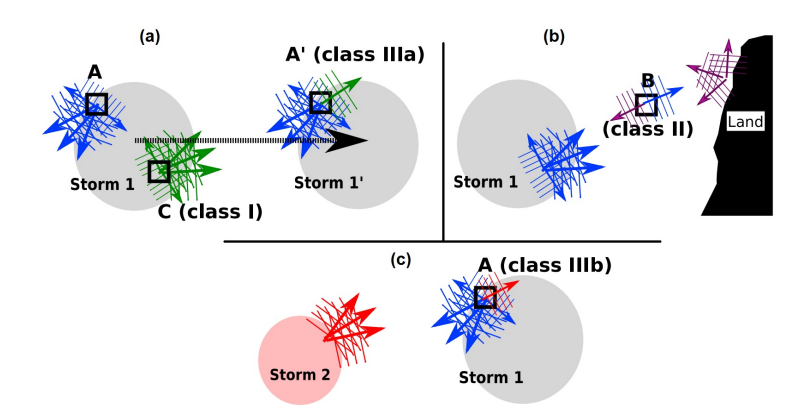


Figure 1.4: Schematic of wave conditions in noise-generating situations. (a) Storm 1 is rapidly moving so that waves generated at C become swell that can meet the wind-sea at point A'. In this case, the noise generated by the local wind-sea alone at point C (class I: wind-generated waves with a wide directional spectrum) can be much stronger at point A' because of the wider directional distribution. (b) Noise generated when waves reflect off the coast (class II: coastal reflection), and (c) noise generated when waves from two distinct storms cross, here at point A (class III: the interaction of two independent wave systems; Ardhuin et al. (2011)).

Microseisms can propagate as both surface and body waves. Primary microseisms contain substantial amounts of both Rayleigh and Love waves, with the presence of Love waves attributed to the direct interaction between traveling ocean waves and variations in sea-bottom topography. In contrast, secondary microseisms primarily consist of Rayleigh waves, generated by vertical forces resulting from wave-wave interactions. The mechanism responsible for Love wave excitation in the secondary microseism band remains less well understood. While some studies (Nishida et al., 2008; Juretzek and Hadziioannou, 2016) observe the same azimuth for the strongest sources for Love and Rayleigh waves, Gal et al. (2017) observed that the average power distribution of Rayleigh and Love waves differs in azimuth, likely due to their distinct generation processes. This study attributes Rayleigh waves to convex coastlines, whereas Love waves are linked to sedimentary basins on the seafloor.

This distinction highlights the different physical mechanisms responsible for generating primary and secondary microseisms. During typical microseismic periods, which range from 5 to 20 seconds, the seismic noise field is largely controlled by fundamental mode surface waves. Rayleigh and Love waves dominate the seismic signal during these periods, reflecting the stability and

regularity of ocean wave activity. In addition to surface waves, researchers have documented the detection of body waves primarily within the double-frequency microseism band (Gerstoft et al., 2006; Koper and de Foy, 2008; Landès et al., 2010; Zhang et al., 2010). Several studies have investigated the generation of body waves in secondary microseisms, revealing that they primarily originate in deep water and open oceans. Their sources often track intense oceanic storms in the Southern Hemisphere during summer and the Northern Hemisphere during winter (Obrebski et al., 2013; Stutzmann et al., 2012; Landès et al., 2010).

1.2.3 Seasonal variation

Strong microseism activity correlates well with regions of high wave energy, such as storm systems in both hemispheres, reflecting the seasonality of microseism activity. Stutzmann et al. (2009) analyse seismic noise spectra at all stations of the global GEOSCOPE network and show that higher microseism amplitudes during local winter at the high latitudes of both hemispheres. Figure 1.5 presents the average significant wave height, derived from WAVEWATCH III hindcasts (Tolman, 2014), for each month of 2019. During the boreal winter months (October–March), the highest average wave heights occur in the Northern Hemisphere, particularly in the North Atlantic and North Pacific, indicating dominant oceanic activity in these regions. This pattern shifts to the Southern Hemisphere during the boreal summer (April–September), with increased storm activities in the Southern Atlantic and Southern Pacific.

Unlike the Atlantic and Pacific Oceans, the Indian Ocean follows a different seasonal pattern. The Southern Indian Ocean experiences higher wave amplitudes during the austral winter, coinciding with the occurrence of larger storms. In contrast, the Northern Indian Ocean, which is enclosed by continents, generates fewer microseism sources compared to the more open Southern Indian Ocean (Davy et al., 2015).

Both primary and secondary microseisms exhibit distinct seasonal variations, as



Figure 1.5: Swell wave height output from the WAVEWATCH III model for 12 months of 2019.

documented in several studies (e.g., Stehly et al., 2006; Stutzmann et al., 2009; Gualtieri et al., 2019). Their sources predominantly shift between hemispheres, with stronger microseismic activity in the Northern Hemisphere oceans during winter and in the Southern Hemisphere oceans during summer. Persistent primary microseism sources have been identified in the North Pacific Ocean, near the west coast of the Queen Charlotte Islands, and in the North Atlantic Ocean, close to the coast of Newfoundland (Cessaro, 1994).

Secondary microseisms, on the other hand, exhibit heightened intensity during winter months in the Northern Hemisphere, particularly in wave interactions near the southern tip of Greenland (Kedar et al., 2008; Ardhuin et al., 2011). While both primary and secondary microseism frequently observe surface waves, body wave microseisms, particularly P-waves, have been more frequently detected in the secondary microseism(Toksöz and Lacoss, 1968; Gerstoft et al., 2008; Koper and de Foy, 2008). Some studies suggest that secondary microseismic P-waves originate from deep-ocean storms, showing consistent seasonal

variations that align with storm activity in each hemisphere (Haubrich and McCamy, 1969).

Figure 1.6 illustrates the spatial distribution of P-wave sources in the secondary microseism band (0.1–0.3 Hz). During the Northern Hemisphere summer, the strongest P-wave sources are predominantly located in the deep ocean, distant from coastal regions, with the most significant activity occurring in the Southern Hemisphere. In contrast, during Northern Hemisphere winter, intense wave activity in the North Atlantic and North Pacific Oceans generates stronger P-wave secondary microseisms.

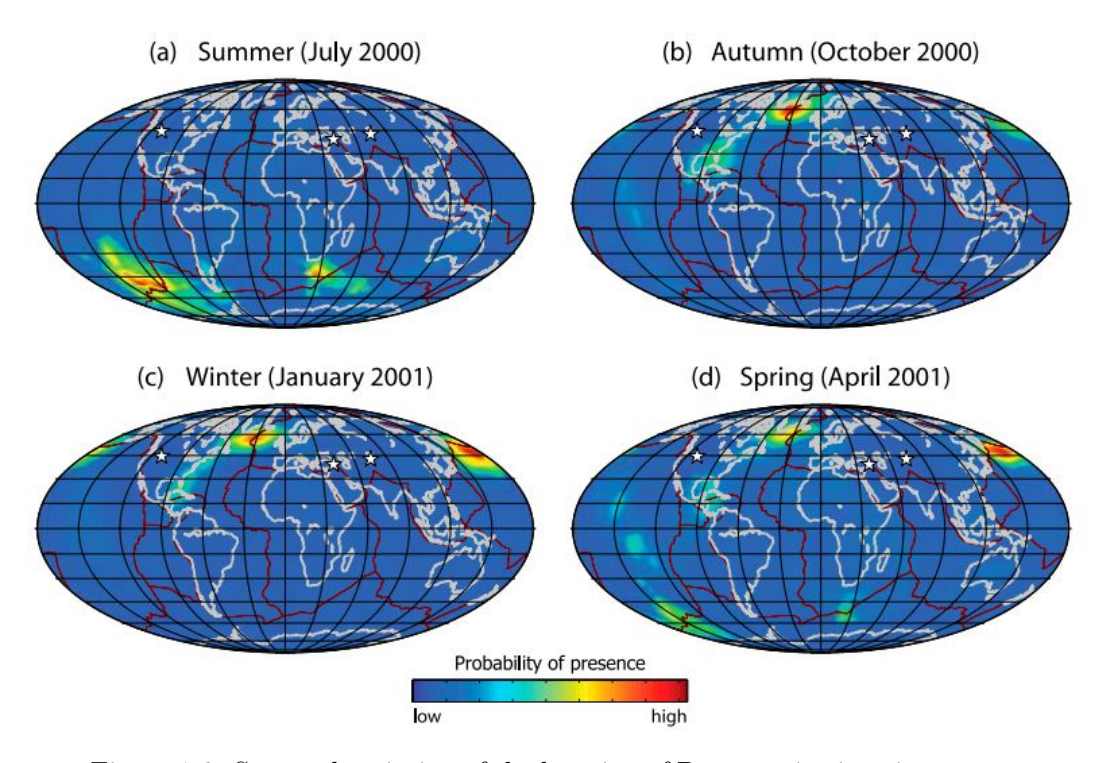


Figure 1.6: Seasonal variation of the location of P wave seismic noise sources in the secondary microseismic band (0.1–0.3 Hz). Landès et al. (2010)

A detailed analysis of continuous seismic records enhances our understanding of the origin of microseismic noise and its seasonal variations. This knowledge is crucial when applying correlation techniques to ambient seismic noise for monitoring and imaging purposes. In the next section, we discuss this technique in detail, along with the significance of understanding microseismic noise generation.

1.3 Ambient seismic noise interferometry

In seismic interferometry, the Green's function, or the impulse response of a medium, can be empirically derived through the cross-correlation function of ambient noise time series recorded simultaneously at two seismic stations (e.g., Campillo and Paul, 2003; Clarke et al., 2011; Sabra et al., 2005; Wapenaar and Fokkema, 2006). This approach enables the reconstruction of the Earth's impulse response without the need for active sources such as earthquakes or explosions. Conceptually, one of the stations is treated as a virtual source due to the absence of a real source, while the other station is considered as a receiver (Lobkis and Weaver, 2001; Weaver and Lobkis, 2004; Shapiro et al., 2005).

The study of correlation functions between random signals was first introduced by Aki in 1957. His research demonstrated that seismic wave velocities between seismometers could be estimated by analyzing the coherency of ambient seismic noise or random signals. Later, Claerbout (1968) discovered that the reflection response of a medium could be obtained through the cross-correlation of signals recorded at the surface. In experimental acoustics, Weaver and Lobkis (2001) investigated how correlation functions could emerge from thermally induced, fully scattered noise. These thermal noises were recorded by two receivers placed on an aluminum sample. The results obtained from this method were shown to be equivalent to the Green's function measured using direct impulsive forces between the same two points (Weaver and Lobkis, 2001). In seismology, Campillo and Paul (2003) demonstrated that stacking cross-correlation functions of seismic coda waves, recorded from 101 teleseismic earthquakes in Mexico, could effectively reconstruct the Green's function between stations.

Shapiro and Campillo (2004) extended this method to ambient seismic noise. Consequently, dispersion curves of Rayleigh waves were extracted by calculating the cross-correlation functions of noise recorded at stations separated by hundreds to thousands of kilometers. Afterwards the analysis of surface waves through cross-correlations of ambient noise has become a well-established

method, as surface waves dominate the Green's function between two stations on Earth's surface.

Seismic interferometry relies on the fundamental assumption that noise sources are uniformly distributed throughout space, ensuring that the computed noise correlation accurately approximates the Green's function of the medium (Snieder, 2004; Roux et al., 2005). Both theoretical and experimental studies have confirmed that when noise sources are homogeneously distributed and uncorrelated, the average cross-correlation function approximates the superposition of the Green's function and its time-reversed counterpart (Wapenaar and Fokkema, 2006; Wapenaar, 2004).

In applied seismology, the ideal assumption of uniformly distributed noise sources is rarely met due to the uneven spatial distribution of ambient seismic noise across different regions, with oceanic regions being highly effective in generating microseisms. As a result, asymmetries in both the amplitude and spectral characteristics of noise correlations commonly arise. These variations stem from differences in noise generation processes and the non-uniform distribution of noise sources. Some studies have shown that emergence of the Green's function often requires the sufficient self-averaging process (i.e., stacking) over long time periods to enhance random spatial distribution of the noise sources (e.g., Campillo, 2006; Larose et al., 2006). However, when the station pairs are poorly oriented with respect to the dominant direction of the noise source, long-term stacking significantly enhances the signal-to-noise ratio but does not always restore the expected symmetry.

Figure 1.7a illustrates the correlation wavefield recorded between station BRMO, located within the Italian array, and station GRA1, positioned inside the Gräfenberg array in Germany. The cross-correlation wavefield obtained from the vertical component in the frequency range of 0.05–0.1 Hz is stacked over two years. As observed, the fundamental mode Rayleigh wave is obvously visible in positive and in the negative lag time sides. A clear asymmetry in the amplitudes of the positive and negative components of the Green's function is evident, reflecting differences in both the noise source characteristics and the

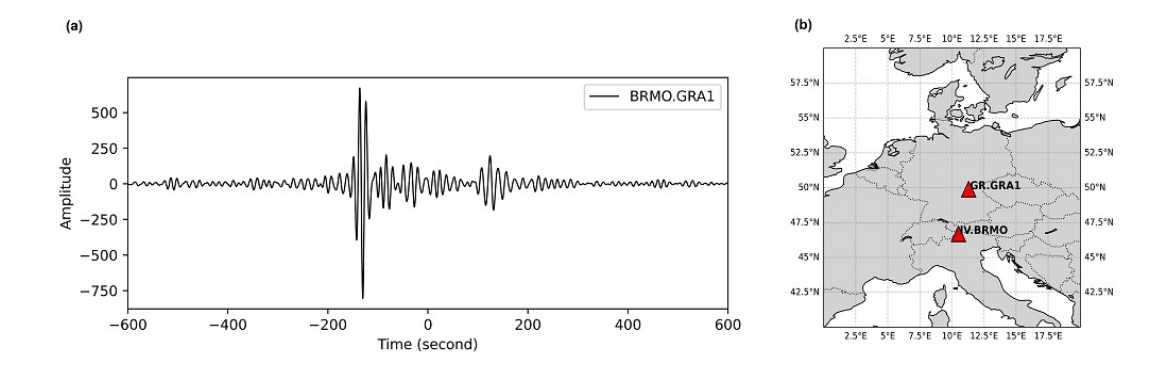


Figure 1.7: (a) Two years stacking of the correlation wavefield between IV.BRMO-GR.GRA1. Considerable asymmetry in amplitude can be observed in the positive and negative elapsed time sides.(b) the location of two regional scale seismic stations, IV.BRMO in the Italian seismic array and GR.GRA1 in the Gräfenberg array in Germany, with a distance between stations of 700 km.

relative distances to sources propagating in opposite radial directions from the stations.

1.3.1 Correlation wavefield application

The correlation technique has been widely applied in surface wave tomography to investigate the elastic structure of the Earth on scales ranging from local to global (e.g., Bensen et al., 2007; Yang and Ritzwoller, 2008). This method exhibits numerous advantages over classical tomography.

Measurements obtained using surface waves from teleseismic events are limited to specific directions and ray paths determined by the locations of earthquakes and seismic stations. Consequently, many other propagation directions are not sampled or recorded. In contrast, with this method, measurements can be conducted in all possible propagation directions, depending on the positioning of the stations.

The inversion of surface waves in classical methods requires prior information about the sources, which is not always available with sufficient accuracy. However, the ambient seismic noise method is independent of earthquake sources.

Surface wave measurements from teleseismic events provide average values over

a large region, limiting spatial resolution and reducing the accuracy of Earth imaging. In contrast, results derived from ambient seismic noise, particularly for group velocity measurements, are influenced by interstation distance. Utilizing a dense seismic network enhances the quality of these results, leading to more precise imaging.

Obtaining dispersion curves of surface waves for periods shorter than 20 seconds using classical methods is challenging due to significant attenuation and heterogeneities along the source-to-station path. However, the ambient seismic noise method enables accurate imaging of Earth's crustal structure even at these shorter periods. Additionally, local earthquake tomography provides another valuable approach for resolving crustal structures at similar wavelengths, offering complementary insights into subsurface properties.

A key advantage of using continuous seismic noise recordings to study the Earth's subsurface is the ability to make repeated measurements over time. This capability has led to the development of real-time crustal monitoring techniques, where continuous seismic data from station networks allow the detection of temporal changes in the velocity structure of the medium between sensor pairs. This approach provides a highly sensitive method for tracking variations in subsurface properties.

As discussed in Section (1.3), the ideal condition of a uniformly distributed noise field is rarely met in real-world scenarios. This non-uniformity can distort direct wave arrivals, affect amplitude measurements, and introduce biases in the estimated Green's functions (Tsai, 2009; Yao and Van Der Hilst, 2009; Froment et al., 2010; Delaney et al., 2017). To mitigate these issues, several studies have emphasized long-term averaging of cross-correlation functions and applied additional preprocessing techniques to minimize the influence of uneven noise distribution on Green's function reconstruction (Safarkhani and Shirzad, 2019; Fichtner et al., 2020; Shirzad et al., 2022).

In particular, variations in noise source distribution tend to introduce greater errors in the reconstruction of direct wave arrivals compared to the coda of the seismic Green's function. Coda waves, which result from multiple scattering events and repeated sampling of the medium, have proven to be a valuable tool for Earth imaging. Unlike direct waves, scattered coda waves are considered less sensitive to the spatial distribution of ambient seismic noise sources. Studies by Stehly et al. (2008) have demonstrated that Green's functions can be effectively reconstructed using the coda portion of ambient noise correlations. This approach involves computing the Green's function between station pairs, using a third station as a virtual station, thereby improving the robustness of the method against noise source anisotropy.

In these studies, the primary contribution to the coda correlation wavefield, particularly at late coda, is attributed to a purely scattered wavefield rather than strong directional sources. As a result, most studies focus on coda waves reconstructed by cross-correlation because they are considered more sensitive to material changes than direct arrivals (Froment et al., 2010; Colombi et al., 2014). The monitoring of coda waves is based on the measurement of the time delay between long-term reference cross-correlations and short-term correlations. This observed delay is interpreted as an indicator of variations in seismic velocity and interpreted as temporal changes within the medium (Clarke et al., 2011).

In this study, the focus is on persistent and uncontrolled sources on correlation wvefields. Microseismic sources act as uncontrolled seismic source as we cannot control the location and/or source-time function. We investigate how these sources influence the cross correlation function in early and later arrivals.

Chapter 2

Theory and Methods

2.1 Correlation technique

To conceptualize correlation technique, consider two seismic receivers positioned at locations X_A and X_B , surrounded by a set of sources distributed within an arbitrary spatial domain bounded by S (Figure 2.1a) Each noise source emits a wavefield that propagates through the medium and is subsequently recorded by both receivers. By computing the cross-correlation of the signals recorded at these two locations and summing the contributions from all sources along the boundary \mathbf{S} , the wavefield propagating along the direct path between the receivers will constructively interfere. These regions where wave energy aligns coherently are known as Fresnel zones (e.g., sources positioned along the axis connecting the two receivers, represented by the thick dashed line in Figure 2.1b). Conversely, outside these zones, destructive interference occurs, leading to an overall attenuation of energy. As illustrated in Figure 2.1b, the computed cross correlation for all sources between two receivers outside the vertical dashed lines. Upon summation of all computed correlation wavefields in Figure 2.1b, the Green's function emerges between the two receivers. This scenario simulates one receiver effectively acting as a virtual source while the other remains a receiver (Figure 2.1c; Wapenaar et al. (2010)).

Using seismic interferometry, the Green's function between the two points can

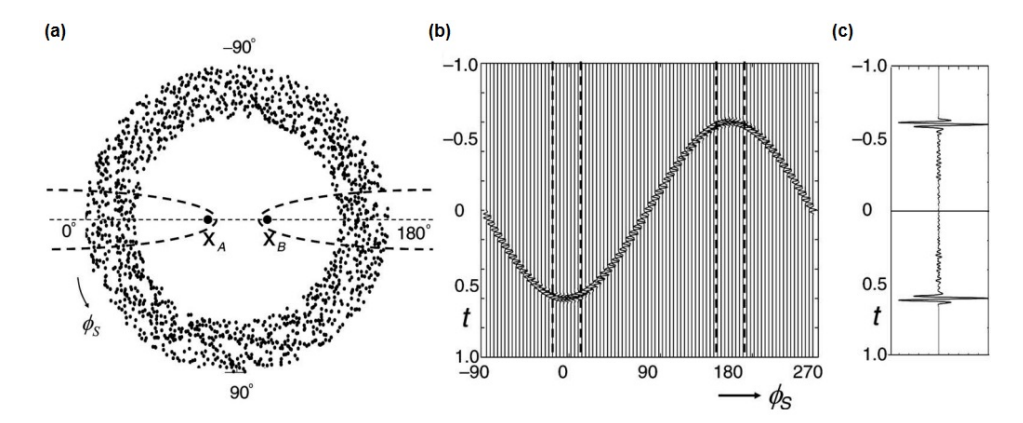


Figure 2.1: Isotropic distribution of noise sources surrounding stations located at \mathbf{X}_A and \mathbf{X}_B . The thick dashed lines represent the Fresnel zones. (b) Cross-correlation of the recorded responses at the receiver locations, where the primary contributions originate from sources within the Fresnel zones, marked by the dashed vertical lines. (c) Summation of the cross-correlations shown in (b).(Wapenaar et al., 2010)

be expressed in terms of an integration over all possible sources on a boundary **S** (Wapenaar et al., 2010):

$$G(x_A, x_B, \omega) - G^*(x_A, x_B, \omega) = \frac{2i}{\omega} \int_S T(x) u^*(x, x_A, \omega) u(x, x_B, \omega) dx \qquad (2.1)$$

where: $G(x_A, x_B, \omega)$ is the Green's function between two points x_A and x_B at angular frequency ω . $G^*(x_A, x_B, \omega)$ is the complex conjugate of the Green's function. T(x) represents the energy flux at the boundary S. $u(x, x_A, \omega)$ and $u(x, x_B, \omega)$ are wavefields observed at points x_A and x_B .

The resulting function is symmetric in time, producing both positive and negative correlation lags, which represent signals propagating in opposite directions. The segment of the cross-correlation function corresponding to positive time lags is referred to as the causal signal. As illustrated in Figure 2.1c, related propagated wavefields diverge from the station considered as a source. Conversely, the negative time lags, known as the acausal signal, depict wave propagation in the reverse direction, effectively interchanging the roles of the two stations (Campillo, 2006).

2.2 Pre-processing correlation computation

In this section, the processing steps applied to continuous seismic noise recordings to compute correlation wavefields are outlined. The data processing workflow follows the methodology established by Bensen et al. (2007) and is divided into three main stages: (1) preprocessing of single station data, (2) cross-correlation of all possible station pairs, (3) stacking and extraction of empirical Green's functions.

The initial stage of data processing (i.e., preprocessing of raw data) involves several essential steps aimed at enhancing ambient noise signals while suppressing transient signals such as earthquakes. This step is crucial for minimizing biases introduced by non-diffuse wavefields. First, each daily recorded trace undergoes mean and trend removal. Since the study focuses on microseismic frequency bands (<1 Hz), the data are downsampled to 2 Hz in accordance with the Nyquist theorem. Additionally, the instrument response is removed to ensure consistency across different seismic networks. A bandpass filter, designed according to the target period range (i.e., microseismic frequencies), is applied with specific corner frequencies (0.01, 0.03, 0.3, 0.9 Hz). The traces are then segmented into daily recordings. The subsequent steps involve time-domain and frequency-domain normalization (Sections 2.2.1 and 2.2.2).

2.2.1 Time-domain normalization

Preprocessed seismic data contain not only ambient noise signals but also a variety of transient signals originating from high-energy events (e.g., earth-quakes, landslides, explosions, volcanic activity), human activities (e.g., traffic, industrial operations, urban noise), and instrumental artifacts. These transient signals can dominate recorded waveforms, significantly influencing cross-correlation results.

One of the primary challenges in automated seismic processing is the irregular occurrence of earthquakes. While seismic catalogs provide records of larger

earthquakes, smaller seismic events are often undocumented. As a result, earthquake-induced noise must be identified and removed directly from the processed data rather than relying solely on earthquake catalogs (Bensen et al., 2007). Furthermore, scattered waves are generally weaker than direct waves, making it essential to apply normalization techniques that minimize biases caused by transient signals while enhancing scattered wave detection. This ensures that the contribution of input signals to the reconstruction of empirical Green's functions remains balanced across both time and frequency domains.

Several methods can be used for time-domain normalization, with the choice depending largely on the characteristics of the dataset. The most commonly used techniques are described below.

2.2.1.1 One-bit normalization

One of the most widely used methods is one-bit normalization, in which only the sign of the signal is retained. In this approach, all positive amplitudes are replaced with +1, while all negative amplitudes are set to -1 (Bensen et al., 2007).

$$x_{i} = \begin{cases} -1, & \text{if } x_{i} < 0 \\ 0, & \text{if } x_{i} = 0 \\ 1, & \text{if } x_{i} > 0 \end{cases}$$

This is a nonlinear method that acts similar to a nonlinear low-pass filter. While it removes amplitude information, it primarily preserves phase content at lower frequency signals.

2.2.1.2 Running average normalization

In this method, a symmetric window is centered at each sampled point in the waveform. The absolute mean value within this window is calculated and assigned to the central point. This process is repeated for all sampled points. The weighting of each measured point follows Equation 2.2 as defined by Bensen et al. (2007):

$$w_n = \frac{1}{2N+1} \sum_{j=n-N}^{n+N} |d_j| \tag{2.2}$$

According to this equation, the normalized data are obtained by multiplying the original waveform by the inverse of the computed weight.

$$\tilde{d}_n = \frac{d_n}{w_n} \tag{2.3}$$

The chosen window length (2N + 1) is a critical parameter, as it influences the retention of signal information. In the extreme case of using a single sample window (N = 0), this method becomes equivalent to one-bit normalization.

2.2.2 Frequency-domain normalization

In addition to time-domain normalization, it is crucial to ensure that processed data retain useful frequency content. Studies have demonstrated that ambient seismic noise is not uniformly distributed across the frequency spectrum (Bensen et al., 2007). Monochromatic signals, such as those found in the 26 sec microseism spectrum, tend to exhibit peak values at specific frequencies due to the uneven distribution of ambient seismic noise sources in certain regions. These signals, along with high-energy seismic events such as earthquakes and landslides, create spectral peaks that can distort the frequency content of the signal. As a result, this non-uniform frequency distribution negatively affects the quality of the extracted empirical Green's functions.

To mitigate these effects, normalization is applied in both time and frequency domains (Bensen et al., 2007; Stehly et al., 2009). After applying a Fourier transform to convert the signal to the frequency domain, the amplitude spectrum is adjusted using a smoothed version of itself within predefined frequency bands. During this process, the phase spectrum remains unchanged, a procedure known as Frequency-Domain normalization or spectral whitening.

Spectral whitening reduces the influence of dominant microseism signals by

flattening the amplitude spectrum across the desired frequency range. Before applying frequency-domain normalization, additional pre-processing steps including windowing, trend and mean removal, and running average normalization are performed to ensure consistency and enhance the quality of the extracted empirical Green's functions or reference cross-correlations.

2.2.3 Retrieving the reference correlation wavefields

According to Section 2.1, after preprocessing the daily single station recordings, the prepared waveforms are cross-correlated for all possible station pairs within the network.

Cross-correlation is performed for each station pair using vertical-component data recorded simultaneously on a given day. The resulting daily correlation functions are subsequently stacked over two years time span.

Linear stacking is a common technique employed in this study, which is widely employed to enhance the signal-to-noise ratio (SNR) to generate reference correlation functions for each station pair. The primary purpose of stacking is to suppress noncoherent undesired signals, while preserving and reinforcing the coherent components of ambient seismic noise. By stacking cross-correlation functions over various time periods, the azimuthal coverage of ambient seismic noise sources is effectively increased, leading to an overall improvement in the coherence of the retrieved signal.

In this study, cross-correlation functions are stacked across different time intervals, including seasonal (six months corresponding to summer and six months corresponding to winter) and biennial (two-year) periods, following a linear stacking approach. The highest SNR is achieved when all daily cross-correlation wavefields are incorporated into the stacking process, with the two-year stacked function yielding the most stable and well-defined empirical Green's function (Bensen et al., 2007).

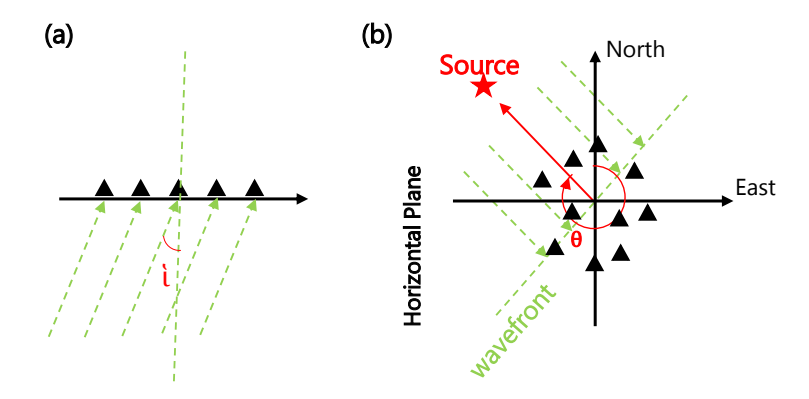


Figure 2.2: Schematic illustration of a plane wave emitted from a source (red star) propagating across the seismic array (black triangles). Due to a specific slowness, the wavefield reaches each station at different times. (a) The incidence angle (i) of the incoming plane wavefront is defined in the vertical plane, while the backazimuth (θ) is defined in the horizontal plane. Incoming plane wavefront is indicated by green dashed lines. Adapted from Schweitzer et al. (2012).

2.3 Beamforming

Beamforming is an array processing technique used to estimate the proportion of seismic wave energy that coherently propagates across an array. This method, widely applied not only in seismology but also in radar analysis, wireless communications, astronomy, and acoustics, is instrumental in localizing and identifying seismic sources(Capon, 1969; Van Trees, 2002; Dewdney et al., 2009). Rost and Thomas (2002) investigated this approach using a delay and sum process to estimate the direction and velocity of propagating seismic wavefronts. By enhancing the signal to noise ratio (SNR) through summation of the coherent part of seismic signals recorded at different array sensors, beamforming allows for the determination of both the back azimuth and apparent velocity (slowness) of a given seismic phase. Typically, array processing assumes a plane wavefront approaching the array, characterized by an incidence angle (i) and a back azimuth (θ) , as illustrated in Figure 2.5.

In this approach, the arrival time of seismic waves at a reference station (often positioned at the center of the array) is used as a baseline. The recorded waveforms from all sensors in the array are time shifted accordingly to achieve optimal alignment. This alignment ensures that the coherent components of the seismic signals sum constructively, forming a high amplitude beam. The accuracy of this process relies on correctly estimating the delay time, which represents the additional time required for a plane wavefront to reach different stations within the array.

Mathematically, any plane wave can be parametrized using its horizontal slowness vector (u_h) , where (u) consists of three components:

$$\mathbf{u} = (u_x, u_y, u_z)$$

$$\mathbf{u} = u_h \left(\sin \theta, \cos \theta, \frac{1}{\tan i} \right)$$
(2.4)

(i), incidence angle approaching seismic array

across the array.

 (θ) , back azimuth indicating the direction of wave propagation, and (u_h) , horizontal slowness representing the apparent velocity of the wavefront

Theoretical time delays (τ) between stations can be determined based on the station coordinates (\mathbf{r}) and the horizontal slowness (u_h) of the seismic waves:

$$\tau = \mathbf{r} \cdot u_{\rm h}$$

Once these delays are removed from all station recordings, beamforming values according to the specific slowness (u_h) and back azimuth (θ) can be computed as follows (Gal et al., 2019):

$$b(u, t, \theta) = \frac{1}{N} \sum_{j=1}^{N} d(x_j, t + \tau_j(u_h, \theta))$$
 (2.5)

where $d(x_j, t)$ is the recorded seismogram at station j, τ_j is the relative travel time correction for station j, and N represents the total number of stations in the array.

A grid search over discrete slowness and back azimuth values is performed

to maximize beam power, thereby identifying the dominant direction of wave propagation along with its corresponding slowness.

2.3.1 Single-component beamforming

Beamforming techniques can be applied to both single-component and threecomponent seismic arrays. In this section, we discuss the single-component beamforming method that we use.

A conventional beamforming approach can also be implemented in the frequency domain, rather than the time domain, by utilizing the Fourier transform of the recorded waveforms (Qin and Lu, 2024). Mathematically, this is expressed as:

$$b(u,\omega,\theta) = \frac{1}{N} \sum_{j=1}^{N} d(x_i,\omega) e^{i\omega u_{\rm h}(r_j - r_0)}$$
(2.6)

where $d(x_j, \omega)$ is the Fourier transform of $d(x_j, t)$ in equation 2.5. Instead of performing time shifts, this approach applies phase shifts of the form $e^{i\omega u_h(r_j-r_0)}$ to align waveforms across different stations, followed by stacking, to compute the final beam power values.

An alternative approach, known as cross-correlation beamforming, has been introduced in some studies. This method applies the delay-and-sum process to the correlation functions of seismic recordings rather than to the recordings themselves (Baggeroer et al. 1988, Ruigrok et al., 2017).

$$b(u,\omega,\theta) = \frac{1}{N^2} \sum_{j=1}^{N} \sum_{\substack{k=1\\k\neq j}}^{N} C_{jk}(r_{jk},\omega) e^{i\omega u_{\rm h}(r_j - r_k)},$$

$$C_{jk}(r_{jk},\omega) = d^*(x_j,\omega) d(x_k,\omega)$$
(2.7)

The cross-covariance matrix C_{jk} is used, where the relative phase shift between two stations x_j and x_k is contained. In this equation, superscript * denotes the complex conjugate. This method significantly enhances the accuracy of back azimuth and slowness estimation compared to conventional beamforming, as it leverages the coherence of seismic wavefields across the array.

In beamforming analysis, the plane-wave approximation is valid when the seismic source is located in the far-field region, meaning that the distance from the source is significantly greater than the aperture of the array. The array aperture is defined as the maximum distance between the outermost seismic sensors within the array, and its size is determined based on the wavelength of interest. Larger aperture arrays provide better resolution for longer wavelengths (lower frequencies), allowing for improved discrimination of wave arrivals and their slowness. In other words, to resolve the signals, the aperture of the array must be at least as large as the observed wavelengths (Schweitzer et al., 2002).

In Chapter 4, the cross-correlation beamforming method is applied to single vertical component data, which discussed in details in a subsequent chapter.

2.3.2 Three-component beamforming

Esmersoy et al. (1985) extended the single-component beamforming approach to a three-component framework for estimating the properties of a propagating seismic wavefield. The primary advantage of three-component (3C) beamforming is that it not only allows for the determination of the back azimuth and slowness of the wavefield but also enables the discrimination between different wave types. By utilizing all three components (vertical, radial, and transverse), it becomes possible to distinguish Love waves from Rayleigh waves, particularly when analyzing surface waves.

Polarization refers to the orientation of particle motion as a seismic wave propagates through a medium. Love waves exhibit horizontal polarization, meaning their motion is entirely transverse to the propagation direction. Consequently, Love waves are predominantly recorded on the transverse component.

Rayleigh waves, in contrast, exhibit elliptical particle motion in the vertical

plane aligned with the propagation direction. Near the surface, the motion follows a counterclockwise elliptical trajectory (when viewed in the direction of wave propagation). However, at greater depths, due to the interaction between compressional (P) and vertical shear (SV) waves, the motion transitions to a prograde elliptical trajectory. As a result, Rayleigh waves are primarily recorded on the vertical and radial components.

The polarization introduces an additional phase shift among the different components of the seismic wavefield, which remains consistent across all stations. This function can be formally expressed as (Riahi et al., 2013):

$$w(k,\xi) = c(\xi) \otimes a(k). \tag{2.8}$$

where ξ is the polarization parameter and $c(\xi)$ represents the different polarization states among the East (E), North (N), and Vertical (Z) components and k is wave vector. a(k) represents the mode vector, which describes the spatial distribution and relative phase variations of the incoming seismic wave energy as a function of the wave vector k.

By generalizing the conventional single-component beamforming technique, the three-component beamforming function can be formulated as:

$$R(k,\xi) = w(k,\xi)^* S_{3C} w(k,\xi). \tag{2.9}$$

where $S_{3C} = \langle s_{3C}.s_{3C}^* \rangle$ represents the spectral density matrix, and (s_{3C}) is a column vector containing the 3N Fourier amplitudes of all channels. The optimal values of the beamforming function $R(k,\xi)$ indicate the dominant wave parameters, including slowness, back azimuth, and polarization in a three-component seismic array.

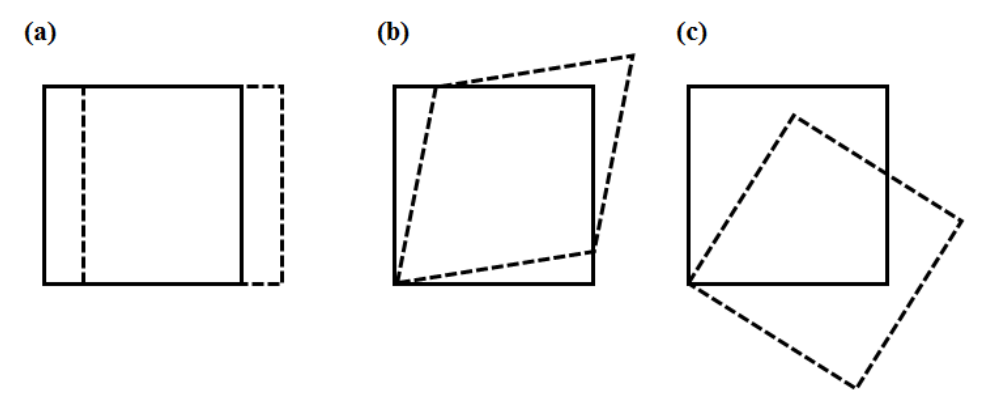


Figure 2.3: Three types of motion for solid particles in classic elasticity. (a) Translational motion, (b) deformation, and (c) rigid rotational motion. solid line, original body; Dot line, new body shape.

2.4 Rotational seismology

A complete description of the motion of deformable solid particles at a specific point demands consideration of three crucial components: pure translational motion, rigid rotational motion, and deformation (e.g., Aki and Richards (2002)). These basic concepts of three categories of particle motion are visually illustrated in Figure 2.3. Translational and rotational motions describe the relative displacement of the particle, capturing changes in its position and rotation, respectively (see Figure 2.3a and c). In contrast, deformation reflects a relative change in the shape of the particle, capturing the effects of strain or deformation (see Figure 2.3b). A comprehensive basis for understanding the motion at a given point is provided by the combination of 12 components of freedom, including three components of translational and rotational motions and six components of strain.

In seismology, the formulation of rotational motion has been studied by Aki and Richards (2002). However, the practical implementation of rotational motion studies has been limited due to the historical absence of instruments with sufficient sensitivity to measure the rotational motion of the ground.

In the context of wave propagation, the displacement wavefield \mathbf{u} describes the position of a particle relative to its original location at a reference time \mathbf{t}_0 . The position of a particle at time \mathbf{t} , relative to its reference position \mathbf{x}_0 at \mathbf{t}_0 , can

be expressed as a vector field:

$$u(\mathbf{x}_0, t) = \mathbf{x} - \mathbf{x}_0 \tag{2.10}$$

In this equation, $u(\mathbf{x}_0, t)$ denotes the displacement vector, \mathbf{x} represents the particle's location at time \mathbf{t} , and \mathbf{x}_0 signifies the reference position. With Taylor series expansion this equation can be written as (Shearer (2019)):

$$\mathbf{u}(\mathbf{x}) = \begin{bmatrix} u_x \\ u_y \\ u_z \end{bmatrix} = \mathbf{u}(\mathbf{x}_0) + \begin{bmatrix} \frac{\partial u_x}{\partial x} & \frac{\partial u_x}{\partial y} & \frac{\partial u_x}{\partial z} \\ \frac{\partial u_y}{\partial x} & \frac{\partial u_y}{\partial y} & \frac{\partial u_y}{\partial z} \\ \frac{\partial u_z}{\partial x} & \frac{\partial u_z}{\partial y} & \frac{\partial u_z}{\partial z} \end{bmatrix} \begin{bmatrix} d_x \\ d_y \\ d_z \end{bmatrix} = \mathbf{u}(\mathbf{x}_0) + \mathbf{G}\delta x, \quad (2.11)$$

G is gradient tensor and δx represents the small displacement vector between the point **x** and the reference position **x**₀. Using the context of infinitesimal strain theory, the Earth's material can be considered homogeneous. We simplify the analysis by neglecting higher-order terms in equation 2.11. This simplification is justified by assuming that the partial derivatives of displacement components, such as $\frac{\partial u_x}{\partial x}$ and $\frac{\partial u_y}{\partial x}$, and similar terms, are sufficiently small that can be ignored.

G can be decomposed into the symmetric strain tensor **e** and the antisymmetric rotation tensor Ω .

$$u(\mathbf{x}, t) = \mathbf{u}(\mathbf{x}_0) + \mathbf{e}\delta x + \Omega \delta x \tag{2.12}$$

To simplify the representation, the rotational tensor can be expressed as $\frac{1}{2}\nabla \times \mathbf{u}(x)$. This implies that the rotational motion, Ω , is equal to half the curl of the displacement field \mathbf{u} (Aki and Richards, 2002).:

$$u(\mathbf{x}, t) = \mathbf{u}(\mathbf{x}_0) + \mathbf{e}\delta x + \omega \delta x \tag{2.13}$$

$$\boldsymbol{\omega} = \begin{pmatrix} \omega_1 \\ \omega_2 \\ \omega_3 \end{pmatrix} = \frac{1}{2} \nabla \times \mathbf{u} = \frac{1}{2} \begin{pmatrix} \partial_y u_z - \partial_z u_y \\ \partial_z u_x - \partial_x u_z \\ \partial_x u_y - \partial_y u_x \end{pmatrix}$$
(2.14)

Among all seismic waves, the P-wave is unique in that it does not produce any rotational motion. In contrast, ground rotations induced by S-waves and surface waves can be described using the ground vibration velocities measured in two orthogonal directions. These rotational motions are quantitatively represented by Equation 2.14.

In the field of seismology, rotational motions have historically been regarded as negligible and challenging to record. However, the study of rotational motion in seismology offers several advantages, significantly enhancing our understanding and interpretation of seismic signals. By jointly analyzing translational and rotational components, seismologist can improve the signal-to-noise ratio in seismic observations, allowing for clearer detection of events (Brokešová and Málek, 2013). This combined approach also aids in accurately pinpointing the location of seismic sources and enhances the capabilities of tomographic imaging techniques (Bernauer et al., 2009).

Furthermore, rotational motion analysis facilitates the identification of rotational modes and resonance frequencies within seismic data, providing valuable insights into the dynamic behavior of the Earth's interior (Sollberger et al., 2020; Lin et al., 2011). Lastly, their ability to distinguish signals from distant powerful sources and nearby weaker ones further underscores their utility in complex seismic environments (Igel et al., 2005; Bernauer et al., 2012). For over three decades, rotational sensors have been available, particularly through the use of laser technology. These developments have enabled seismologists to directly measure rotational ground motion across a range of scales, from small, localized earthquakes to large, distant teleseisms (e.g., Takeo (1998); Pancha et al. (2000); Suryanto et al. (2006); Schreiber et al. (2006), Igel et al. (2011)).

Significant advancements in this field is the incorporation of Sagnac interferometry within large ring-laser gyroscopes, a method that has demonstrated efficacy in detecting rotational motion at teleseismic distances, with results that are in close agreement with predictions from linear elastic wave theory (Pancha et al., 2000). However, such measurements have historically been constrained to a relatively limited frequency range, thereby restricting their applicability to different broader frequency ranges. Recent advancements include the work of Igel et al. (2005), who utilized ring-laser recordings to capture the Earth's free oscillations, thereby facilitating the application of rotational seismology to longer periods. Furthermore, the study introduced an innovative approach for estimating horizontal-phase velocity by using data from ring lasers with transverse acceleration measurements obtained from nearby classical seismographs.

2.4.1 Array-derived rotation

In addition to the direct measurement of rotation, the indirect detection of rotational motions through the use of classical seismometers has been explored in numerous studies (e.g., Spudich et al., 1995; Bodin et al., 1997; Huang et al., 2003). These studies use the small-aperture seismic arrays, composed of linear motion sensors spaced at distances smaller than the recorded wavelength, provides a method for obtaining teleseismic rotational data. This approach assumes minimal contamination of translational signals by rotational motions and relies on the applicability of classical elasticity theory. For example, Spudich et al. (1995) examined the rotational components of a microseismic array by employing finite-difference methods to estimate the displacement gradient matrix. It has been demonstrated that, at the boundary of a free surface, the time-dependent displacement gradient matrix G, derived from data recorded by N three-component seismographs, can be resolved mathematically as:

$$d_{i} = GR_{i} = \begin{pmatrix} \partial_{x}u_{x} & \partial_{y}u_{x} & \partial_{z}u_{x} \\ \partial_{x}u_{y} & \partial_{y}u_{y} & \partial_{z}u_{y} \\ \partial_{x}u_{z} - \partial_{z}u_{y} & \partial_{y}u_{z} - \partial_{x}u_{z} & -\eta(\partial_{x}u_{x} + \partial_{y}u_{y}) \end{pmatrix} R_{i}, \quad (2.15)$$

Where the tensor \mathbf{G} is defined as the displacement gradient matrix, $\mathbf{R}_i = \mathbf{r}_i$ - \mathbf{r}_0 and $\mathbf{d} = \mathbf{u}_i$ - \mathbf{u}_0 correspond to the relative distance and displacement of station \mathbf{i} with respect to a reference station.

When ground displacements are recorded at a minimum of three surface stations with accurately known relative positions, the rotational components can be determined using standard least-squares inversion techniques (Spudich et al., 1995).

Using $\mathbf{p} = (\partial_x u_x, \partial_y u_x, \partial_z u_x, \partial_x u_y, \partial_y u_y, \partial_z u_y)^{\mathrm{T}}$ the linear system can be written as:

$$\mathbf{d} = \begin{pmatrix} \mathbf{d}^1 \\ \mathbf{d}^2 \\ \vdots \\ \mathbf{d}^N \end{pmatrix} = \begin{pmatrix} \mathbf{A}^1 \\ \mathbf{A}^2 \\ \vdots \\ \mathbf{A}^N \end{pmatrix} \mathbf{p} = \mathbf{A}\mathbf{p}$$
 (2.16)

Using least squares inversion, equation 2.16 can be written as:

$$\tilde{p} = \left(A^T C_d^{-1} A\right)^{-1} A^T C_d^{-1} d, \tag{2.17}$$

where \mathbf{C}_d is the covariance matrix of \mathbf{d} . The strain tensor and the rigid body rotation sensor can be resolved by \tilde{p} .

Several studies have suggested that rotational rates can be derived from an array of translational motion measurements, provided the array is of an appropriate size and includes data from at least three stations (e.g., (Bodin et al., 1997; Suryanto et al., 2006; Huang, 2003)

2.4.2 Rotational beamforming

One of the notable properties of rotational motion is that, under the assumption of plane wave propagation, the transverse acceleration and the rotation rate (around a vertical axis) are directly proportional to the horizontal phase velocity (Igel et al. 2005; Ferreira and Igel 2009). By focusing on surface waves, it is possible to analyze the rotational motion of Love and Rayleigh waves independently.

Considering Love waves, for a transversely polarized wave propagating along the y-axis, the displacement field can be expressed as:

$$u_x = 0, \quad u_y = A\sin(kx - kct), \quad u_z = 0$$
 (2.18)

where **A** represents the amplitude, **k** the wave number, **c** the phase velocity, and $\omega = kc$ is the angular frequency. Based on equation 2.14, the rotation rate around the vertical axis is the only component with a nonzero value, given by:

$$\dot{\omega}_x = 0, \quad \dot{\omega}_y = 0, \quad \dot{\omega}_z = \frac{1}{2}k^2cA\sin(kx - kct)$$
 (2.19)

The transverse acceleration \mathbf{a}_T from equation 2.18 can be expressed as the second derivative with respect to time:

$$a_T = \ddot{u}_T = -k^2 c^2 A \sin(kx - kct) \tag{2.20}$$

A comparison between Equations 2.19 and 2.20 reveals that their ratio corresponds to a factor of -2c.

$$\frac{a_T}{\dot{\omega}_z} = \frac{-k^2 c^2 A \sin(kx - kct)}{\frac{1}{2} k^2 c A \sin(kx - kct)} = -2c$$
 (2.21)

This relationship indicates that the phase velocity of Love waves can be determined by scaling the amplitude between the transverse acceleration and the vertical rotation measurements observed within the same phase.

The graphical representation provided in Figure 2.4 illustrates that the transverse polarization of Love wave particle motion generates vertical rotational motion. Since Rayleigh waves generate elliptical particle motion, rotation sensors are used to measure motions along horizontal axes (Figure 2.4).

Rayleigh waves propagating in the x direction and polarized along two axes

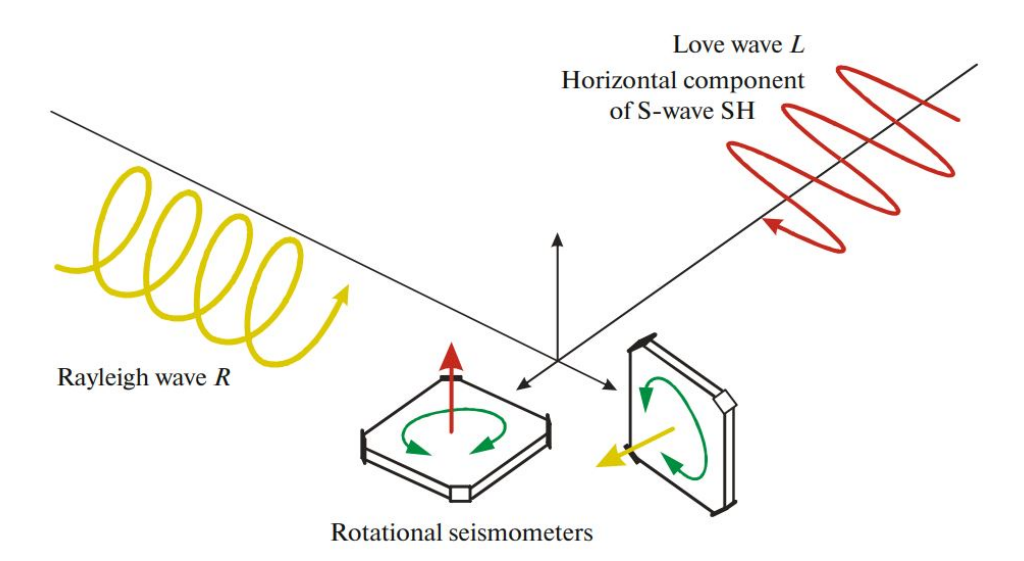


Figure 2.4: Rotational motions induces by Rayleigh (yellow line) and Love (red line) waves (Kislov and Gravirov, 2021).

can be mathematically described as:

$$u_x = A \sin \xi \sin(kx - kct),$$

$$u_y = 0,$$

$$u_z = A \cos \xi \cos(kx - kct)$$
(2.22)

Here, $\bf A$ denotes the amplitude, $\bf k$ represents the wavenumber, and $\bf c$ is the phase velocity. The angle ξ , referred to as the ellipticity angle of the Rayleigh wave, defines the eccentricity and the direction of the particle motion's rotation. When $\xi \in (-\pi/2,0)$, the elliptical motion of the Rayleigh wave is retrograde, meaning that the vertical component of oscillation $\bf u_z$ leads the oscillation in the propagation direction by $+\pi/2$ radians. Conversely, when $\xi \in (0,\pi/2)$, the wave exhibits prograde motion. For $\xi=0$ or $\xi=\pm\pi/2$, the polarization is purely vertical or horizontal, respectively. The term $|\tan\xi|$ quantifies the ellipticity of the Rayleigh wave. Rotational motions induced by Rayleigh waves are confined to the ω_x and ω_y components. When a Rayleigh wave is horizontally polarized (i.e., $\xi=\pm\pi/2$), no rotational motions are generated. Based on Equation 2.14, the transverse rotation rate for Rayleigh waves can be expressed as:

$$\frac{a_z}{\dot{\omega}_y} = \frac{aAk^3c^2\cos\xi\cos(kct - kx)}{aAk^3c\cos\xi\cos(kct - kx)} = c \tag{2.23}$$

Similar to Love waves, the phase velocity of Rayleigh waves can be determined by comparing the amplitude of vertical acceleration to horizontal rotation measurements.

In addition to phase velocity, information about the azimuth of surface waves can also be derived by analyzing the correlation between rotational and acceleration measurements in the azimuthal domain. Using a theoretical back azimuth range of 0–360 degrees, horizontal acceleration can be estimated through a grid search over the azimuthal domain. The correlation coefficient is calculated for each back azimuth value, comparing the rotational and acceleration measurements. The azimuth associated with the maximum correlation coefficient is identified as the propagation direction of the surface waves.

Chapter 3

Data availability

3.1 Data availability for correlation wavefield

As stated in the introduction, the initial two research questions of this study are to assess the influence of persistent, uncontrolled noise sources particularly oceanic microseisms on the correlation wavefield. To investigate this, the study focuses on the European region, which is located in proximity to one of the strongest oceanic noise sources, the North Atlantic Ocean. For this purpose, continuous vertical-component seismograms recorded between January-December 2019 and January-December 2021 by 19 broadband stations were analyzed. Among these, 13 stations belong to the German Regional Seismic Network (GR), forming the Gräfenberg array in Germany. The remaining six broadband stations are standalone stations from different national seismic networks: the Italian National Seismic Network (IV) in Italy, the Portuguese National Seismic Network (PM) in Portugal, the Polish Seismological Network (PL) in Poland, the RESIF permanent network (FR) in France, and the Northern Finland Seismological Network (FN) in Finland. The spatial distribution of the seismic array and the six standalone stations is depicted in Figure 3.1. All seismic data used in this study are openly accessible via the FDSN database. The rationale behind selecting one array and six standalone stations is further discussed in Chapter 5. Figure 3.2a illustrates the geometry of the Gräfenberg array.

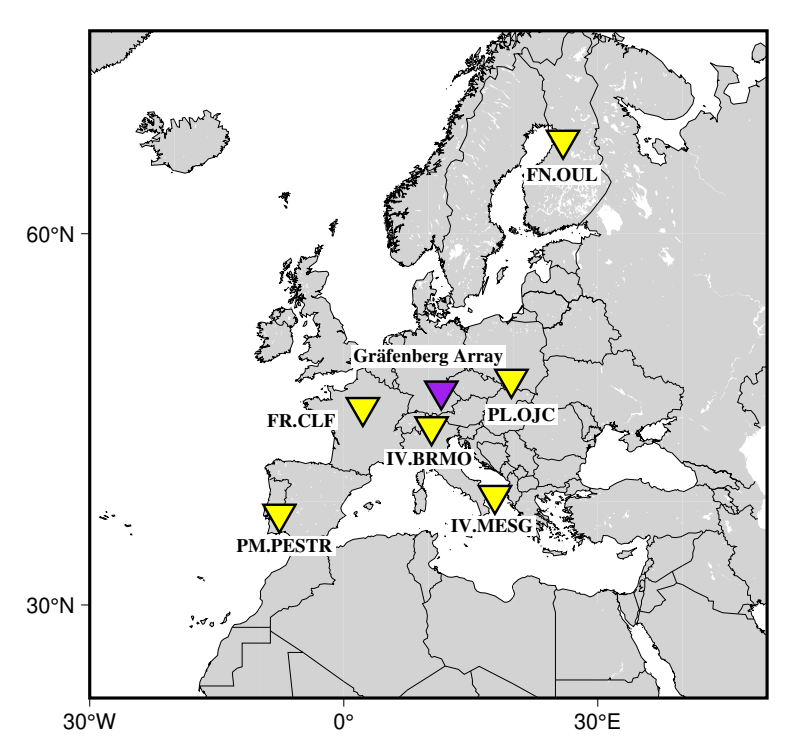


Figure 3.1: The location of the Gräfenberg array in Germany (purple triangles) along with six single master stations distributed across different azimuthal ranges (yellow markers). The master stations are located in Italy (IV.BRMO, IV.MESG), Poland (PL.OJC), France (FR.CLF), Finland (FN.OUL), and Portugal (PM.PESTR).

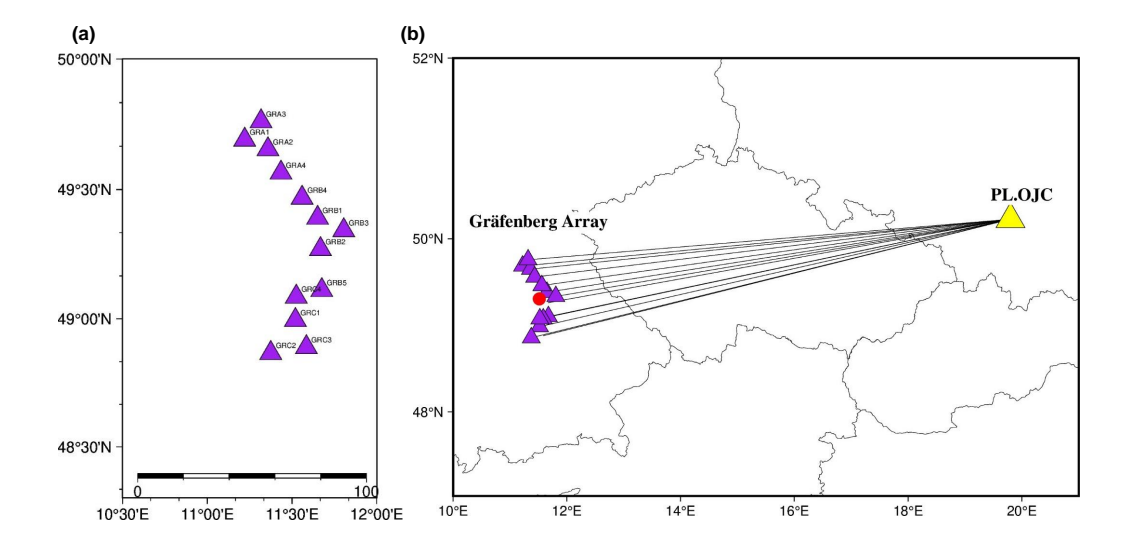


Figure 3.2: (a) Geometry of the Gräfenberg seismic array, consisting of 13 broadband stations with three components and an aperture of 100 km. (b) Schematic representation of the cross-correlation computation, where PL.OJC is considered as the master station (virtual source), and the stations within the Gräfenberg array act as receivers.

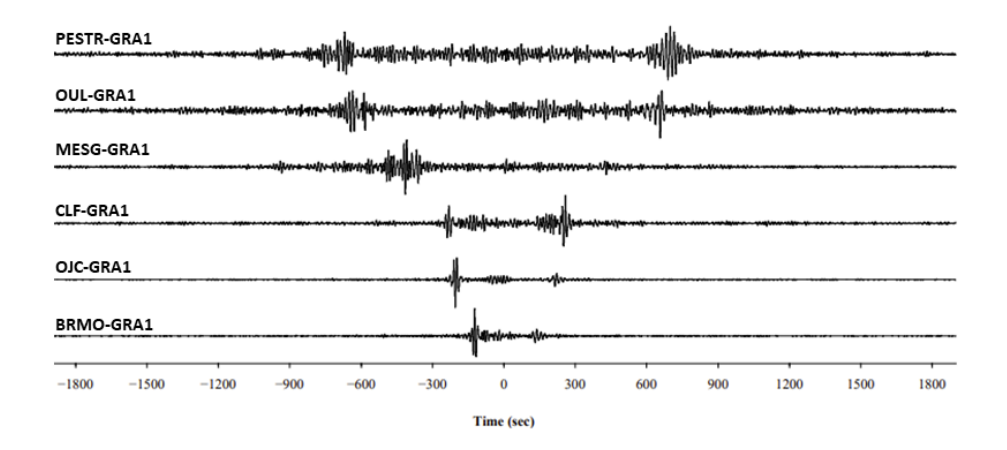


Figure 3.3: Two years reference cross correlations computed between master stations and GRA1 station in Gräfenberg array. This signal filtered in the Secondary microseism frequency band (0.1-0.3 Hz)

These six broadband stations: IV.BRMO, IV.MESG, PM.PESTR, PL.OJC, FR.CLF, and FN.OUL are designated as master stations (virtual sources). For each of these master stations, correlation wavefields are computed with all Gräfenberg seismic array stations, treating them as receivers. Once the preprocessed daily recordings for all stations were prepared (see Section 2.2), the correlation wavefields between each master station and the Gräfenberg array stations were computed. A schematic representation of this virtual source-receiver geometry is presented in Figure 3.2b, where PL.OJC is shown as the master station, while the Gräfenberg array stations serve as receivers. This procedure was systematically repeated for all other standalone master stations. Figure 3.3 displays the reference correlation functions obtained between each master station and GRA1.

3.1.1 Data availability for single-component beamforming

In this study, our focus is on investigating oceanic microseismic noise. To achieve this, we utilize the Gräfenberg array in Germany, which has an aperture of approximately 100 km, making it suitable for analyzing primary and secondary microseismic frequency bands. We apply cross-correlation beamforming to the vertical-component continuous seismic recordings for the entire years of 2019 and 2021, using data from 13 stations in this array. The results obtained provide valuable insights into the dominant sources responsible for microseismic

noise and their seasonal variations within the study region.

To further explore the influence of oceanic sources on the correlation wavefield, we define six master stations positioned at different azimuths surrounding the Gräfenberg array. These master stations are selected at sufficiently large distances to satisfy the beamforming assumption of planar wavefields. For each master station, the beamforming method is applied to the reference correlation wavefields as listed in Table.1, ensuring that the analysis is conducted for each master station individually.

The primary objective of this investigation is to analyze beamforming results on the correlation wavefield, identifying dominant source contributions as the wavefield propagates from each master station and is recorded across the array. These results are then compared with beamforming analysis performed directly on the raw seismic recordings within the Gräfenberg array (see Chapter 4).

3.2 Data availability for three-component beamforming

In the three-component beamforming method, we aim to address the final research question outlined in the introduction. Unlike the previous approach, which focused on correlation wavefields, this method exclusively analyzes raw three-component seismic recordings from selected seismic arrays. Our primary objective is to investigate the seasonal variations of primary and secondary microseisms, along with their wave propagation mechanisms, specifically the polarization of Love and Rayleigh waves. This will be compared to results obtained with rotational beamforming (see Section 3.3)

To achieve this, we conduct a long-term data analysis using four years of continuous seismic recordings from 2016 to 2020. Two seismic arrays have been selected for this study: the NOA (NORSAR) array in Europe and a combination of stations from the Southern California Seismic Network (CI) and the ANZA Regional Network (AZ) in the United States. The NOA array is a large-aperture

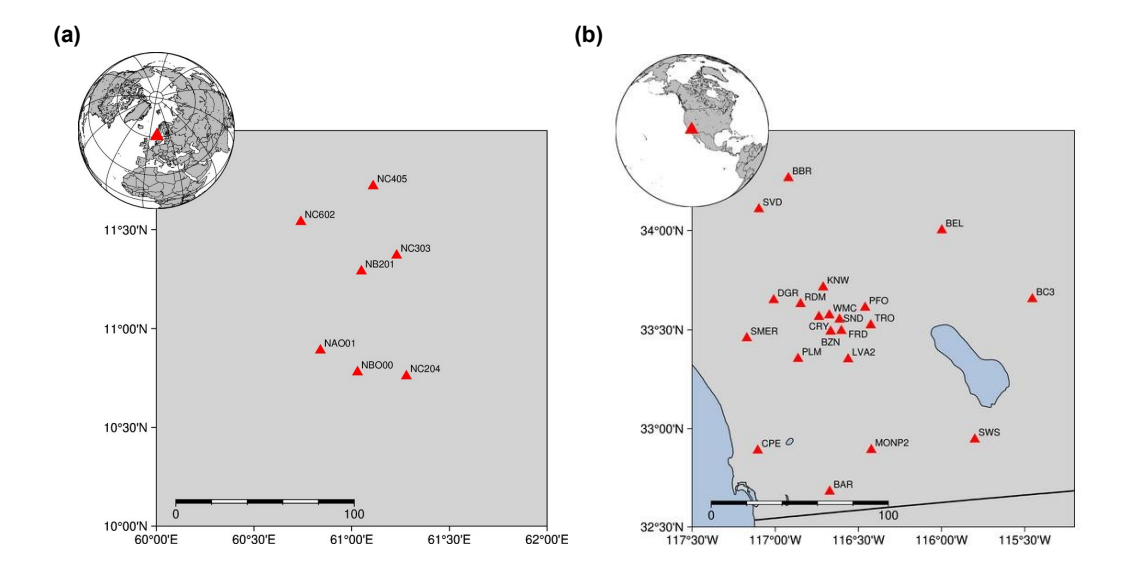


Figure 3.4: Arrays used for the three-component beamforming method: (a) The NOA array in Norway which consists of multiple three-component stations with subset arrays. Each sub-array is equipped with one three-component broadband sensor, with an aperture diameter of 73.9 km (b) A combination of 21 three-component broadband stations from the CI and AZ networks in California, with a total aperture of 173.9 km.

(73.9 Km) seismic array located in near Hamar in southern Norway (top inset plot in Figure 3.4), consisting of multiple subarrays equipped with broadband and short-period seismometers, providing high-resolution observations of seismic waves. Each sub-array is equipped with one three-component broadband sensor. For the purpose of our three-component beamforming analysis, we consider only a subset of seven three components stations. The configuration of these selected stations within the NOA array is shown in Figure 3.4a.

The second array, consisting of stations from the CI and AZ networks (aperture 173.9 km), is located along the west coast of the United States, near the North Pacific Ocean (tope inset plot in Figure 3.4). This network includes 21 stations, all equipped with three-component broadband sensors. The spatial configuration of these stations is illustrated in Figure 3.4b.

3.3 Data availability for rotational beamforming

Array-derived rotation (ADR) and beamforming impose different requirements on the size and spacing of seismic arrays, even when targeting the same wavelength. This discrepancy necessitates the use of at least two different arrays. The ADR method assumes a uniform spatial strain tensor (Equation 2.12 in Section 2.3), and to minimize errors, the optimal array size should be approximately one-quarter of the maximum wavelength (Spudich & Fletcher, 2008). Given the maximum frequency of interest, the relationship between frequency, target wavelength, and array aperture size can be expressed as follows:

$$f_{\text{max}} = \frac{c}{\lambda} = \frac{c}{4r} \tag{3.1}$$

For this study, we focus on oceanic microseisms within the primary and secondary frequency bands (0.05–0.2 Hz). Based on this frequency range, the required array aperture should be less than 1.8 km. However, due to the sparse distribution of arrays globally, identifying suitable arrays for ADR analysis is challenging.

To address this, we first selected two optimal array sizes: the Piñon Flat Array (PFO) in the United States and the ARCES array in Norway. Next, to ensure a fair comparison with the three-component beamforming results, we selected seismic arrays in close geographic proximity to the ADR arrays whenever possible namely, the CI & AZ seismic arrays in the United States and the NOA array in Europe (see Figure 3.4).

The ARCES array, located near Karasjok in northern Norway, lies in proximity to the Barents and Norwegian Seas and the North Atlantic Ocean. This array comprises 25 seismic stations arranged in concentric rings, each equipped with three-component broadband sensors.

The configuration of these broadband stations, with an aperture of 1.7 km, is illustrated in Figure 3.5a. The Pinon Flat Array (PFO) consists of 13 three-

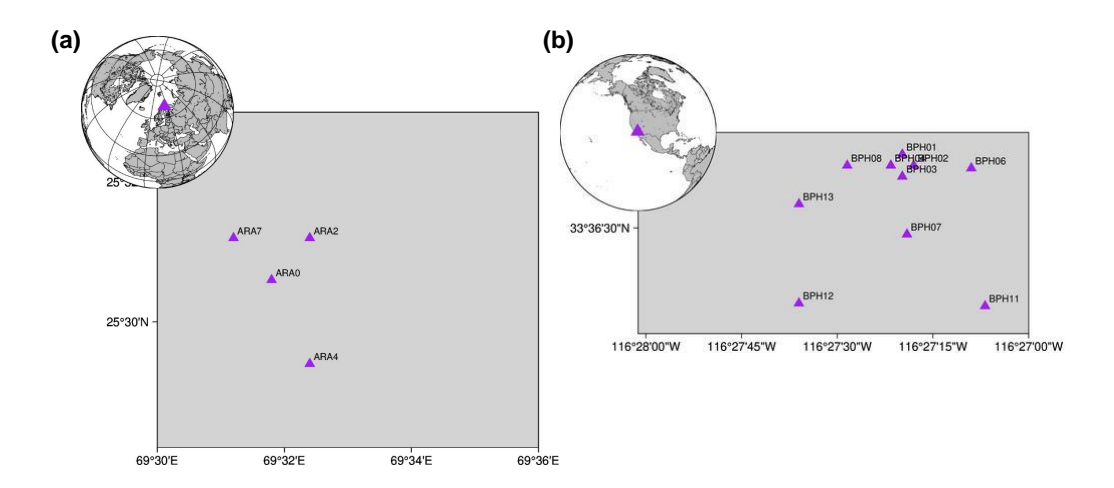


Figure 3.5: Arrays used for the Array-Derived Rotation (ADR) method: (a) The ARCES array in Norway, consisting of four three-component stations with an aperture of 1.7 km. (b) The Piñon Flat array in California, comprising 13 three-component stations with an aperture of 1.08 km

component broadband seismic stations in California, with an aperture of 1.08 km. The configuration of this array is shown in Figure 3.5b.

Chapter 4

Imprints of microseism noise sources on coda of the correlation wavefield

The present chapter is intended to address the first two research questions posed in the introduction of this thesis:

- How do persistent microseism noise sources influence the different parts of correlation wavefields?
- Do seasonal variations affect the stability of the direct arrival or later parts of the correlation wavefield?

4.1 Continuous isolated noise sources induce repeating waves in the coda of ambient noise correlations

Sven Schippkus¹, Mahsa Safarkhani¹, Celine Hadziioannou¹

¹ Institute of Geophysics, Center for Earth System Research and Sustainability (CEN), Universitat Hamburg, Hamburg, Germany

Published in Seismica

Author Contribution of Mahsa Safarkhani: Conceptualization, Data curation, Investigation

This study investigates the influence of persistent isolated noise sources on coda of the correlation wavefields. This study demonstrated that continuously acting isolated noise sources, such as ocean microseisms, produce repeating wave patterns throughout the entire correlation function, which propagate from the isolated source location. These waves coincide with and are more coherent than those from other sources, suggesting a impact on the ambient noise correlation wavefields.

The full version of this paper is provided in the supplementary materials of this thesis (See Supp. A1).

4.2 Imprints of time-dependent microseism source distributions on the coda of correlations (Journal Submission)

Mahsa Safarkhani¹, Sven Schippkus¹, Celine Hadziioannou¹

In review at Geophysical Journal International

¹ Institute of Geophysics, Center for Earth System Research and Sustainability (CEN), Universitat Hamburg, Hamburg, Germany

Abstract

Seismic interferometry, applied to continuous seismic records, yields correlation wavefields that can be exploited for information about Earth's subsurface. The coda of the correlation wavefield has been described as multiply scattered waves that are highly sensitive to crustal heterogeneity and its changes. Therefore, the coda of consecutive correlation wavefields allows to monitor velocity variations over time to detect weak changes in the medium at depth. Ocean microseisms, generated by ocean-land interactions, are the dominant continuous source of seismic energy at frequencies below 0.5 Hz. It is well-understood that these oceanic sources are not homogeneously distributed over Earth and change over the seasons, which commonly results in asymmetric correlation wavefields from seismic data. The impact of these seasonal changes on the coda of the correlation wavefield is typically considered negligible. In contrast, we demonstrate that oceanic noise sources and their changes directly impact the composition of the coda. We compute correlation wavefields between several master stations throughout Europe and the Gräfenberg array in Germany. We beamform these correlation wavefields, in the microseism frequency band, to detect coherent waves arriving at the Gräfenberg array. We perform this analysis for a two-year period, which enables us to compare variations in source direction over the seasons. We find seismic waves arriving from dominant sources to the North-Northwest of Gräfenberg in boreal winter (with slownesses corresponding to surface waves) and towards the South in summer (with slownesses corresponding to body waves) throughout the entire correlation wavefield, including its late coda. Beamforming the original recordings before cross-correlation confirms that the seasonally dominant source regions are directly detected also in the correlation wavefield coda. We derive that seismic waves propagating from isolated microseism source regions will be present in correlation wavefields even if the master station, or "virtual source", used for correlation recorded no physical signal at all. The findings we present raise concerns about velocity monitoring approaches relying on the coda being comprised exclusively of scattered waves. Our results also suggest that higher-order correlations do not

achieve an effectively more homogeneous source distribution, and instead may even enhance such bias.

Coda waves – Seismic noise – Seismic interferometry – Wave propagation – Wave scattering and diffraction

4.3 Introduction

Passive seismic methods, which utilize the ambient seismic noise wavefield, offer significant opportunities for both monitoring and imaging applications. Green's functions extracted from noise correlation wavefields between pairs of stations enable seismologists to access information about the Earth's crust and upper mantle on regional to global scales (e.g., Shapiro et al., 2005; Yao et al., 2006; Roux et al., 2011; Shirzad and Shomali, 2014). Using omnipresent seismic noise recordings to produce virtual seismic sources at receiver locations allows for the derivation of velocity structures without relying on seismic activity or controlled seismic sources (e.g., Lobkis and Weaver, 2001; Shapiro and Campillo, 2004; Wapenaar and Fokkema, 2006). Furthermore, in addition to standard surface wave tomography using direct arrivals of the correlation function, the coda of this correlation wavefield has also been essential in providing continuous measurements for monitoring applications (Snieder et al., 2002; Sens-Schönfelder and Wegler, 2006; Richter et al., 2014; Hillers et al., 2015). Coda wave interferometry, which involves tracking phase shifts in multiplyscattered physical arrivals, allows us to detect subtle temporal variations in seismic velocity (e.g., Sens-Schönfelder and Wegler, 2006; Brenguier et al., 2008; Donaldson et al., 2017).

Accurate reconstruction of the Green's function through seismic interferometry relies on an isotropic noise source distribution (Snieder, 2004; Derode et al., 2003; Larose et al., 2005; Shirzad et al., 2022). In many studies, the noise wavefield used consists primarily of ocean microseisms, which dominate the low-frequency range (0.05-0.5 Hz). The continuous interaction between ocean swells and the solid Earth produces two distinct peaks - the primary and

secondary microseism (Longuet-Higgins, 1950; Kedar et al., 2008; Stutzmann et al., 2012; Ardhuin et al., 2015; Juretzek and Hadziioannou, 2016). Yet, the anisotropic spatial distribution of microseisms and their seasonal variations lead to incomplete reconstruction of Green's functions.

Several studies have revealed biases in seismic interferometry, caused by nondiffuse wavefields near station pairs (e.g., Tsai, 2009; Yao and Van Der Hilst, 2009; Froment et al., 2010; Tsai, 2010; Schippkus et al., 2022). These investigations focused on direct waves in correlation functions and found that anisotropic source illuminations induce mostly small velocity estimation errors on the order of 1% (Froment et al., 2010). Errors in the estimation of velocity variations of coda waves for monitoring purposes are also expected due to the necessitation of stable source regimes (Hadziioannou et al., 2009; Colombi et al., 2014), and a sufficient scatterer distribution to achieve fully scattered waves in the coda. Schippkus et al. (2023) investigated the effect of persistent isolated noise sources on the correlation wavefield, and found that isolated noise sources can dominate the coda part of the correlation wavefield. The impact of contributions from isolated sources on the coda of the correlation wavefield raises questions about the reliability and uncertainty in monitoring measurements based on correlation wavefields, especially concerning velocity variations induced by natural processes with seasonal variation.

This study highlights the sensitivity of correlation wavefields to spatio-temporal variations in localized microseisms. Our analysis utilises estimated correlation wavefields between six master stations, distributed across Europe, which act as virtual sources, and the Gräfenberg seismic array in Germany. In a next step, we employ beamforming to analyze the directional energy distribution of the correlated wavefield (similar to the approach in Soergel et al. (2023)). Our examination of the correlation wavefield within the frequency band of primary and secondary microseisms (0.05-0.1, 0.1-0.3 Hz) show a constant impact of the ocean microseism source distribution, from the direct arrivals, through coda waves up to the very late lapse times.

4.4 Method

4.4.1 Approach

To evaluate the composition of the coda of the correlation wavefield over the seasons in the microseism frequency bands and how this compares to the recorded seismograms, we rely on beamforming (Baggeroer et al., 1988; Rost and Thomas, 2002; Ruigrok et al., 2017). We beamform continuous seismograms recorded at the Gräfenberg seismic array in Germany to detect the dominant microseism sources. In a second step, we compute correlation wavefields from seismograms recorded at the Gräfenberg array and six master stations throughout Europe and then beamform them, as well.

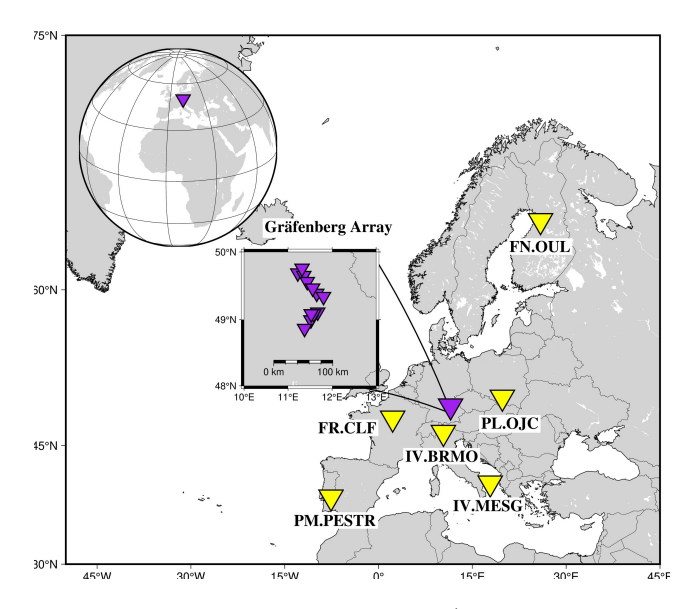


Figure 4.1: The Gräfenberg seismic stations (depicted by purple triangles) are located in Germany, while the master stations (depicted by yellow triangles) are in Poland (PL.OJC), Finland (FN.OUL), France (FR.CRF), Portugal (PM.PESTR), and Italy (IV.MESG, IV.BRMO). The upper and lower inside panels feature a zoomed-out and zoomed-in view of the seismic array, its location, and geometry.

We use vertical component recordings at the Gräfenberg seismic array in Germany, consisting of 13 permanent broadband seismic stations with an aperture of ca. 100 km, and six permanent master stations (PL.OJC, FN.OUL, FR.CLF, PM.PESTR, IV.BRMO, and IV.MESG) surrounding the array (Figure 4.1). The master stations have been chosen to cover a wide range of backazimuths and

different distances (between 360 km and 1980 km) to the Gräfenberg array. Additional master stations would not have provided additional information, as our results below demonstrate. We use recordings from two non-consecutive years (2019 and 2021) for all stations, because some stations have data gaps in 2020. To achieve consistent results across all master stations, i.e., to use exactly the same time periods, and for ease of processing, we disregarded data recorded in 2020 entirely. We correct the recordings for instrument response, and only apply further pre-processing for computing correlation wavefields, not for beamforming the raw recordings. This pre-processing includes cutting the seismograms into one-hour segments, removing the mean and trend, applying temporal normalisation in a five-second moving window, and spectrally whitening in the frequency range from 0.01 Hz to 0.9 Hz (Bensen et al., 2007; Safarkhani and Shirzad, 2019). The pre-processed seismograms are cross-correlated and stacked linearly to yield the correlation wavefields.

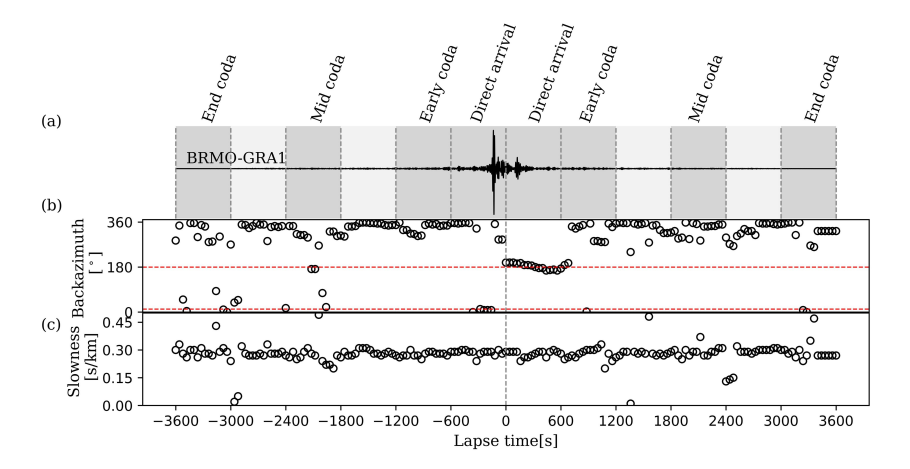


Figure 4.2: Distribution of maximum beam power values for slowness and back azimuth grid searches. (a) illustrates the reference noise correlation function (NCF) used as the primary signal for the beamforming method. The grey shadows represent the 10 minute windowing function centered around the direct Rayleigh waves and later parts of the correlation wavefield. The windows are labelled according to the wavetypes in the correlation wavefield, consisting of the "Direct Arrival", "Early Coda", "Mid Coda" and "End Coda" on both casual and acasual elapsed time sides. Panels (b) and (c) demonstrate the distribution of back azimuths and slowness that correspond to the maximum value of beam power in each sliding window (160 seconds) using the beamforming process. Red dashed lines illustrate the converging and diverging wavefield between the master station and seismic array (master-receiver) on the positive (ca. 180°) and negative (ca. 10°) lapse time sides.

4.4.2 Beamforming

Beamforming is a phase-matching algorithm that allows to detect and extract coherent wavefield contributions from its recordings. In its simplest form, a beam is formed by phase-shifting the seismograms to correct for the expected phase delays between stations for an incident wave recorded on an array and stacking those, often called the delay-and-sum approach (Rost and Thomas, 2002). In a grid search, a wide range of phase-shift combinations are tested that correspond to potential plane waves propagating across the array. We parametrise these plane waves in terms of backazimuth and slowness. Cross-correlation beamforming, similar to Bartlett beamforming (Baggeroer et al., 1988), applies the same delay-and-sum idea to correlation functions between the recordings instead of the recordings themselves, which yields more precise estimates of the dominant source direction and local phase velocity (Ruigrok et al., 2017).

We apply cross-correlation beamforming both to raw continuous recordings of the Gräfenberg array and to the correlation wavefields between the master stations and the array. The cross-correlation beamformer can be written in frequency domain as

$$B = \sum_{\omega} \sum_{j} \sum_{k \neq j} s^*(\mathbf{r}_j) s(\mathbf{r}_k) u(\mathbf{r}_j) u^*(\mathbf{r}_k), \tag{4.1}$$

with ω the angular frequency, B the beampower for a given backazimuthslowness combination, u the recordings and s the synthetic plane-wave Green's functions (also called replica or steering vectors) for all station pairs between stations at \mathbf{r}_j and \mathbf{r}_k .

For illustration purposes, we showcase one example beamforming result on the correlation wavefield between IV.BRMO and the Gräfenberg array in the primary microseism frequency band from 0.05 to 0.1 Hz in detail (Figure 4.2). The two-hour long correlation function between IV.BRMO and GR.GRA1 shows distinct arrivals at negative and positive lapse times in the correlation function (Figure 4.2a). Beamforming in 160 seconds long windows, overlapping by 75%, confirms that these arrivals are direct Rayleigh waves (with slowness ca. 0.3s/km) travelling towards the master station in negative lapse times (backazimuth ca. 10° from North, cf. Figure 4.1), and away from the master station (backazimuth ca. 180°, cf. Figure 4.1) in positive lapse times, respectively (Figure 4.2b, c). This is the contribution to the correlation wavefield usually arising in seismic interferometry (Wapenaar et al., 2005). Throughout the rest of the correlation wavefield, we detect coherent Rayleigh waves arriving from West to Northwest as dominant. These are repeating waves induced by persistent isolated microseism sources (Schippkus et al., 2023). We label lapse time segments as end coda, mid coda, early coda, and direct arrival in negative and positive lapse times (Figure 4.2a) for reference below. In the following, we investigate the averaged beampower distributions within these segments.

4.5 Results

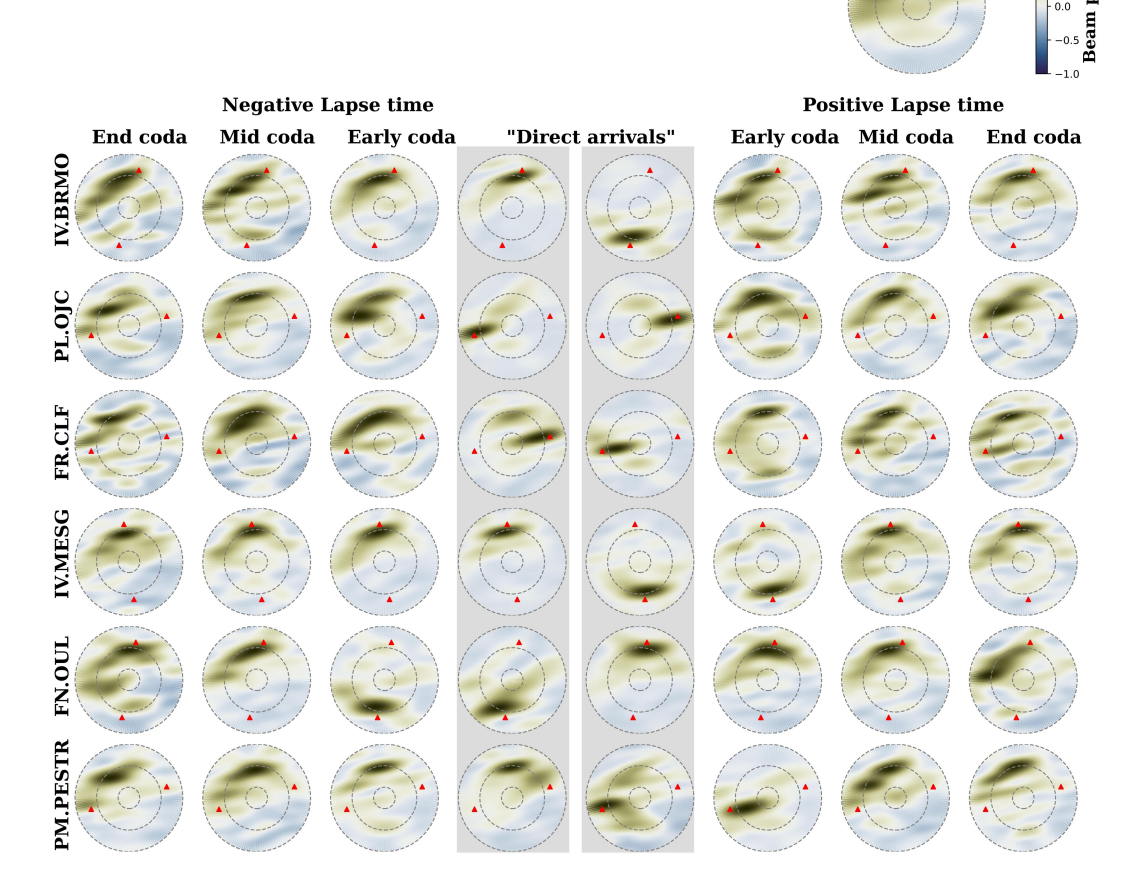
4.5.1 Beamforming on different correlation windows

We apply beamforming to separate lapse time segments of the correlation wavefield, as shown by the gray windows in Figure 4.2(a): direct Rayleigh wave arrival (0 - 600 s), early (600 - 1200 s), mid (1800 - 2400 s), and end (3000 - 3600 s) coda. Within each window, we beamform with the parameters described above (160 sec. windows, 75% overlap) and compute the mean beampower distribution. Figure 4.3 shows the result for the correlation wavefields between all 6 master stations and the Gräfenberg array, filtered within the frequency band of the primary microseism (0.05-0.1 Hz).

To compare the results obtained in each lapse time segment of the correlation wavefield to the original seismic noise wave field, we also show the beamforming output derived from continuously recorded raw data across 13 stations in the Gräfenberg seismic array (Figure 4.3, top right polar plot). The raw data underwent instrument response correction, detrending and filtering within the 0.05-0.1 Hz frequency range, followed by decimation to 1 Hz. Beamforming

was performed using the same parameters and averaging as for the correlation waveforms.

As noted in the previous section, in the 'direct arrival' segment, coherent energy consistently originates from the direction of the master station, represented by the red triangles in this figure. This direct arrival suggests that the coherent waves follow a uniform and predictable pattern as they propagate from the master station's geometry to the receivers, as expected based on interferometry principles. On the other hand, for later lapse times in the coda segments, one would expect the beamformer output to become less stable, because the coda is commonly thought to be comprised of scattered waves. This decrease in stability would continue until no coherent energy is recovered, as the scattered wavefield attenuates and becomes more incoherent. Instead, for all master-station and Gräfenberg-array configurations, all coda segments display a coherent and distinct beampower maximum, originating from the north-northwest of the Gräfenberg array. This corresponds to the main direction of primary microseism sources, as confirmed by the beamforming results on raw data (Figure 4.3, top right panel). This is observed even for the very late coda (up to 1 hour lapse time). At these very late lapse times, long after the scattering coda should have ended, no physical wavefield from ambient noise is expected in the reconstructed Green's function between the master stations and the Gräfenberg array. This reaffirms that persistent, isolated sources, like ocean microseisms, can produce coherent, repeated wave arrivals even at the end of correlation functions. Continuous excitation from specific geographic sources appears to drive this phenomenon, indicating that this repeating energy can influence the later parts of the wavefield, which is often presumed to be random or entirely scattered, with limited source-related influence. The question arises how sensitive these results are to seasonal source variations.



Raw data

Figure 4.3: Evaluation of beamforming results on 10-minute correlation wavefield windows within the primary microseism frequency band (0.05-0.1 Hz). Slowness values ranging from 0 to 0.5 s/km are indicated with dashed line circles. This analysis includes all viable master station pairs, namely IV.BRMO, PL.OJC, FR.CLF, IV.MESG, FN.OUL, and PM.PESTR. Distinct segments are labelled to indicate the location of the wavetypes in the correlation wavefields including, the direct arrivals highlighted in gray, early coda, mid coda, and end coda on both positive and negative elapsed time sides. The spatial arrangement/geometry of the Gräfenberg (GR) seismic array and master stations is depicted by red triangles based on azimuth and backazimuth. Based on the master-receiver wavefield contribution, most coherency in Direct arrivals observed in location of master station and GR array in negative and positive lapse time sides. Due to the large distance between the Master stations FN.OUL, IV.MESG, PM.PESTR and GR array, the direct arrival is still visible in the early coda segment even though it arrives after 10 minutes. The upper panel of the figure presents the result of beamforming on the continuous raw data recorded within the GR seismic array stations.

4.5.2 Temporal variation of correlations' coda: impact of seasonal ocean microseism variation

To investigate the influence of changing noise sources on the correlation's coda, we consider the seasonal variation of the secondary microseism (0.1-0.3 Hz) (e.g., Stutzmann et al., 2009; Hillers et al., 2012; Juretzek and Hadziioannou, 2016). We focus on the secondary microseism, because they are more susceptible to seasonal variations than primary microseisms (Lepore and Grad, 2018; Gualtieri et al., 2021a). Reference correlation wavefields were computed for two sixmonth periods: April to September (boreal summer) and October to March (boreal winter) in the specified frequency range. The beamforming results for the correlation wavefields between master stations IV.BRMO, PL.OJC and the Gräfenberg array are shown in Figure 4.4.

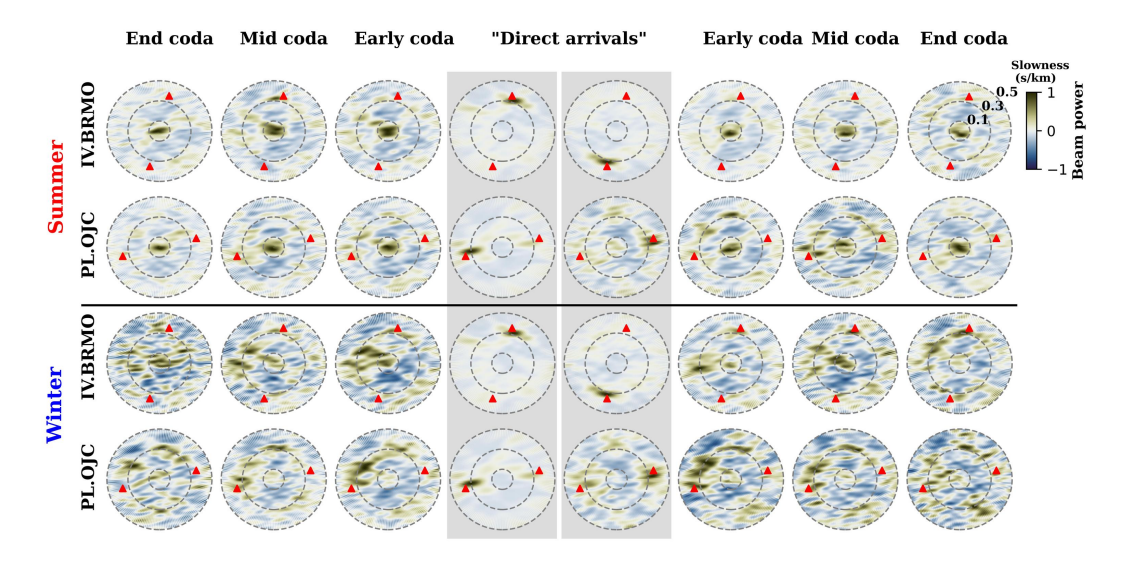


Figure 4.4: Seasonal variation of coda correlation wavefields in the secondary microseism band (0.1-0.3 Hz) with respect to the oceanic regime for the IV.BRMO and PL.OJC master stations during summer and winter. Dashed line circles indicate slowness values from 0-0.5 s/km. The gray window highlights direct arrivals in positive and negative lapse time sides. Non-direct arrivals including early, mid and end coda are titled and red triangles show the geometry of the seismic array and master stations.

The direct arrivals remain stable across both winter and summer, confirming the presence of Rayleigh waves with a slowness of ca. 0.3 s/km (Figure 4.4). This stability suggests that these direct arrival windows are dominated by waves traveling between the master stations and the Gräfenberg array, unaffected by

seasonal variations. In contrast, the coda, particularly the later part of the correlation wavefield, exhibits significant seasonal differences (Figure 4.4). In boreal winter, Northern hemisphere storms dominate, leading to higher surface wave energy from northern directions (Figure 4.4). During summer time, when the strongest storms are located in the Southern Hemisphere, and the noise cross-correlations show dominant arrivals with very low horizontal slowness arriving from South, which are likely body waves impinging from below (Figure 4.4).

4.5.3 Influence of the master station

In the coda of the correlation wavefields, we detect persistent isolated microseism sources as dominant, regardless of the frequency band and chosen master station (Figs 4.3, 4.4). This suggests the master station has little impact on the phase match during beamforming of these parts of the correlation wavefield. In the following, we derive why this is the case.

Consider a wavefield u, recorded at position \mathbf{r} , induced by a single isolated noise source located at \mathbf{r}_N

$$u(\mathbf{r}) = N_I G(\mathbf{r}, \mathbf{r}_N), \tag{4.2}$$

with G the Green's function, and N_I the source term of the isolated noise source, written in frequency domain. The cross-correlation of this wavefield recorded by two stations at \mathbf{r} and at \mathbf{r}_M (the master station) is given by

$$C(\mathbf{r}, \mathbf{r}_M) = u(\mathbf{r})u^*(\mathbf{r}_M) = |N_I|^2 G(\mathbf{r}, \mathbf{r}_N)G^*(\mathbf{r}_M, \mathbf{r}_N). \tag{4.3}$$

The auto-correlation of the source term convolved with the cross-correlation of the Green's functions between source and sensors is the contribution by an isolated noise source to the correlation wavefield (Equation 6 in Schippkus et al., 2022). In the present study, we beamform the correlation wavefield, i.e., we replace the recordings u in the beamformer (Equation 4.1) with correlation

functions C (Equation 4.3). The beampower is then

$$B = \sum_{\omega} \sum_{j} \sum_{k \neq j} s^*(\mathbf{r}_j) s(\mathbf{r}_k) C(\mathbf{r}_j, \mathbf{r}_M) C^*(\mathbf{r}_k, \mathbf{r}_M), \tag{4.4}$$

which gives

$$B = \sum_{\omega} \sum_{j} \sum_{k \neq j} s^*(\mathbf{r}_j) s(\mathbf{r}_k) |N_I|^2 |N_I|^2 G(\mathbf{r}_j, \mathbf{r}_N) G^*(\mathbf{r}_M, \mathbf{r}_N) G^*(\mathbf{r}_k, \mathbf{r}_N) G(\mathbf{r}_M, \mathbf{r}_N),$$
(4.5)

and simplifies to

$$B = \sum_{\omega} \sum_{j} \sum_{k \neq j} \underbrace{s^*(\mathbf{r}_j) s(\mathbf{r}_k) |N_I|^2 G(\mathbf{r}_j, \mathbf{r}_N) G^*(\mathbf{r}_k, \mathbf{r}_N)}_{\text{equivalent to beamforming } u \text{ (Equation 4.1)}} \underbrace{|N_I|^2 |G(\mathbf{r}_M, \mathbf{r}_N)|^2}_{\text{master station influence}}. (4.6)$$

The contribution of the master station to the beamformer is the auto-correlation of the isolated source term $|N_I|^2$ convolved with the auto-correlation of the Green's function between isolated noise source and master station $|G(\mathbf{r}_M, \mathbf{r}_N)|^2$. These terms carry no phase information. Therefore, the master station does not affect the phase match of the correlation wavefield beamformer in the case of a single isolated noise source. Our results, although they are impacted by more complex source distributions than a single isolated source, can be largely explained by this. The impact of the master station in the beamformer is limited to weighting frequencies recorded with high amplitude at \mathbf{r}_M higher, which is likely negligible in practice.

We compute correlation functions between the seismograms recorded at the Gräfenberg array and a uniformly random noise time series ("numerical noise") and beamform them to confirm the irrelevance of the master station for the detection of isolated noise sources (Figure 4.5). A sample correlation function showcases the lack of distinct arrivals (Figure 4.5a). Beamforming all 13 correlation functions in the primary microseism frequency band (0.05 - 0.1 Hz, as in Figure 4.3) detects coherent surface waves arriving from West to Northwest as dominant at all lapse times, including at times that previously contained direct waves propagating between the master stations and the array (Figure 4.5b). This confirms our derivation above and reaffirms that ocean

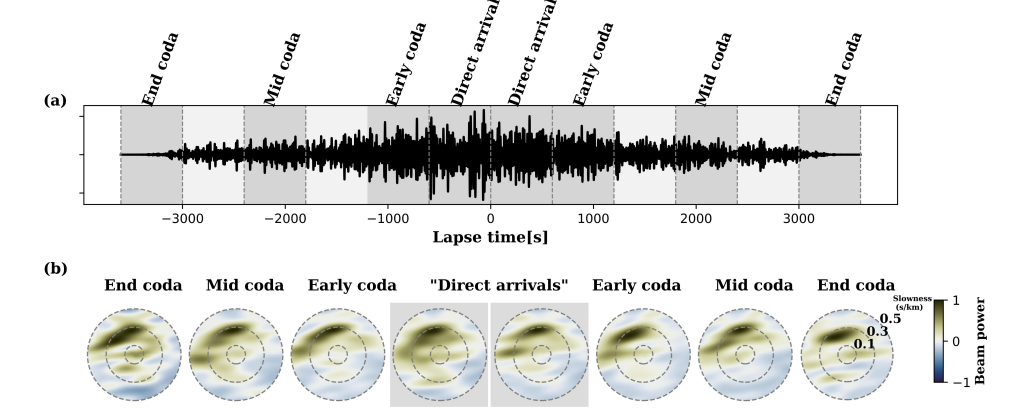


Figure 4.5: Applying correlation beamforming on random/artificial recorded data in the primary frequency band (0.05-0.1~Hz). Dashed line circles indicate the slowness values from 0-0.5 s/km. (a) illustrates the reference noise correlation function (NCF) between the master station recording of random-generated noise and GRA1 station. A 10-minute windowing function was applied to the NCF prior to beamforming, with each window being labelled according to the position of wave types in the correlation wavefield. The beamforming results of dim grey windows are shown in (b).

microseisms act as isolated noise sources (Schippkus et al., 2023). The master station recording is self-evidently required for the correlation wavefield to contain physical waves travelling between the master and array stations. In this study, we observe both the direct arrivals travelling to and from the master station, as well as repeating waves from the isolated sources (Figs 4.2 - 4.4).

4.6 Discussion

In noise interferometry, it is commonly assumed that the seismic wavefield is fully scattered or, equivalently, induced by an isotropic source distribution, such that cross-correlation of the wavefield recorded at two positions yields the Green's function (Wapenaar and Fokkema, 2006). In that case, the later parts of this correlation wavefield, i.e., its coda, contain only multiply scattered waves propagating towards and originating from the master station at negative and positive lapse times, respectively. Existing velocity monitoring approaches exploit these scattered waves for time-dependent information about Earth's structure (Sens-Schönfelder and Wegler, 2006; Brenguier et al., 2008). Our

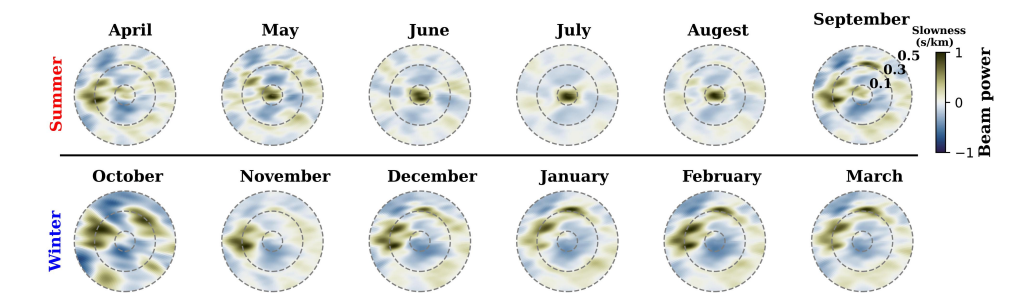


Figure 4.6: Seasonal variation shown in the beamforming results of the raw data recordings at 13 stations of the Gräfenberg seismic array within 12 month of 2019 in the secondary frequency band (0.1 - 0.3 Hz). Dashed line circles indicate the slowness values from 0-0.5 s/km. Top panel shows the 6 month related to the boreal summer (i.e. April-September). Bottom panel shows the beamforming results for 6 months related to winter (i.e October-March).

results show that the correlation wavefield coda is dominated by repeating waves propagating from isolated ocean microseism sources instead (Figs 4.2,4.3), as has been suggested by Schippkus et al. (2023). We further demonstrate that the seasonal variation of secondary microseisms due to changes in storm activity maps directly into the coda parts of the correlation wavefield (Figure 4.4). Finally, we explain why this effect occurs irrespective of the master station (Figure 4.5). These results raise concerns about velocity monitoring based on scattered waves, and have significant implications for higher-order correlations, which we discuss in the following.

First, we discuss the seasonal variations observed in the secondary microseism. During the boreal winter months, we find that surface waves arriving at the Gräfenberg array from the Northwest dominate the coda of the correlation wavefield (Figure 4.4). These detections are consistent with the results from beamforming the original recordings recorded during winter (Figure 4.6). This pattern corresponds to well-known dominant source regions for secondary microseism in the Northern Atlantic which are primarily active during winter months (Friedrich et al., 1998; Chevrot et al., 2007; Juretzek and Hadziioannou, 2016). During the summer months, we observe that body waves with apparent velocities exceeding 10 km/s dominate, arriving from the South. This dominance is evident both in the coda of the correlation wavefield (Figure 4.4) and in

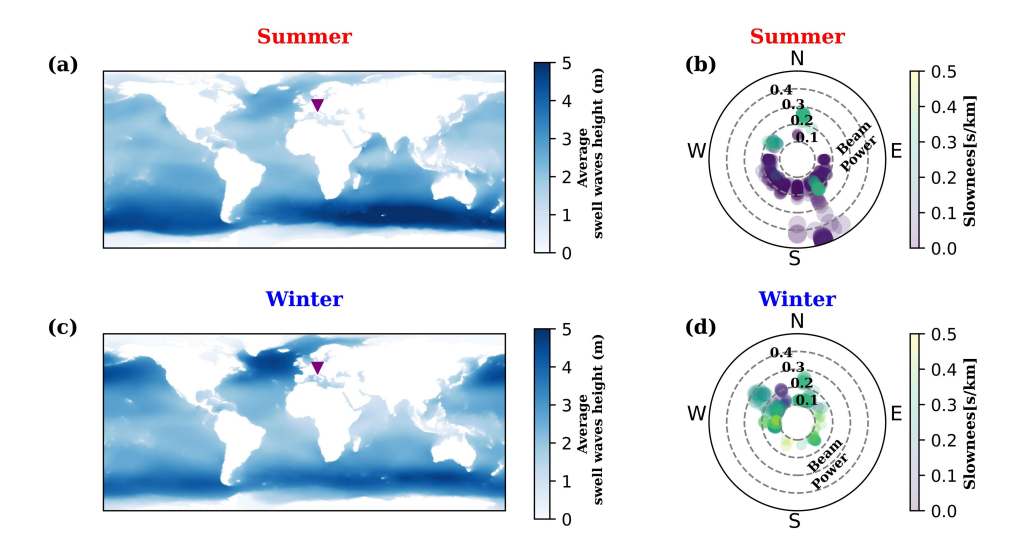


Figure 4.7: Swell wave height output from the WAVEWATCH III model. in summer (a) and winter (c) 2019. The purple triangle indicates the location of the Gräfenberg seismic array. The distribution of maximum beam power values versus backazimuth is shown for one of the master stations during summer (b) and winter (d). The color map displays the slowness values for maximum beam dots ranging from 0-0.5 s/km in summer and winter.

the original recordings (Figure 4.6). Prior research has identified teleseismic body waves within the ambient seismic wavefield, particularly those emanating from distant storm systems (e.g.Gerstoft et al. (2008); Landès et al. (2010); Zhang et al. (2023). Our observations are consistent with Lu et al. (2022), who indicated that during northern hemisphere summers, subcritical P waves are prevalent and play a significant role in the seasonal fluctuations of horizontal-to-vertical seismic amplitudes. They concluded that these waves originate from the Southern Hemisphere, where winter conditions prevail and ocean wave activity is elevated, with these seismic waves becoming particularly detectable during periods of low wave activity in the Atlantic.

The polar plots in Figure 4.7 depict the best direction of arrival, slowness (by color) and beampower (by distance from center) over 2019, which helps showcase the seasonal differences in dominant directions of arrival. The Gräfenberg array geometry is well-suited for the detection of primary and secondary microseism surface waves (Juretzek and Hadziioannou, 2016). However, the array response is not ideal for the discrimination of body waves, as can be seen from Figs 4.4 and 4.6, and which motivates the alternative representation in Figure 4.7. Still,

the measured apparent velocities clearly suggest that body waves dominate in the summer months. Although the estimation of the direction of arrival is less well-constrained, it points almost exclusively to Southerly directions, in agreement with the dominant storm activity in the Southern hemisphere during this time.

We compare this directional dependence in the two seasons and with maps of average significant wave height, extracted from WAVEWATCH III hindcasts (Tolman, 2014). Although significant wave heights are not exactly equivalent to maps of seismic wave generation, they can act as a proxy for regions where high seismic noise generation is expected. In practice, regions with high significant ave height are closely linked but are sometimes found to agree better with seismically detected microseism source locations than modelled seismic source terms based on ocean hindcasts (Igel et al., 2023).

Scattered waves in the coda of correlation wavefields have been exploited to monitor, among other targets, volcanoes (Sens-Schönfelder and Wegler, 2006; Maass et al., 2024), fault damage and healing (Brenguier et al., 2008; Liu et al., 2018), groundwater levels (Lecocq et al., 2017; Mao et al., 2022), and ice or snow cover (Guillemot et al., 2021; Steinmann et al., 2021; Lindner et al., 2021). Because the coda of correlation wavefields appears to behave much like the coda of an earthquake (Campillo, 2006), monitoring methods have been developed under the strong assumption that the coda of correlations is comprised of nothing but scattered waves (Lobkis and Weaver, 2003; Colombi et al., 2014; Mikesell et al., 2015; Wang and Yao, 2020). Our results show that repeating waves induced by isolated noise sources may dominate instead, and that these repeating waves are directly controlled by the changing source regime (Figure 4.4). This raises concerns about the validity of monitoring results based on the scattered-waves assumption. Changing source conditions have been shown to produce velocity errors for the direct arrivals on the order of 1% (Froment et al., 2010) and it appears likely that similar changes may be induced in the coda. This magnitude of potential error is often negligible in applications where much stronger velocity contrasts are imaged, e.g., in crustal tomography (Lu et al., 2018; Schippkus et al., 2018). However, detected velocity variations

are often on the order of 0.1% (e.g., Brenguier et al., 2008; Hadziioannou et al., 2011), where errors on the order of 1% could potentially render results useless. It remains unclear how exactly changes in self-correlated isolated noise sources impact velocity-monitoring results, and will require investigation in future studies. Our results indicate that this effect should be considered as a potentially significant source for errors. If repeating waves were to dominate regular velocity monitoring results, the spatial sensitivity of detected velocity changes and the implicit assumptions about dominant wave types would need to be reconsidered (e.g. Obermann et al. (2013, 2016)). For example, our results show that body waves can be detected reliably far into the coda during the summer months (Figs 4.4, 4.7).

Our results further have significant implications for the understanding of higherorder correlations of ocean microseisms, as well as any other persistent isolated noise sources. Higher-order correlations have been proposed as an additional processing step to achieve correlation wavefields that resemble the Green's function of the medium more accurately (Stehly et al., 2008; Zhang et al., 2020). They are computed by first computing correlation functions of two stations with a common master station, sometimes called auxiliary station in this context, and then re-correlating the correlating functions. When computing the correlation of the coda of the correlation wavefield (C³), the resulting higher-order correlation wavefield will be an accurate representation of the Green's function under the assumption that the coda of the original correlation wavefield is fully scattered (Stehly et al., 2008). We, however, find repeating waves from persistent isolated noise sources to be present and coherent throughout the coda windows (Figs 4.2 - 4.5). Correlations of the direct arrivals in the correlation wavefield (C^2), induced by an isolated noise source have been previously shown to be insensitive to the master station because the phase information recorded at the master station cancels out (Sheng et al., 2018). This is precisely same argument we use for the irrelevance of the master station in the beamforming of correlation wavefields when only an isolated noise source is present (Equation 4.6).

In other words, beamforming correlation wavefields directly probes higher-

order correlations, because beamforming involves the cross-correlation of the investigated signals (Baggeroer et al., 1988; Ruigrok et al., 2017). Thus, our results for the direct arrival windows are probing the C² wavefield and find direct waves to dominate as expected. The results for all coda windows, however, are probing the C³ wavefield and find repeating waves to dominate (Figs 4.2) - 4.5). We do not detect direct arrivals to be dominant in these windows, which would likely emerge if this part of the correlation wavefield was fully scattered (Stehly et al., 2008). The test with a random time series as the master station recording (Figure 4.5) and the fact that the master station contributes no phase information to the beamformer (Equation 4.6) demonstrate why we detect the repeating waves from isolated sources instead. It also follows that persistent isolated noise sources are enhanced in higher-order correlation wavefields, scaling linearly with the number of master or auxiliary stations (Equation 4.6). Therefore, our results suggest that higher-order correlation wavefields do not necessarily achieve more favourable wavefield conditions and thus better Green's function estimates. They achieve the opposite when persistent isolated noise sources are present, and we show in this study that ocean microseisms act in this way.

4.7 Conclusion

This study revisits the impact of noise sources on the coda of correlation wavefields. We present evidence that changing microseism sources directly affect the coda composition. Surface waves propagating from microseism sources in the Northern Atlantic dominate during boreal winter, whereas body waves generated in the Southern oceans dominate during boreal summer. Therefore, the coda does not consist exclusively of scattered waves. It follows that velocity monitoring strategies exploiting scattered waves in the coda of correlation wavefields may need to be adapted to take this effect into account. It further follows that higher-order correlations enhance the bias of non-homogeneous source distributions instead of reducing it.

Acknowledgment

The authors gratefully acknowledge Christoph Sens-Schönfelder for discussions about the role of the master station. The authors acknowledge funding provided by the European Union's Horizon 2020 research and innovation programme under the Marie Skłodowska-Curie grant agreement No. 955515 (SPIN-ITN, https://spin-itn.eu). We gratefully thank the operators of the European permanent and temporary seismic networks who make their data available through EIDA (http://www.orfeus-eu.org/eida). All data processing is carried out with Python software, utilizing the community software ObsPy (Krischer et al., 2015) and Seismic Analysis Code (SAC) (Goldstein and Snoke, 2005) for data processing and analysis.

Data availability

We analysed seismic broad-band stations (vertical component) within latitudes 30°N-65°N and longitudes 15°W-30°E, for two years of data (2019 & 2021), and for which data are distributed by the ORFEUS service European Integrated Data Archive, EIDA (Strollo et al., 2021). Waveform data used in this paper belong to the permanent networks with codes: GR (Federal Institute for Geosciences and Natural Resources (BGR), Germany, 1976), IV (Istituto Nazionale di Geofisica e Vulcanologia (INGV), Italy, 2005), FR (Reseau sismologique et géodésique français (RESIF), France, 1995), FN (Sodankylä Geophysical Observatory / University Of Oulu, Finland, 1980), PL (Polish Academy of Sciences, Polskiej Akademii Nauk (PAN), Poland 1990), PM (Instituto Português do Mar e da Atmosfera, I.P. (IPMA), Portugal, 2006).

Chapter 5

Seasonal variations in Rayleigh and Love waves: A comparison of Pacific and Atlantic oceans

The present chapter is intended to address the third research questions posed in the introduction of this thesis:

 What are the locations of microseismic sources during summer and winter and how can microseism noise be decomposed into distinct wavefield components, such as Rayleigh and Love waves?

5.1 Seasonality of microseisms in southern California from 6C ground motions

Le Tang¹, Heiner Igel¹, Jean-Paul Montagner², Celine Hadziioannou³, Mahsa Safarkhani³, Frank Vernon⁴

Department of Earth and Environmental Sciences, Ludwig-Maximilians-Universität München, 80333, Munich, Germany

 2 Institut de Physique du Globe de Paris, Université de Paris, 75238, Paris, France

³ Institute of Geophysics, University of Hamburg, 20146, Hamburg, Germany ⁴ Institute of Geophysics and Planetary Physics, University of California San Diego, La Jolla, CA, USA

Author Contribution of Mahsa Safarkhani: Methodology, Formal Analysis, Investigation , Data Curation, Writing - Review and Editing , Visualization

This study demonstrates that six-component (6C) observations, combining translational and rotational motions, can effectively capture the seasonal variations in microseismic sources. Using rotational motions extracted from a small seismic array at the Pinon Flat Observatory (PFO), this study analyzes the primary (10–20 s) and secondary (5–10 s) microseisms.

The full version of this paper is provided in the supplementary materials of this thesis (See Supp. A2).

5.2 A comparison of Pacific and Atlantic oceans

5.2.1 Introduction

Ambient noise correlations have transformed microseismic noise into a valuable signal source for seismic monitoring and imaging techniques. A deeper understanding of the generation mechanisms and wavefield characteristics of microseismic noise can help understand the ambient noise applications. In particular, accurately determining the spatial and temporal distribution of noise sources is crucial for improving waveform inversion techniques applied to noise correlations. Higher space-time resolution can be achieved by identifying the dominant microseism generation areas and their seasonal variations (i.e., summer vs. winter).

Broadband seismic networks worldwide predominantly use well-established methods such as three-component beamforming to localize primary and secondary microseisms and analyze their wave types (Rayleigh and Love waves). Additionally, small-aperture seismic arrays allow for a more detailed investigation of ambient seismic noise wavefields (see Section 3.2). While microseism sources have been extensively characterized in previous studies, the motivation behind this research lies in assessing their seasonal variations and spatial distribution specifically in terms of Rayleigh and Love waves in both primary and secondary microseisms utilizing two distinct methods.

The third research question of this study examines microseism characterization in terms of source locations and seasonal behavior. To address this question, we evaluate the accuracy and applicability of the array-derived rotation results with three-component beamforming in detecting microseismic wave types and their back azimuths. By evaluating their results, this study aims to assess the reliability and limitations of each approach. A key motivation for this comparison is the potential to reduce dependence on rotational motion sensors, which, despite their advantages, remain costly and sparsely deployed worldwide for large-scale microseism studies. The following sections will present and

compare array-derived rotation and three-component beamforming results for the two study regions (the United States and Europe).

This chapter characterizes microseismic noise and its generation mechanisms within the primary (0.05–0.1 Hz) and secondary (0.1–0.2 Hz) frequency bands. Three-component beamforming (see Section 2.3.1) is employed to differentiate between Love and Rayleigh waves in microseismic noise fields recorded by arrays in Europe and the United States. Subsequently, the array-derived rotation method (see Section 2.3.2) is applied to evaluate the feasibility of using rotational seismology for estimating the back azimuths of Rayleigh and Love waves in both frequency bands and to examine their seasonal variations.

A systematic comparison of these two methods was conducted over the same processing period (2016–2020) for seismic arrays located in the United States and Europe, with a focus on the Pacific and Atlantic Oceans (see Sections 3.2 & 3.3).

5.2.2 Method

Both three-component beamforming and array-derived rotation methods are applied to raw seismic data recorded by three-component stations, as described in Chapter 2. Data pre-processing is performed using ObsPy (Beyreuther et al., 2010; Krischer et al., 2015), ensuring consistency in data handling for both methods to allow a direct comparison of the results.

The pre-processing workflow begins with removing the mean (demeaning) and trend (detrending) from the daily recorded waveforms at each station. A bandpass filter with corner frequencies of 0.01–0.6 Hz is applied to focus on the frequency content of primary and secondary microseisms. The signals are then decimated to 2 Hz while maintaining the Nyquist theorem conditions. Instrument response correction is performed using corner frequencies of 0.01, 0.02, 0.5, and 0.6 Hz to remove instrumental noise. In the final step, a second bandpass filter is applied to focus on the relevant frequency bands: 0.05–0.1 Hz for primary microseisms and 0.1–0.2 Hz for secondary microseism analysis.

In the three-component beamforming method, beamforming is applied using a 600 second sliding window to perform a grid search for slowness with a 0.02 s/km increment and a 2° degree spacing in back azimuth.

In the array-derived rotation method, rotational motions are first retrieved using the array_rotation_strain function in ObsPy (Krischer et al., 2015). The function calculates three-component rotational motions and 6 components of strain values for giving the translational seismic array using the finite-differencing approach (see Section 2.4.1, (Spudich et al., 1995)). In the next step, these retrieved rotational measurements are compared to the second-order derivative of the recorded signals (i.e., acceleration) according to Equation 2.20 for Love wave polarization and Equation 2.22 for Rayleigh wave polarization (See Section 2.4.2).

To determine the back azimuth, the rotation signals are rotated in the predefined theoretical back azimuth within the 0–360° range with 2° degree increments and analyzed for their similarity to the acceleration signal at each specific back azimuth (see Section 2.4.2). The degree of similarity between these signals is then determined using a 600-second sliding window, where the correlation coefficient between the rotation and acceleration signals is calculated for each time window. The maximum correlation coefficient is interpreted as the most probable direction of the microseism sources.

5.2.3 Results

5.2.3.1 Array-derived rotation (United States)

Before applying the array-derived rotation and three-component beamforming methods to ambient seismic noise, we first examine their performance on a major earthquake recorded by the Pinon Flat (PFO) and ARCES arrays (Tanimoto et al. (2016b); Donner et al. (2017); Tang et al. (2024a)). Figure 5.1 shows the location of an earthquake that occurred in Noto Peninsula, Japan on January 1, 2024, with a magnitude M7.5 (see figure 5.1a & c).

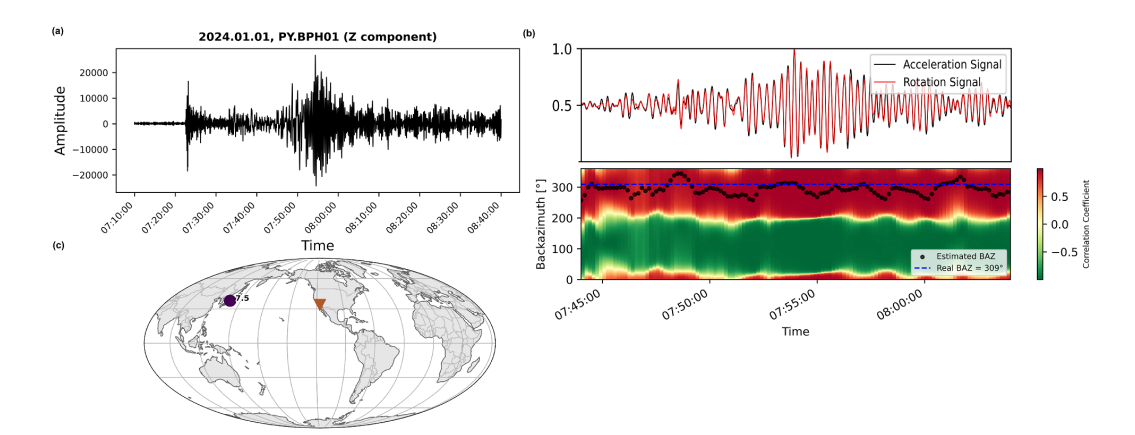


Figure 5.1: (a) The 30-minute earthquake signal from January 1, 2024, in Japan with a magnitude of M7.5 is displayed.(c) Purple dot shows the location of the earthquake relative to the center of the Piñon Flat array in California (yellow triangle).(b) The results of the rotational beamforming for Rayleigh waves polarization are shown. This is done by calculating the correlation coefficient of the vertical acceleration with the horizontal rotation signals. The black dots in the figures represent the maximum values obtained in each sliding window, while the dashed line indicates the actual back azimuth of the earthquake (309.6°).

Since our focus is on Rayleigh and Love wave polarization, array-derived rotation beamforming method is applied to time windows centered on surface wave arrivals (Figure 5.1 b), which can be visually identified and estimated using a ray model.

As illustrated in Figure 5.1b, which focuses on Rayleigh wave polarization, the horizontal rotational signal is represented in red, while the vertical acceleration signal is depicted in black. The strong agreement between these signals is evident.

Given the total length of the time series, which is 20 minutes, a 60-second sliding window with 10% overlapping across the entire time series is applied, and the correlation coefficient between the two signals is computed. The black dots present the retrieved maximum correlation coefficient for each sliding window, while the dashed line displays the real back azimuth corresponding to the earthquake location relative to the Pinon flat array. As demonstrated, the estimated back azimuth aligns with the actual back azimuth (309.6°).

After validating the method using a known source location, we apply it to

ambient seismic noise records (Hadziioannou et al., 2012; Tang et al., 2024a) for the time period 2016–2020. Figure 5.2 presents the results for Rayleigh wave polarization in the primary microseism frequency band (0.05–0.1 Hz, 10-20 sec). The color map depicts the correlation coefficient retrieved for each sliding window, computed over the entire grid search of back azimuths (0°–360°).

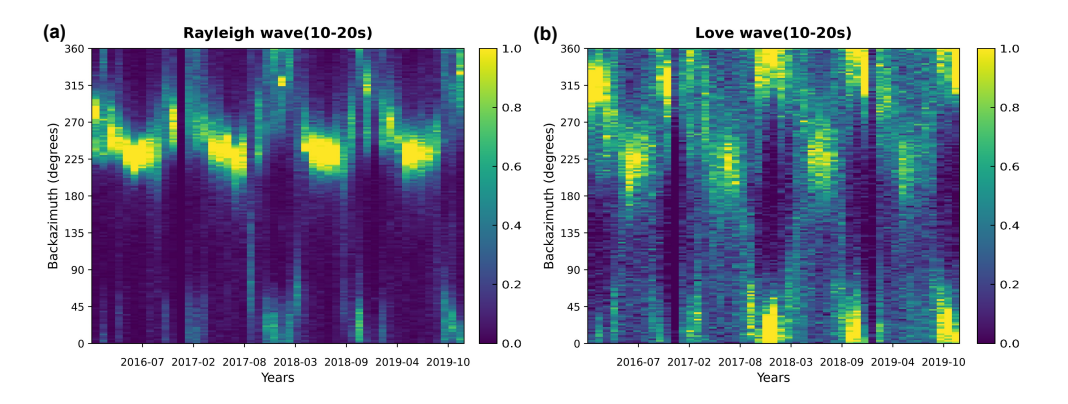


Figure 5.2: The rotational beamforming results for Pinon Flat in the primary microseismic frequency band (0.05–0.1 Hz, 10–20 s) for Rayleigh (a) and Love (b) wave types. The color map illustrates the distribution density of the computed correlation coefficient over backazimuth for a duration of four years (2016.01-0.1–2019.12.01).

As illustrated in Figure 5.2a, for Rayleigh waves, the distribution of maximum correlation coefficients with the highest density is concentrated within the 200°–270° range. This maximum range is consistently observed each year during boreal summer. During boreal winter, the back azimuth oscillates between 0°–45° and 315°–360°. Analyzing the entire four-year period, we observe that the maximum correlation values are generally higher in summer compared to winter.

As illustrated in Figure 5.2b, the density distribution of the retrieved correlation coefficients for Love wave primary microseism is depicted. During boreal summer, the back azimuth range is between 180° and 225° degrees. During winter, the source directions predominantly range between 0°–45° and 300°–360°, with a generally stronger distribution compared to summer. The seasonal variation is particularly pronounced in the primary microseisms for both Rayleigh and Love waves.

Figure 5.3 presents the results for Rayleigh and Love waves in the secondary

frequency band (0.1–0.2 Hz, 5–10 s). The spatial distribution of high correlation values exhibits slight variations between summer and winter. For Rayleigh waves, the primary range remains $200^{\circ}-250^{\circ}$, with relatively stable intensity during summer ($200^{\circ}-225^{\circ}$) and winter ($230^{\circ}-250^{\circ}$). In contrast, Love waves display a broader range ($190^{\circ}-270^{\circ}$) and exhibit higher intensity during summer compared to winter.

A comparison of the results across both frequency bands reveals that the secondary frequency band exhibits a higher density of distribution values, suggesting a more compact distribution of sources in comparison to primary microseisms.

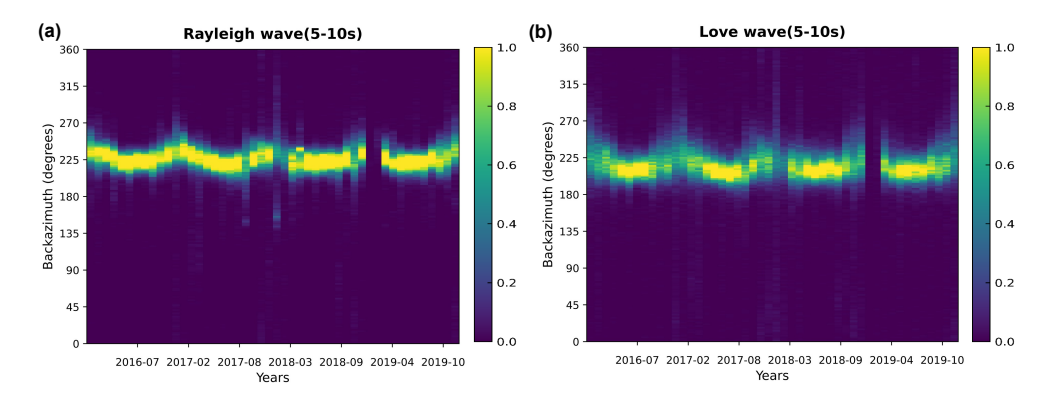


Figure 5.3: The rotational beamforming results for Piñon Flat in the secondary microseismic frequency band (0.1–0.2 Hz, 5–10 s) for Rayleigh (a) and Love (b) wave types. The color map illustrates the distribution density of the computed correlation coefficient over backazimuth for a duration of four years (2016–2020).

5.2.3.2 Three-component beamforming (United States)

In this section, we present the results of three-component beamforming applied to the AZ and CI arrays in California. Unlike array-derived rotation, beamforming employs a grid search over slowness during the computation of beam values. To provide a comprehensive overview, we display the average beam values retrieved across the full back azimuth range $(0^{\circ}-360^{\circ})$ and slowness values (0-0.5 s/km).

Figure 5.4 illustrates the beamforming results for Rayleigh and Love waves in the primary (0.05–0.1 Hz) and secondary (0.1-0.2 Hz) frequency bands.

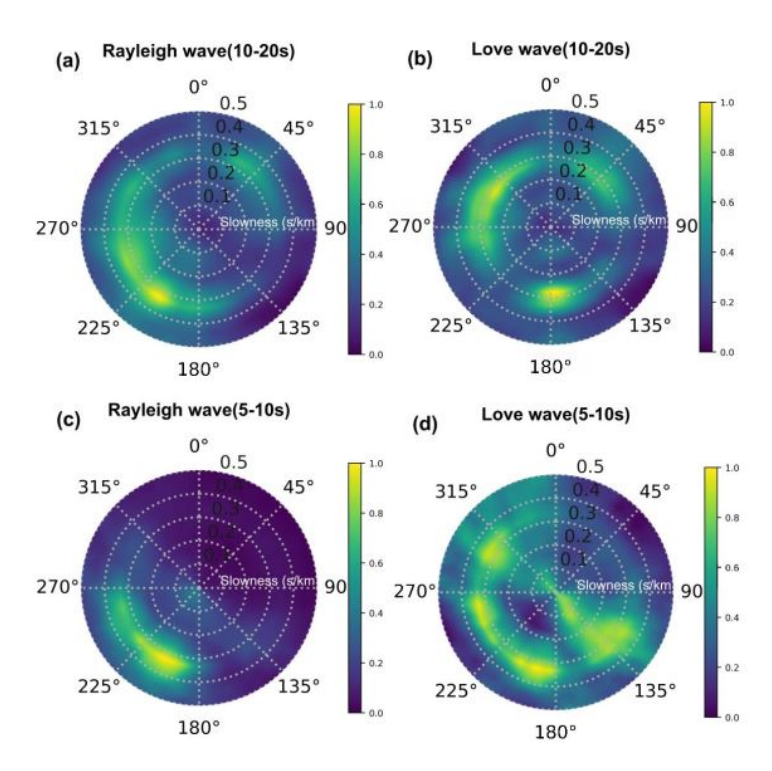


Figure 5.4: The results of three-component beamforming for a combination of stations of AZ and CI arrays in California, specifically the Rayleigh wave (a) and the Love wave (b) for the primary frequency band (0.05-0.1 Hz, 10-20 sec), and the Rayleigh wave (c) and the Love wave (d) for the secondary frequency band (0.1-0.2 Hz, 5-10 sec). The color map illustrates the mean of the estimated beam values for a 600-second sliding window over a period of four years (2016.01.01-2019.12.01) for a back azimuth versus slowness (0-0.5 s/km) grid search.

Regarding the primary microseism (see figure 5.4a and b, the dominant source directions for these wave types differ significantly, with Rayleigh waves primarily originate from approximately 225° with a slowness of surface waves. Love waves are predominantly observed at two locations focusing on 180° and 315° with a slowness of surface waves.

To assess seasonal variations, Figure 5.5 presents the average beam values for summer and winter months in the primary frequency band. The impact of seasonal variation is particularly pronounced in the three-component beamforming results, highlighting distinct shifts in source direction and wave propagation characteristics. During summer, Rayleigh waves exhibit a local maximum at $200^{\circ}-225^{\circ}$ with a slowness in the range of 0.3 s/km, whereas in winter, the dominant direction shifts to $300^{\circ}-320^{\circ}$, maintaining the same slowness. Additional, lower-amplitude sources are widely distributed within the $180^{\circ}-300^{\circ}$ and $0^{\circ}-50^{\circ}$

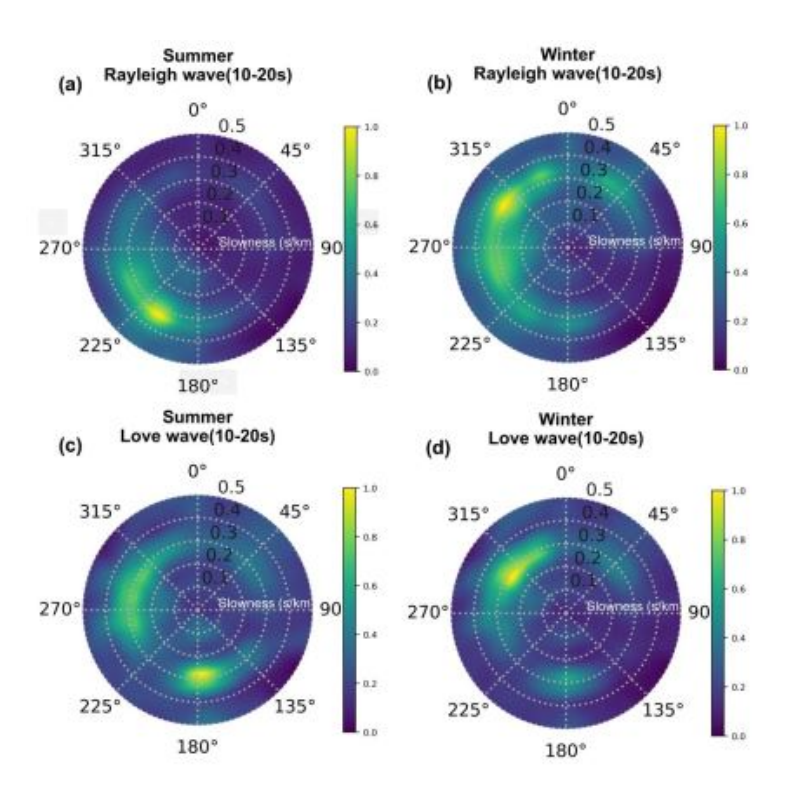


Figure 5.5: The results of three-component beamforming for a combination of stations of AZ and CI arrays in California, specifically the Rayleigh wave (a) and (b), the Love wave (c) and (d) for the primary frequency band (0.05-0.1 Hz, 10-20 sec). The color map illustrates the mean of the estimated beam values for a 600-second sliding window over a period of four years (2016-2020) for boreal summer (April-December) and boreal winter (December-March) for a back azimuth versus slowness (0-0.5 s/km) grid search.

back azimuth ranges.

For Love waves, seasonal variations are also evident, with a shift in dominant back azimuth from 150°–190° (summer) to 290°–340° (winter), while maintaining a consistent slowness range of surface waves.

Figure 5.6 presents the average beam values for summer and winter in the secondary frequency band (0.1–0.2 Hz). Rayleigh waves exhibit a consistent source direction across both seasons, with a back azimuth range of 190°–230° and a slowness of surface waves.

For Love waves, the energy distribution is more dispersed across multiple back azimuth and slowness combinations. However, the majority of the energy remains concentrated within the 230°–270° and 290°–330° back azimuth ranges.

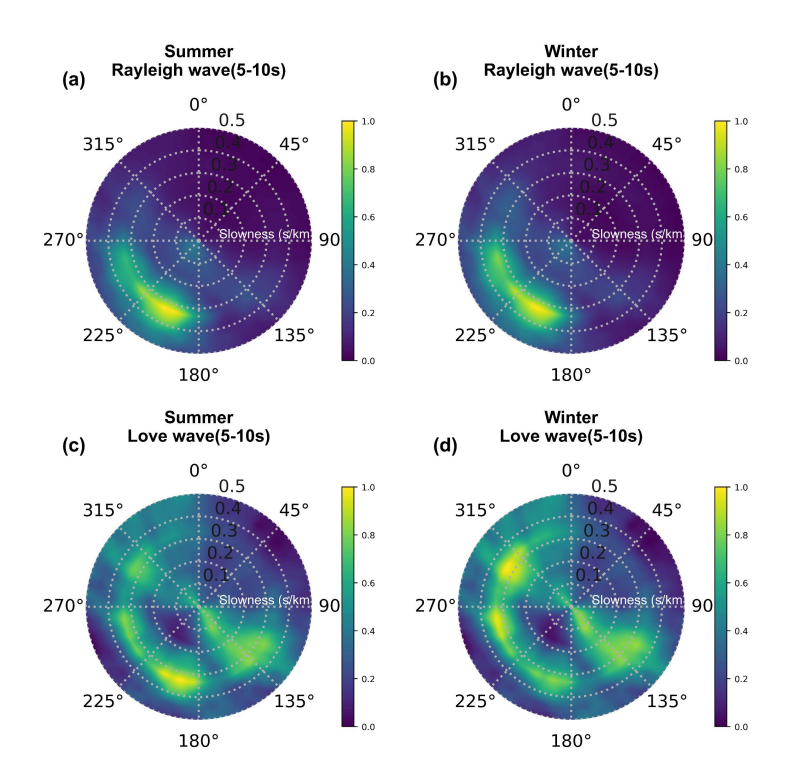


Figure 5.6: The results of three-component beamforming for a combination of stations of AZ and CI arrays in California, specifically the Rayleigh wave (a) and (b), the Love wave (c) and (d) for the secondary frequency band (0.1-0.2 Hz, 5-10 sec). The color map illustrates the mean of the estimated beam values for a 600-second sliding window over a period of four years (2016-2020) for boreal summer (April-December) and boreal winter (December-March) for a back azimuth versus slowness (0-0.5 s/km) grid search.

Additionally, a distinct secondary source direction appears at 110° - 140° , with a slowness ranging from 0 to 0.5 s/km, which is not observed in the rotation-derived results (Figure 5.12).

5.2.3.3 Array-derived rotation (Europe)

In a similar manner with Figure 5.1, Figure 5.7 illustrates the implementation of the array-derived rotation method for the specified earthquake, as documented by the ARCES array (see figure 5.7a and c). In congruence with Figure 5.1, the retrieved back azimuth demonstrates a strong correlation with the actual back azimuth of the earthquake in relation to the ARCES array 56.4°.

Using the same validation approach as for known source locations (e.g., earth-quakes), Figure 5.8 illustrates the results derived from four years of continuous

data in the primary frequency band (10–20 s).

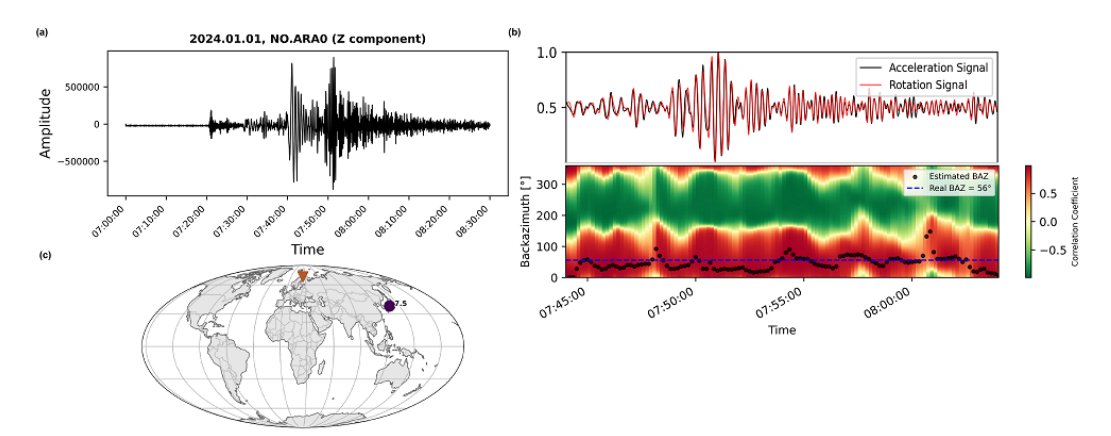


Figure 5.7: (a) The 30-minute earthquake signal from January 1, 2024, in Japan with a magnitude of M7.5 is displayed.(c) Purple dot shows location of the earthquake relative the center of the ARCES array in Norway.(b) The results of the rotational beamforming for Rayleigh waves polarization are shown. This is done by calculating the correlation coefficient of the vertical acceleration with the horizontal rotation signals. The black dots in the figures represent the maximum values obtained in each sliding window, while the dashed line indicates the actual back azimuth of the earthquake (56.4°) .

This figure demonstrates a consistent directional pattern for both Rayleigh and Love wave microseisms. Rayleigh waves exhibit a narrower back azimuth range, concentrated between 280° and 310°, whereas Love waves are distributed over a broader back azimuth range of 180°–315°. Both wave types show clear back azimuth detections during the winter months of each year, while no distinct directional patterns are observed during the summer.

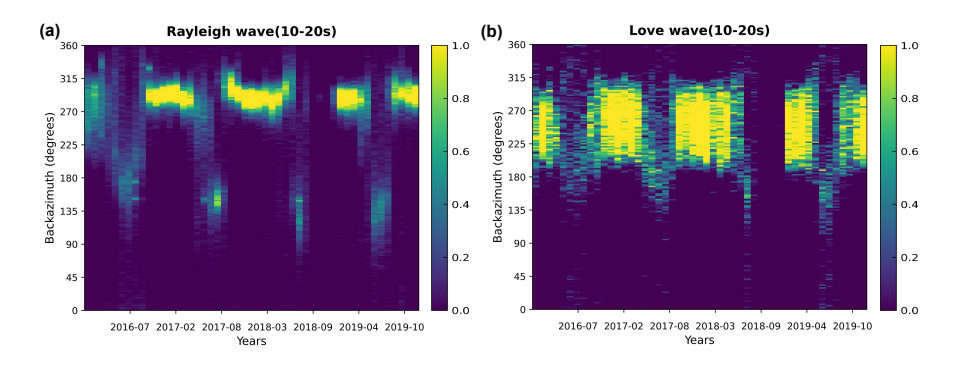


Figure 5.8: The rotational beamforming results for ARCES array in the primary microseismic frequency band (0.05–0.1 Hz, 10–20 s) for Rayleigh (a) and Love (b) wave types. The color map illustrates the distribution density of the computed correlation coefficient over backazimuth for a duration of four years (2016.01.01–2019.12.01).

In the secondary frequency band (see figure 5.9), the results exhibit a pattern

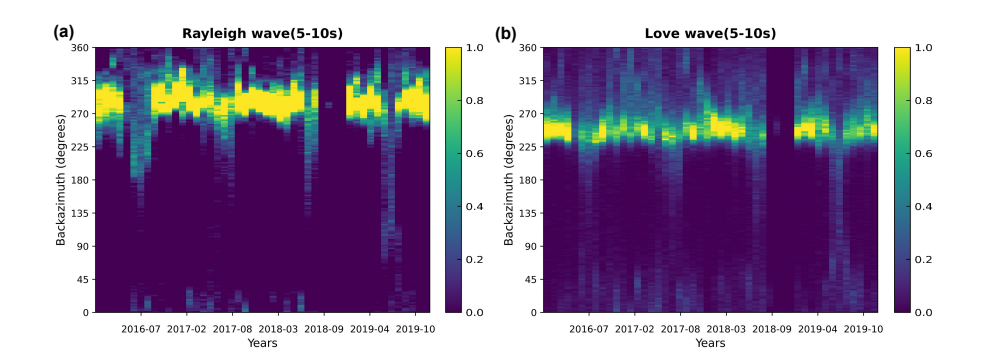


Figure 5.9: The rotational beamforming results for ARCES array in the secondary microseismic frequency band (0.1–0.2 Hz, 5–10 s) for Rayleigh (a) and Love (b) wave types. The color map illustrates the distribution density of the computed correlation coefficient over backazimuth for a duration of four years (2016.01.01–2019.12.01).

similar to the primary microseisms. Rayleigh wave polarization remains stable with back azimuths ranging from 270° to 315°, while Love waves show stability within the 225° to 270° range. A similar scenario is observed during the summer months, where no distinct directional pattern is detectable.

5.2.3.4 Three-component beamfomring (Europe)

In this section, we present the results of three-component beamforming applied to the NOA array in Norway. The results of distribution of beam values for four year time span (2016-220) in slowness grid 0-0.5 s/km and back azimuth ranging 0-360° degree shows in Figure 5.10.

The primary sources contributing to both microseisms originate predominantly from the west and north-northwest of the array. Rayleigh waves in the primary microseism band are primarily concentrated in the 240°–310° range, with a lower amplitude distribution extending from 310° to 10°. In contrast, secondary Rayleigh microseisms exhibit well-focused directions between 265°–290° and 335°–350°.

For Love waves, the primary microseisms are predominantly influenced by sources in the 340°–14° range, while secondary microseisms display multiple contributing directions, notably from 260°–290° and 334°–20°. This pattern aligns with observations from other oceanic regions in figure 5.10a-c.

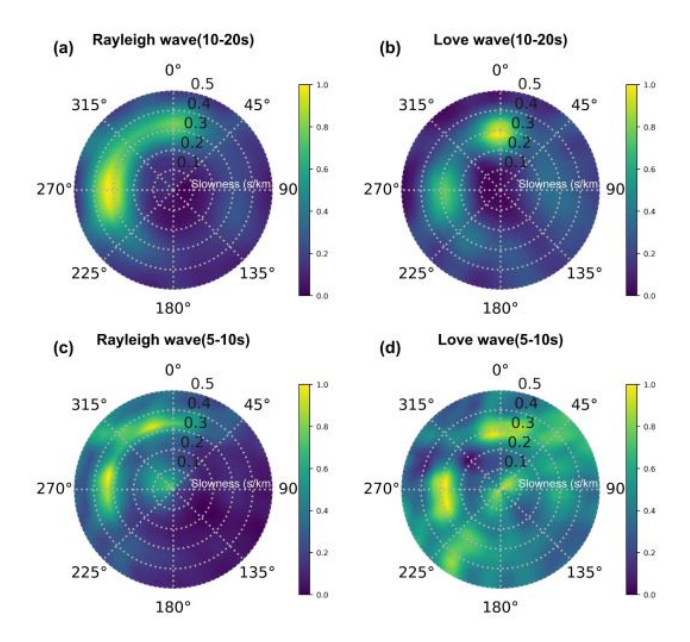


Figure 5.10: The results of three-component beamforming for a combination of stations of NOA arrays in Norway, specifically the Rayleigh wave (a) and (b), the Love wave (c) and (d) for the secondary frequency band (0.1-0.2 Hz, 5-10 sec). The color map illustrates the mean of the estimated beam values for a 600-second sliding window over a period of four years (2016-2020) for boreal summer (April-December) and boreal winter (December-March) for a back azimuth versus slowness (0-0.5 s/km) grid search

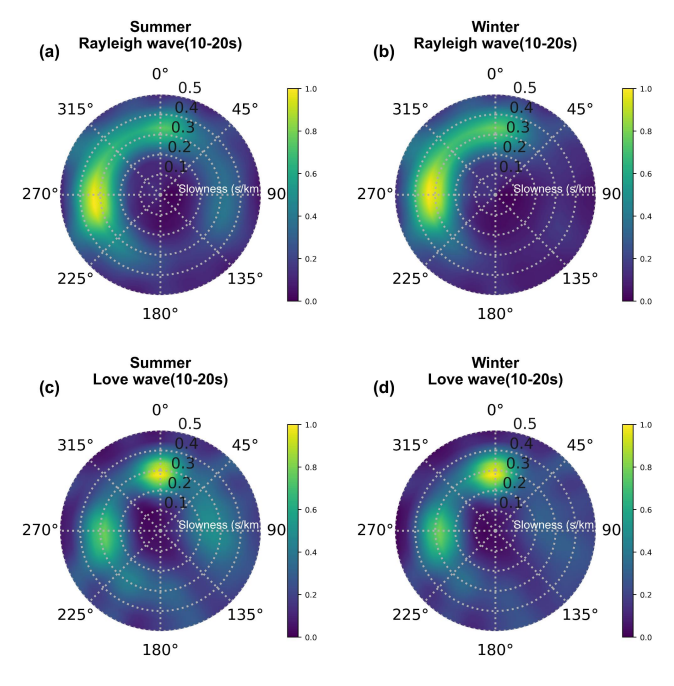


Figure 5.11: The results of three-component beamforming for a combination of stations of NOA arrays in Norway, specifically the Rayleigh wave (a) and (b), the Love wave (c) and (d) for the primary frequency band (0.05-0.1~Hz, 10-20~sec). The color map illustrates the mean of the estimated beam values for a 600-second sliding window over a period of four years (2016-2020) for boreal summer (April-December) and boreal winter (December-March) for a back azimuth versus slowness (0-0.5~s/km) grid search.

The seasonal variation in primary microseisms is illustrated in Figure 5.11. As observed, the source directions remain remarkably stable for both wave types throughout the year. Rayleigh waves are consistently detected within the 230°–290° range, while Love waves are predominantly observed between 350°–30° during both summer and winter.

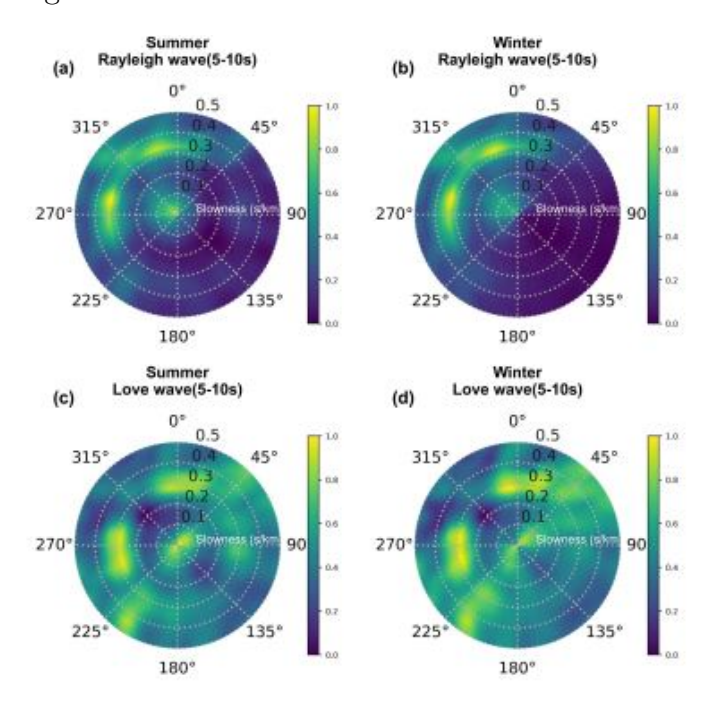


Figure 5.12: The results of three-component beamforming for a combination of stations of NOA arrays in Norway, specifically the Rayleigh wave (a) and (b), the Love wave (c) and (d) for the secondary frequency band (0.1-0.2 Hz, 5-10 sec). The color map illustrates the mean of the estimated beam values for a 600-second sliding window over a period of four years (2016-2020) for boreal summer (April-December) and boreal winter (December-March) for a back azimuth versus slowness (0-0.5 s/km) grid search.

Examining the secondary microseisms during boreal summer and winter in Figure 5.12, we observe stable source directions, consistent with the patterns identified in Figure 5.10 for secondary frequency band (5-10 s).

5.2.4 Discussion

To facilitate an easier overview of the results obtained using the array-derived rotation and three-component beamforming methods, we have organized the polarization results for Rayleigh and Love waves into primary and secondary microseisms for breal summer (yellow shadow) and breal winter (purple shadow).

As illustrated in Figure 5.13, the dominant source directions for both primary and secondary microseisms are generally consistent across the two methods. For instance, using both approaches, the main sources for secondary microseisms are located to the southwest of the California array, with back azimuths ranging from 200° to 260° toward the coast. This stable pattern over the years is in agreement with previous studies (Tanimoto et al., 2006; Stehly et al., 2006).

In contrast, primary microseisms exhibit considerable seasonal variations. During winter, source activities are more prominent in the north-northwest direction, likely a result of storms originating in the Northeast Pacific that occur closer to the Pacific coast. This suggests that primary microseisms, which are excited by the interaction of oceanic swells and the seafloor (Ardhuin et al., 2011), are closely linked to seasonal variations in global ocean wave activity (Stehly et al., 2006; Colosi et al., 2021; Tang et al., 2024a). Also, this suggests that storm swells arrive at different coastal areas during different seasons.

The array-derived rotation method produces similar results for both Love and Rayleigh polarizations, whereas the three-component beamforming method reveals a broader back azimuth distribution for Love waves. This discrepancy may indicate that array-derived rotation is less sensitive to small scale variations and primarily captures large scale generation mechanisms, while three-component beamforming resolves more detailed directional variations when several source areas acting simultaneously. Although the generation mechanism of secondary Love waves remains controversial, it is generally accepted that unlike Rayleigh waves, which are mainly produced by seafloor pressure fluctuations induced by opposing ocean waves, Love waves could be more strongly influenced by heterogeneous (Rind and Down (1979), Gualtieri et. al., 2020), subsurface structures, and specific bathymetric features (Juretzek and Hadziioannou, 2017). In addition to a dominant pattern of Love wave generation by strong storm patterns from the west-northwest in winter and southwest in summer, other lower energy directions may be attributed to bathymetric effects in the source region, resulting in a weaker and more diffuse Love wavefield.

Figure 5.14 shows that both methods yield very consistent and stable estimates

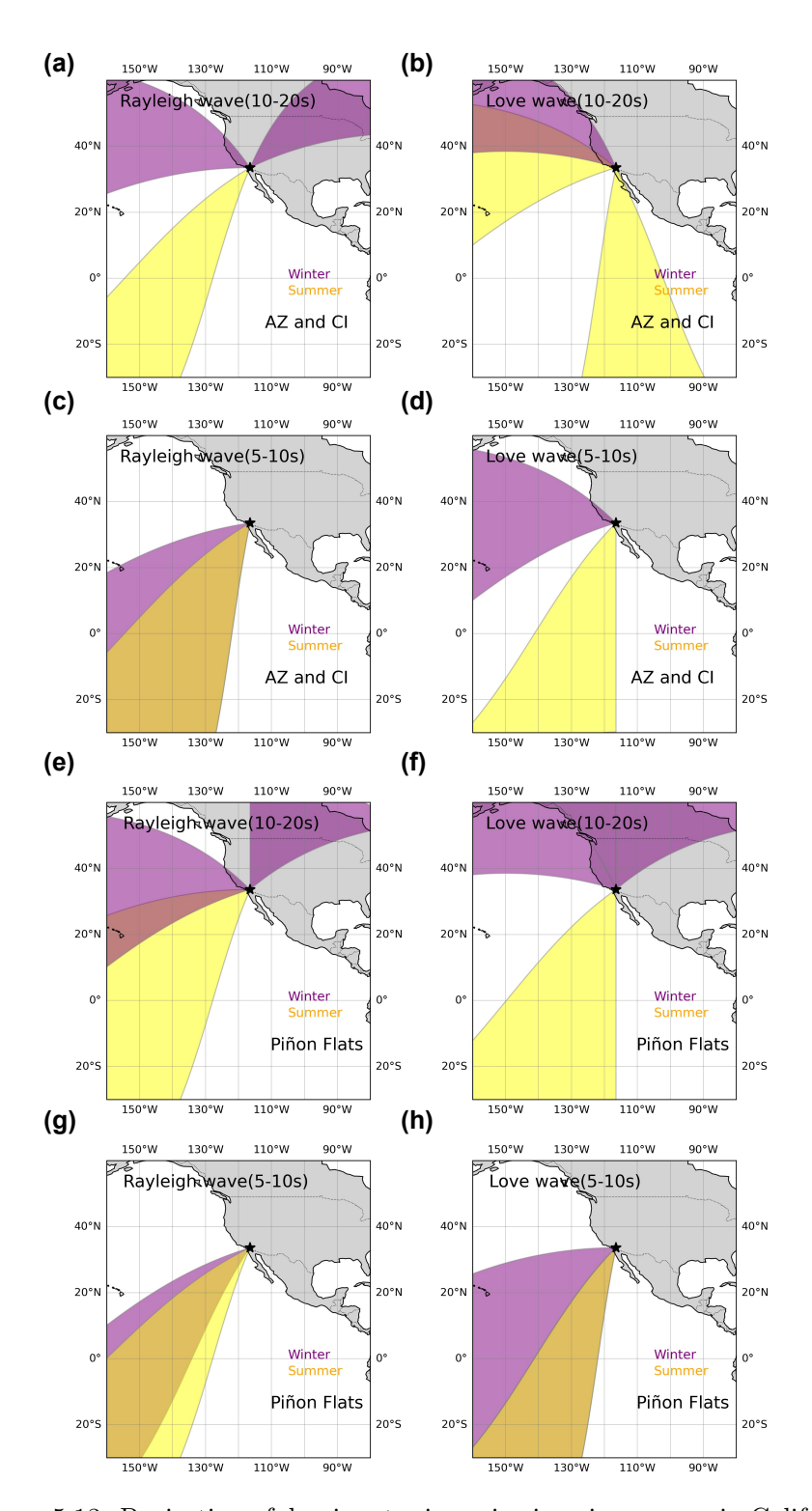


Figure 5.13: Projection of dominant microseismic noise sources in California arrays. (a) Noise sources estimated for AZ and CI stations in the primary microseism band (10–20 s), focusing on Rayleigh waves. (b) Same as (a) but for Love waves. (c) Noise sources in the secondary microseism band (5–10 s) for Rayleigh waves. (d) Same as (c) but for Love waves estimations were performed using three-component beamforming. This results shows in the same order for Pinon Flat using array-derived rotation method in (e-h) Yellow shading represents boreal summer, while purple shading represents boreal winter

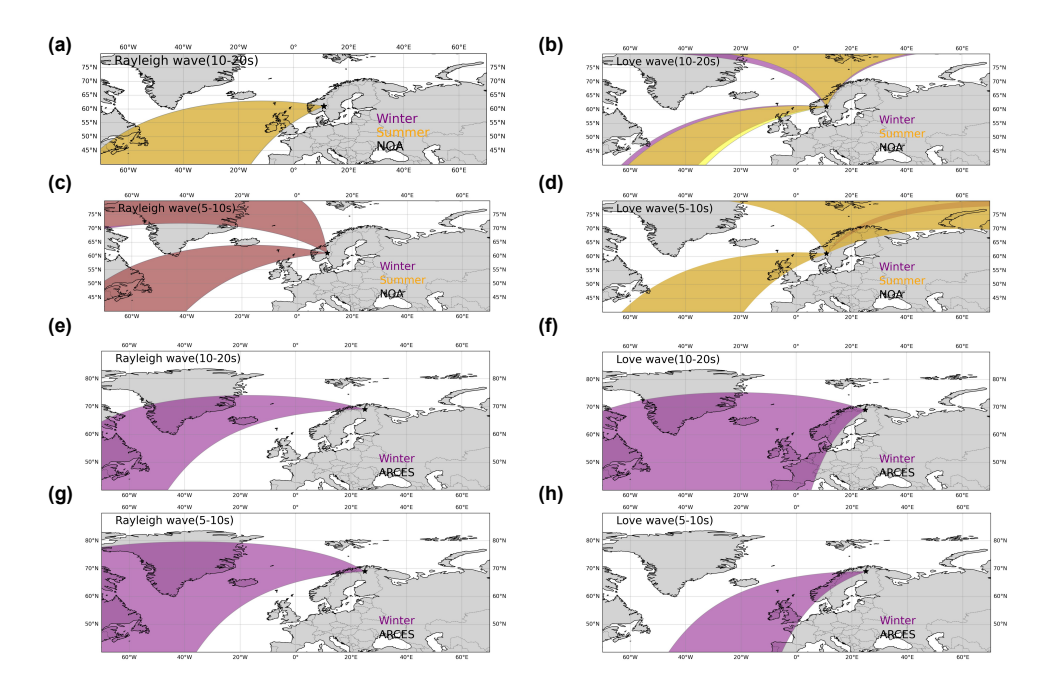


Figure 5.14: Projection of dominant microseismic noise sources in Norway arrays. (a) Noise sources estimated for NOA stations in the primary microseism band (10–20 s), focusing on Rayleigh waves. (b) Same as (a) but for Love waves. (c) Noise sources in the secondary microseism band (5–10 s) for Rayleigh waves. (d) Same as (c) but for Love waves estimations were performed using three-component beamforming. This results shows in the same order for ARCES sismic array using array-derived rotation method in (e-h) Yellow shading represents boreal summer, while purple shading represents boreal winter

of microseismic noise source directions in the primary and secondary frequency bands. In NOA seismic array, three-component beamforming shows less seasonal variation for both microseism types, suggesting the influence of strong, persistent storm activity in the North Atlantic over the years (Essen et al., 2003; Stehly et al., 2006; Stutzmann et al., 2012; Juretzek and Hadziioannou, 2017). Consistent contributions from the west coast of Norway and the northern part of the British Isles are observed in NOA array results for both Rayleigh and primary microseisms (Friedrich et al., 1998; Kimman et al., 2012; Möllhoff & Bean, 2016). However, the northern Norwegian coastal area appears to be more efficient in generating Love waves in the secondary microseism band (Juretzek and Hadziioannou, 2016, 2017). In this frequency band, the stable detection of Rayleigh waves indicates a smaller, more concentrated, and well-defined source mechanism, whereas Love waves exhibit a broader back azimuth distribution. This suggests that Love wave generation is more susceptible to coastline and bathymetric variations, which aligns with the broader energy

distribution observed in secondary microseisms (Retailleau et al., 2021).

Regarding array-derived rotation, the rotations show consistent main directions for both microseismic types during winter, matching the three-component beamforming results. However, during summer, the ADR method displays a spread in the correlation coefficients over the back azimuth search, making it difficult to identify a specific dominant direction. This may be because the array-derived rotation method integrates energy from multiple directions, thereby increasing its sensitivity to scattered or interfering sources, whereas beamforming is better able to isolate coherent wave arrivals.

5.2.5 Conclusion

In this study, we investigated Rayleigh and Love wave polarization in both primary and secondary microseisms using two different methodologies: Array-Derived Rotation and Three-Component Beamforming. For Norway arrays highly stable back azimuth distributions for both Love and Rayleigh waves across all seasons, suggesting persistent and dominant microseismic sources in the North Atlantic. Comparing the results from Norway with those from California, we find that North Atlantic microseismic sources are more stable year-round, while Pacific microseism sources exhibit greater seasonal variability. This difference aligns with studies indicating that persistent storm activity in the North Atlantic contributes to a steady microseismic background, whereas the Pacific experiences more pronounced seasonal storm variations.

Future research should focus on improving the resolution and sensitivity of both array-derived rotation and three-component beamforming techniques to better capture the complexity of Love wave generation. Additionally, incorporating a larger number of stations in array-derived rotation analyses may enhance the method's ability to resolve secondary microseism sources more effectively.

Chapter 6

Summary and Outlook

Microseisms are the most persistent and ubiquitous seismic signals on Earth, generated by the continuous harmonic forcing of ocean waves on the solid Earth. A better understanding of their generation mechanisms and spatial distribution is essential for assessing the accuracy and reliability of ambient noise applications in seismology. This research aimed to address three fundamental questions:

- How do persistent microseismic noise sources shape the coda of correlation wavefields?
- To what extent do seasonal variations influence the stability of the direct and late-arriving components of the correlation wavefield?
- Where are the dominant microseismic sources located during summer and winter, and how can microseismic noise be decomposed into distinct wavefield components, such as Rayleigh and Love waves?

To address the first two questions, we focused on the correlation method and single-component beamforming. This part of the study examined how persistent and seasonal variations in microseisms sources control the correlation wavefields between different station pairs (Chapter 5, Suppl. A1). Our findings challenge the conventional assumption that the coda consists purely of scattered waves, highlighting the substantial influence of noise source distribution on

the correlation wavefield. The results indicate that repeated excitations from oceanic microseisms can persist even in the late coda of the one-hour correlation wavefield. Furthermore, seasonal variations in microseismic activity were observed in the mid, late and end parts of the coda of the correlation wavefield, suggesting that velocity change estimations might be affected by fluctuations in noise sources rather than actual subsurface changes. However, the relative contributions of persistent oceanic sources and scattered coda waves remain an open question and require further investigation.

The third research question shifted the focus to microseismic source localization (Chapter 5, Suppl. A2). Here, we compared the performance of three-component beamforming and array-derived rotation methods. Our goal was to evaluate the effectiveness of array-derived rotation in detecting low-frequency ambient seismic sources and in distinguishing the Rayleigh and Love wave components of primary and secondary microseisms. Investigating two distinct geographical regions—Europe and the United States, allowed us to assess the influence of different oceanic environments, namely the North Atlantic and North Pacific, on microseismic activity. The North Atlantic was found to generate more persistent primary and secondary microseisms, leading to greater stability and less seasonal variability in results obtained from the European arrays. In contrast, the Pacific Ocean exhibited more pronounced seasonal variations, particularly in primary microseisms, as observed in the data from U.S. seismic arrays.

To assess the feasibility of array-derived rotation in microseism studies, we tested two types of seismic arrays with different station numbers, geometries, and locations. Overall, array-derived rotation demonstrated a strong agreement with three-component beamforming results. However, several challenges remain when applying array-derived rotation to microseismic frequency bands. These include limitations related to the sensitivity of array-derived rotation rates to noise levels, the influence of near-surface heterogeneities and topographic effects, and the difficulty of achieving accurate measurements with small-aperture seismic arrays. One of the key constraints is that very few small-size

three-component arrays exist on a global scale. Since the array aperture must be significantly smaller than the microseismic wavelength to avoid spatial aliasing, there is a need for further optimization of array configurations for array-derived rotation applications.

As Large-N deployments become increasingly popular for the detection and localization of microseismic sources, incorporating more small-N arrays could enhance the capabilities of array-derived rotation in monitoring oceanic states through microseisms. Expanding datasets from small-scale deployments would provide a more comprehensive evaluation of the method's robustness and allow for refinements in processing techniques. Additionally, array-derived rotation presents a cost-effective and portable alternative to rare and expensive direct rotational motion sensors.

Acknowledgment

I would like to express my deepest gratitude to my supervisors, Prof. Celine Hadziioannou and Dr. Sven Schippkus, for their invaluable guidance, encouragement, and insightful discussions throughout my PhD journey. I am also sincerely thankful to Prof. Jean-Paul Montagner and Prof. Éléonore Stutzmann for their mentorship, constructive feedback and conversations during my secondment at IPGP. Additionally, I extend my appreciation to SPIN-ITN for funding my doctoral research and providing a collaborative research environment. I am profoundly grateful to my family for their unwavering support of me every step of the way.

This PhD project is funded by the European Union's Horizon 2020 research and innovation program under the Marie Skłodowska-Curie grant agreement No. 955515 (ITN SPIN).

Appendix A

Supplementary material

A.1 Continuous isolated noise sources induce repeating waves in the coda of ambient noise correlations

Sven Schippkus¹, Mahsa Safarkhani¹, Celine Hadziioannou¹

¹Institute of Geophysics, Centre for Earth System Research and Sustainability (CEN), Universität Hamburg, Hamburg, Germany

Corresponding author: sven.schippkus@uni-hamburg.de

Author Contribution: Conceptualization SS, MS, CH; Methodology SS; Software SS; Data curation MS; Formal Analysis SS; Investigation SS, MS; Resources SS, CH; Writing - original draft SS; Writing - Review & Editing SS; Visualization SS; Supervision CH; Funding acquisition SS, CH

Abstract

Continuous excitation of isolated noise sources leads to repeating wave arrivals in cross correlations of ambient seismic noise, including throughout their coda. These waves propagate from the isolated sources. We observe this effect on correlation wavefields computed from two years of field data recorded at the Gräfenberg array in Germany and two master stations in Europe. Beamforming the correlation functions in the secondary microseism frequency band reveals repeating waves incoming from distinct directions to the West, which correspond to well-known dominant microseism source locations in the Northeastern Atlantic Ocean. These emerge in addition to the expected acausal and causal correlation wavefield contributions by boundary sources, which are converging onto and diverging from the master station, respectively. Numerical simulations reproduce this observation. We first model a source repeatedly exciting a wavelet, which helps illustrate the fundamental mechanism behind repeated wave generation. Second, we model continuously acting secondary microseism sources and find good agreement with our observations. Our observations and modelling have potentially significant implications for the understanding of correlation wavefields and monitoring of relative velocity changes in particular. Velocity monitoring commonly assumes that only multiply scattered waves, originating from the master station, are present in the coda of the correlation wavefield. We show that repeating waves propagating from isolated noise sources may dominate instead, including the very late coda. Our results imply that in the presence of continuously acting noise sources, which we show is the case for ordinary recordings of ocean microseisms, velocity monitoring assuming scattered waves may be adversely affected with regard to measurement technique, spatial resolution, as well as temporal resolution. We further demonstrate that the very late coda of correlation functions contains useful signal, contrary to the common sentiment that it is dominated by instrument noise.

Non-technical summary Seismic waves are generated by all kinds of sources, including earthquakes, ocean waves, and machinery. Some sources produce a

consistently present background level of seismic energy, so-called ambient seismic noise. It is well-established that, under the condition of evenly distributed noise sources, cross-correlation of ambient seismic noise, which was recorded on two separate seismic stations, yields a new wavefield that propagates directly from one station to the other. We call this new wavefield the correlation wavefield. Here, we show that in the presence of an additional isolated noise source that excites seismic waves continuously, for example ocean waves induced by storm systems over the Northeastern Atlantic, a new contribution to the correlation wavefield emerges: repeating waves propagating from the isolated noise source. These repeating waves can be more coherent across several stations than the expected correlation wavefield contribution, which propagates from one station to the other. We observe such repeating waves propagating from isolated noise sources on correlation wavefields computed from two years of seismic recordings of the Gräfenberg seismic array in Germany and two master stations in Europe. We reproduce our observations with numerical simulations of the sources and resulting correlation wavefields. Our findings have potentially significant implications for seismic monitoring based on relative velocity changes, which is used to monitor geological faults, volcanoes, groundwater, and other processes in the Earth. Velocity monitoring commonly relies on the assumption that the correlation wavefield contains only the contribution that propagates from one station to the other, which we show is not necessarily correct. This can lead to misinterpretation of measured velocity variations.

A.1.1 Introduction

Seismic interferometry of the ambient seismic field gives rise to new correlation wavefields that relate to the Green's function under the condition of uniformly distributed noise sources (Wapenaar et al., 2005; Gouédard et al., 2008). These correlation wavefields are now routinely used for imaging (e.g., Schippkus et al., 2018; Lu et al., 2018) and monitoring (e.g., Wegler and Sens-Schönfelder, 2007; Hadziioannou et al., 2009; Sheng et al., 2023) of Earth's structure. In the presence of an isolated noise source, a second contribution to this wavefield is

introduced, sometimes referred to as spurious arrival (Snieder et al., 2006; Zeng and Ni, 2010; Retailleau et al., 2017; Schippkus et al., 2022). This correlation wavefield contribution can lead to biased measurements of seismic wave speed due to interference of direct waves from the master station and the isolated noise source (Schippkus et al., 2022).

Monitoring applications, on the other hand, rely on estimating relative velocity changes by repeatedly computing correlation wavefields throughout time and measuring changes in the arrival time of their coda (Wegler and Sens-Schönfelder, 2007; Sens-Schönfelder and Larose, 2010). Current strategies often rely on the assumption that the coda of a given correlation wavefield is comprised of multiply scattered waves, originating from the master station, which also dictates its spatial sensitivity (Planès et al., 2014; Margerin et al., 2016; van Dinther et al., 2021). If the spatial sensitivity of the coda is known, seismic velocity changes can be located (Obermann et al., 2014; Mao et al., 2022). Some progress has been made in accounting for the impact of changes in sources on the correlation wavefield, particularly in the context of monitoring at frequencies above 1 Hz, e.g., by carefully selecting time windows in which the same sources are active and produce similar correlation wavefields (Yates et al., 2022; Sheng et al., 2023).

In this study we demonstrate that isolated noise sources may impact correlation wavefields to a degree previously not considered. Continuously acting isolated noise sources, such as ocean microseisms, produce repeating waves throughout the entire correlation function that propagate from the isolated source location. These waves coincide with and are more coherent than multiply scattered waves originating from the master station. This may have significant impact on the understanding of measured velocity changes. In the following, we show observations of these repeating waves on field data correlation functions in the ocean microseism frequency band using stations throughout Europe, illustrate the mechanism behind repeated direct-wave generation in correlation functions, and finally reproduce our field data observations by modelling continuously acting isolated noise sources, i.e., secondary ocean microseisms.

A.1.2 Beamforming the correlation wavefield

We compute correlation wavefields from two years of continuous vertical component seismograms, recorded in 2019 and 2020 at the Gräfenberg array in Germany and two master stations, IV.BRMO in Italy (Figure A.1a) and PL.OJC in Poland (Figure A.2a). IV.BRMO was chosen randomly and PL.OJC was chosen to showcase a different backazimuth and slightly larger distance to the Gräfenberg array. We apply a standard processing workflow: remove instrument response, cut two years of data into two-hour long segments overlapping by 50%, apply spectral whitening (Bensen et al., 2007), cross-correlate each segment, and stack all segments linearly. No further processing, e.g., earthquake removal or other segment selection, has been applied, because whitening in each segment already normalises the energy potentially introduced by earthquakes and we find no evidence for earthquakes-related bias in the resulting correlation wavefields.

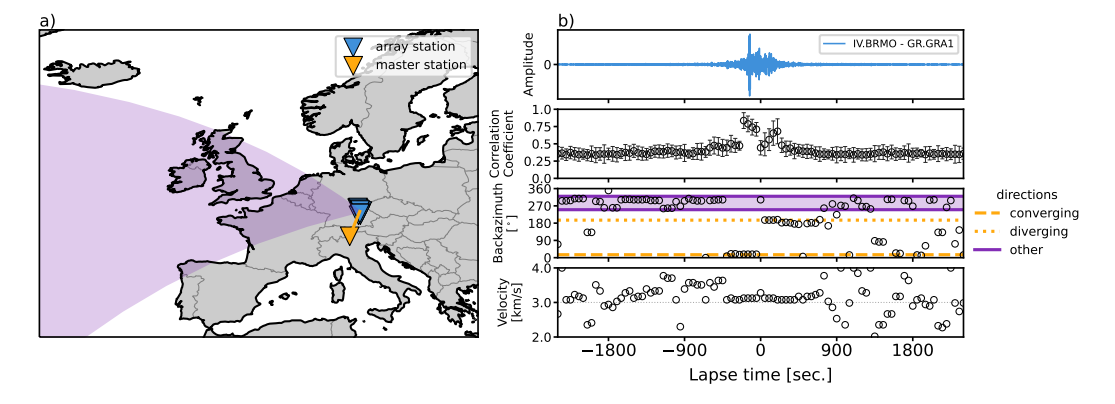


Figure A.1: Beamforming the correlation wavefield between the Gräfenberg array in Germany (blue triangle) and master station IV.BRMO, Italy (yellow triangle), in the secondary microseism frequency band (0.1 to 0.3 Hz). a) Overview map with master station and array stations. The orange line and purple area correspond to the dominant directions detected by beamforming. b) Beamforming results: sample cross-correlation between the master station and one array station (top), mean Pearson correlation-coefficient of correlation functions with best-fitting beams in each window (second panel), detected direction of arrival (third panel), and estimated phase velocity (bottom). Detected directions correspond to the correlation wavefield converging onto and diverging from the master station (orange lines), and a range of directions pointing towards the Atlantic Ocean (purple area).

To estimate from which directions the correlation wavefield arrives at the

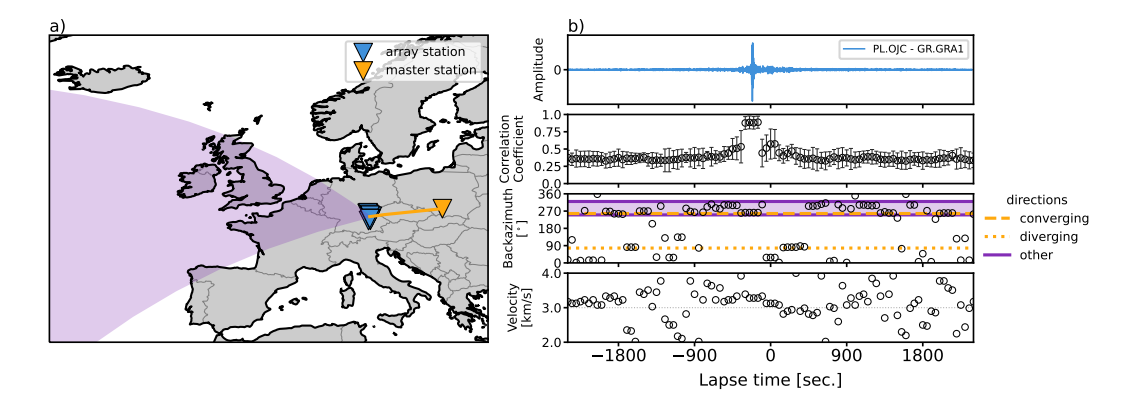


Figure A.2: Same as Figure A.1, but for master station PL.OJC, Poland. The directions detected by beamforming corresponding to the diverging and converging part of the correlation wavefield change with master station as expected (orange lines), whereas the range of directions towards the Northern Atlantic remains constant (purple area). Note that the converging part of the correlation wavefield points towards West, similar to one of the dominant directions detected pointing towards the Atlantic Ocean for master station IV.BRMO (Figure A.1).

Gräfenberg array, we beamform the correlation functions (Figure A.1). We beamform in 200 sec. windows, overlapping by 75%, in the secondary microseism frequency band (0.1 to 0.3 Hz), and assuming plane-wave propagation (Rost and Thomas, 2002). We present a sample correlation function to give orientation in lapse time (Figure A.1b, top panel), and compute Pearson correlation coefficients of all correlation functions with the best-fitting beam for each window to estimate how well the beam explains the data within a window (Figure A.1b, second panel). Similarity is highest for the expected acausal arrival, which also emerges more clearly in the correlation function than the causal arrival, due to the commonly observed strong noise sources in the Northeastern Atlantic (e.g., Friedrich et al., 1998; Chevrot et al., 2007; Juretzek and Hadziioannou, 2016). Throughout the coda, similarity remains nearly constant with a correlation coefficient ~ 0.4 . We detect several dominant directions of arrival (Figure A.1b, third panel). First, the acausal arrival of the correlation wavefield converging onto the master station at negative lapse time (dashed orange line) and the causal arrival diverging from the master station at positive lapse time (dotted orange line), i.e., the correlation wavefield contribution that usually arises in seismic interferometry (Wapenaar et al., 2005). Second, distinct directions throughout the correlation functions pointing

towards West (Figure A.1b, third panel), which we project onto the map view (Figure A.1a).

A second master station in Poland (PL.OJC) illustrates how the converging (acausal) and diverging (causal) parts of the correlation wavefield depend on the geometry of array stations to master station and point roughly towards the great-circle between the two (Soergel et al., 2023), whereas the dominant directions towards West appear to be independent of the master station (Figure A.2). A North-Northeast direction, however, still emerges in the beamforming results as most coherent, which coincides approximately with the great circle direction for the converging part of the correlation wavefield for master station IV.BRMO (Figure A.1). Similarly, the converging direction for master station PL.OJC coincides with the dominant directions towards West (Figure A.2). This hints at the impact the geometry of master station and array stations has on the detection and identification potential of these other directions. We propose the dominant directions detected by beamforming and pointing towards West represent repeating direct waves emerging at isolated noise source locations in the Northeastern Atlantic Ocean. The North-Northeasterly direction observed in the coda in both examples similarly represents waves arriving from isolated source locations off the coast of Norway, which were previously observed as dominant on continuous seismograms (e.g., Juretzek and Hadziioannou, 2016). We call these direct waves, because they propagate directly from the isolated source to the seismic stations. These are not to be confused with the direct waves propagating between the stations, i.e., the expected acausal and causal arrivals.

A.1.3 A repeating impulsive isolated noise source

To substantiate our hypothesis and explain the observations above, we start from the concept of an isolated noise source (Schippkus et al., 2022). Consider a wavefield that is excited by sources on a boundary S and an isolated noise

source at \mathbf{r}_N , recorded on a station at location \mathbf{r}

$$u(\mathbf{r}) = \oint_{S} N_{B}(\mathbf{r}')G(\mathbf{r}, \mathbf{r}')d\mathbf{r}' + N_{I}G(\mathbf{r}, \mathbf{r}_{N}), \qquad (A.1)$$

with G the Green's function and N_B and N_I the source spectra of boundary sources and the isolated source, respectively. This section is formulated in the frequency domain. The cross-correlation of this wavefield at location \mathbf{r} with the wavefield recorded on a master station at \mathbf{r}_M is given by (Equation 6 of Schippkus et al., 2022)

$$\langle u(\mathbf{r})u^*(\mathbf{r}_M)\rangle = \frac{\rho c|N_B|^2}{2} \left(G(\mathbf{r}, \mathbf{r}_M) + G^*(\mathbf{r}, \mathbf{r}_M) \right) + |N_I|^2 G(\mathbf{r}, \mathbf{r}_N) G^*(\mathbf{r}_M, \mathbf{r}_N) ,$$
(A.2)

with ρ the mass density of the medium and c the propagation velocity. The first term describes the contribution of uncorrelated sources on the boundary S surrounding the stations, which usually arises in seismic interferometry (as in Wapenaar et al., 2005), and the second term describes the contribution of the isolated noise source. The relation of these terms has been investigated by Schippkus et al. (2022), who demonstrate how the direct arrivals of these two wavefield contributions interfere for certain station geometries, leading to biased surface wave dispersion measurements. In their modelling, the authors assumed the source term of the isolated source N_I to be a wavelet, excited once.

Here, we expand upon this idea by considering the isolated noise source to be excited multiple times in a correlated manner. For illustration purposes, we express its source term as $N_I = W_I E_I$, with a wavelet W_I and excitation pattern E_I . The contribution of the isolated noise source to the correlation wavefield is hence

$$|W_I|^2 |E_I|^2 G(\mathbf{r}, \mathbf{r}_N) G^*(\mathbf{r}_M, \mathbf{r}_N) . \tag{A.3}$$

A simple example of an isolated noise source exciting a Ricker wavelet, repeating 5 times with a 20 sec. interval, illustrates how such a source manifests in correlation functions (Figure A.3). For such a source, the excitation pattern is a time series with 1 at every interval of 20 sec. (5 times), and 0 elsewhere.

The auto-correlation of the wavelet $|W_I|^2$ (Figure A.3a), auto-correlation of the excitation pattern $|E_I|^2$ (Figure A.3b), and cross-correlation of the Green's functions $G(\mathbf{r}, \mathbf{r}_N)G^*(\mathbf{r}_M, \mathbf{r}_N)$ for surface waves in a homogeneous, isotropic, acoustic medium and an arbitrary geometry (Figure A.3c) are convolved to result in a repeating wavelet with the same 20 sec. interval, present in the correlation wavefield (Figure A.3d). These repeating wavelets represent direct waves emitted from the isolated source location.

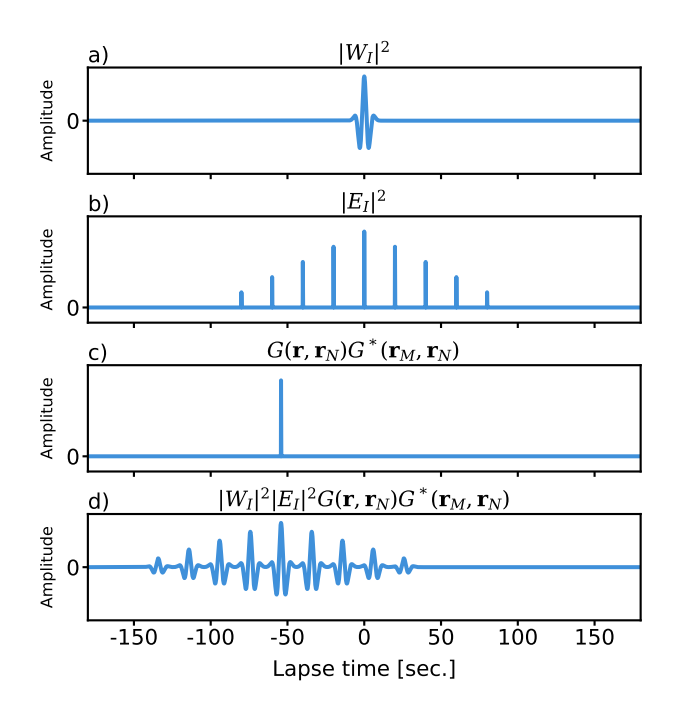


Figure A.3: A repeating isolated noise source produces repeating direct waves in correlation functions, depicted in time domain. a) Auto-correlation of the wavelet $|W_I|^2$. b) Auto-correlation of the excitation pattern $|E_I|^2$ with a regular 20 sec. interval, excited 5 times. Note that amplitudes decay by 1/5 every interval away from 0 sec. lapse time. c) Cross-correlation of the Green's functions between the isolated noise source and both station locations for an arbitrary geometry. d) Second term of the correlation wavefield (Equation A.3, the convolution of a-c), where each arriving wavelet represents a direct wave emitted from the isolated noise source at \mathbf{r}_N .

A sketch of the correlation wavefield in the presence of a repeating impulsive isolated noise source helps illustrate its evolution with lapse time (Figure A.4). The wavefield is comprised of the two contributions by boundary sources (first term of Equation A.2, yellow in Figure A.4) and the isolated noise source (Equation A.3, purple in Figure A.4). The boundary source contribution converges onto the master station at negative lapse times (the acausal part), and

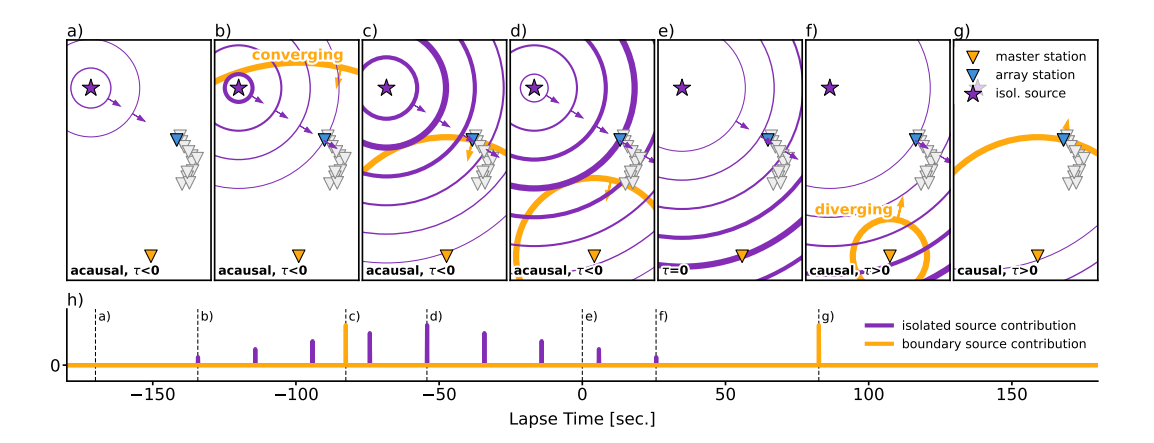


Figure A.4: Schematic illustration of the correlation wavefield in the presence of a repeating impulsive source (5 excitations, 20 sec. interval, same as in Figure A.3). We remove the wavelet for improved clarity. a-g) Snapshots of the correlation wavefield at different lapse times, indicated by dashed lines in h). The contributions of the isolated source (purple lines) and boundary sources surrounding the master and array stations (yellow line) propagate through the medium. Line thickness indicates amplitude. h) Correlation function between the array station and the master station, color-coded by isolated source and boundary source contribution (purple and yellow, respectively). Dashed vertical lines mark the lapse time snapshots displayed in a-g. The acausal part of the correlation function contains repeating waves propagating from the isolated source and the boundary source contribution converging onto the master station (a-d). At lapse time $\tau = 0$, both the main arrival of the isolated source contribution and the boundary source contribution reach the master station (e). At causal lapse time, the last arrivals of the isolated source reach the array station (f) and finally the diverging contribution of the boundary sources (g).

This is the expected contribution that usually arises in seismic interferometry. The repeating isolated noise source induces waves that emerge earlier and with lower amplitude than the main arrival (Figure A.4a) and eventually reach the array station (A.4b). The main arrival (highest amplitude, indicated by line thickness) of the isolated noise source emerges at $\tau = -|\mathbf{r}_M - \mathbf{r}_N|/c$ and touches the boundary source contribution along the line connecting the isolated source and master station (c-f, as in Schippkus et al., 2022). At lapse time $\tau = 0$, both the wavefield contribution by boundary sources and the main arrival of the isolated noise source reach the master station (Figure A.4e). At causal lapse times, the last repeating waves from the isolated noise source reach the array station (Figure A.4f) before the boundary source contribution diverging

from the master station arrives at the at array station (Figure A.4g). The exact timing of each arrival depends on the geometry of isolated source, master station, and array stations, as well as the excitation pattern.

Note that the repeating direct waves from the isolated noise source are asymmetrical in lapse time (Figs. A.3, A.4), because there is no part of the correlation wavefield converging onto the isolated noise source (Schippkus et al., 2022). How strongly these repeating direct waves manifest depends on how highly correlated the isolated source is with itself throughout time. The example presented here constitutes the most extreme case, i.e., identical wavelet and exactly regular excitation pattern. Even under these conditions, amplitudes decay linearly with time due to the finite length of the excitation pattern (Figure A.3b). In this example, the amplitude of the excitation pattern auto-correlation decreases by 1/5 of the maximum amplitude with each interval away from 0 sec., because the source is excited 5 times. Slight variations in amplitude, shape of the wavelet, or excitation timing lead to reduced correlation, and thus repeating direct waves with reduced amplitude or different shape. If there was no correlation, the repeating waves would disappear. The main arrival would remain.

To confirm the repeating wavelets in the correlation functions indeed represent repeating direct waves emitted from the isolated noise source, we model a master station in Italy (same location as IV.BRMO), array stations in Southern Germany (same locations as the Gräfenberg array), 1000 boundary sources surrounding the stations in a small-circle with 1000 km distance to them, as well as a repeating isolated noise source Southwest of Iceland (Figure A.5a). All sources excite Ricker wavelets, and only the isolated noise source repeats it 50 times with a 150 sec. interval (similar to Figs. A.3, A.4). We compute synthetic surface wave seismograms by assuming a homogeneous, isotropic, acoustic half-space with a medium velocity v = 3 km/s for simplicity (i.e., Green's functions are of the form $e^{-i\omega x/v}$), and compute cross correlations of those waveforms. During the calculations, we treat boundary sources and the isolated noise source separately in accordance with equation (A.2). The

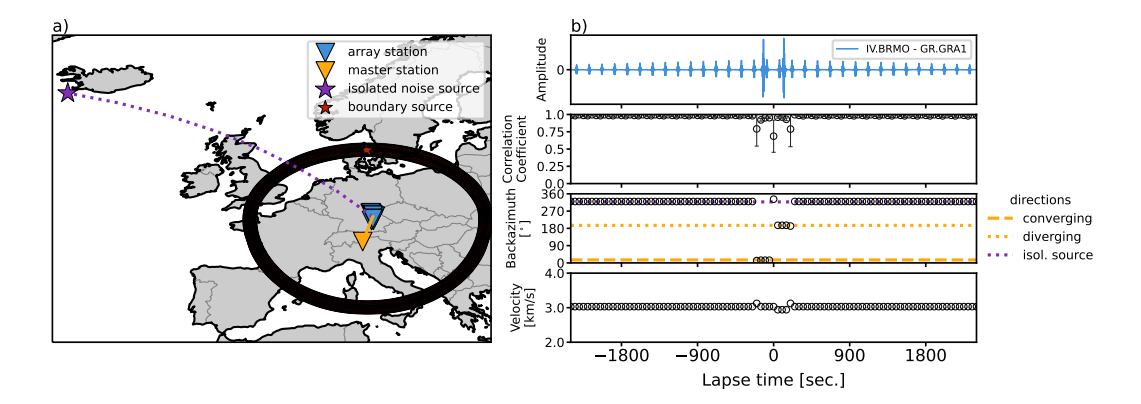


Figure A.5: Beamforming synthetic cross-correlation functions detects repeating direct waves from the regularly repeating isolated noise source. a) Overview map: master station (orange triangle), array stations (blue triangle), boundary sources in a small circle surronding the stations (red stars) and the isolated noise source Southwest of Iceland (purple star). b) Beamforming results: sample cross-correlation between master station and one array station, mean correlation-coefficients between windowed correlation functions and beams, detected direction of arrival, and estimated phase velocity. The boundary source contribution to the correlation wavefield converging onto and diverging from the master station (orange lines, first term in Equation A.2) is detected as well as repeating direct waves from the isolated noise source (purple line, second term in Equation A.2).

maximum amplitude of the isolated noise source contribution is scaled to 1/4 of the boundary source contribution to distinguish them easily (Figure A.5b, top panel). The correlation wavefield contains both wavefield contributions. Beamforming the cross-correlation functions between the master station and all array stations detects three directions of arrival (Figure A.5b, third panel): the first term of the correlation wavefield converging onto the master station at negative lapse time (dashed orange line) and diverging from the master station at positive lapse time (dotted orange line), and repeating direct waves from the isolated source (purple dotted line) throughout the correlation function. The estimated phase velocity of ~ 3 km/s is the medium velocity (Figure A.5b, bottom panel). Note that the correlation functions match exactly with the beam (correlation coefficent of 1) only for time windows that do not contain both contributions simultaneously (Figure A.5b, second panel).

This example illustrates the principle behind repeating direct waves emerging in correlation functions. However, we observed this effect on field data of secondary ocean microseisms (Figs. A.1, A.2), which are better described as

continuously acting sources, which we introduce in the following.

A.1.4 Continuously acting isolated noise sources

To describe the suspected isolated noise source (Figs. A.1, A.2) as a continuously acting microseism source, we rely on the parametrization employed by Gualtieri et al. (2020) (Equation 3 therein). The surface pressure P at colatitude θ and longitude ϕ excited by the secondary microseism mechanism is described as a superposition of many harmonics

$$P(t,\theta,\phi) = \sum_{i=1}^{H} A(f_i,\theta,\phi) \cos(2\pi f_i t + \Phi_i), \tag{A.4}$$

with H the number of harmonics, A the amplitude of the harmonic frequency f_i , and $\Phi_i \in [0, 2\pi)$ its phase, sampled uniformly random. The amplitude A relates to the power spectral density of ocean gravity waves and incorporates local site effects, and is described in more detail by Gualtieri et al. (2020). For our considerations, we neglect the amplitude term (A = 1), because we investigate a fairly narrow frequency band and the exact amplitude of each harmonic is irrelevant for explaining the effect observed in this study. In the following, we use $P(\theta,\phi)$ (the spectrum of $P(t,\theta,\phi)$) with harmonics from 0.1 to 0.3 Hz directly as the source term N_I (Figure A.6a). Its auto-correlation (Figure A.6b), convolved with the same Green's function cross-correlation as above (Figure A.3c) contains one clear main arrival and weak, repeating direct waves (Figure A.6c). These repeating waves excited by a microseism source have much lower amplitude and inconsistent shape compared to a repeating impulsive isolated noise source (Figure A.3) due to decreased correlation of the source term with itself throughout time.

We repeat the numerical simulation above (Figure A.5) with $P(\theta, \phi)$ as the source term for both boundary and isolated noise sources (Figure A.7). Both contributions to the correlation wavefield are scaled to have similar amplitudes. A secondary microseism source produces repeating direct waves in correlation wavefields (Figure A.7b), similar to the regularly repeating source (Figure

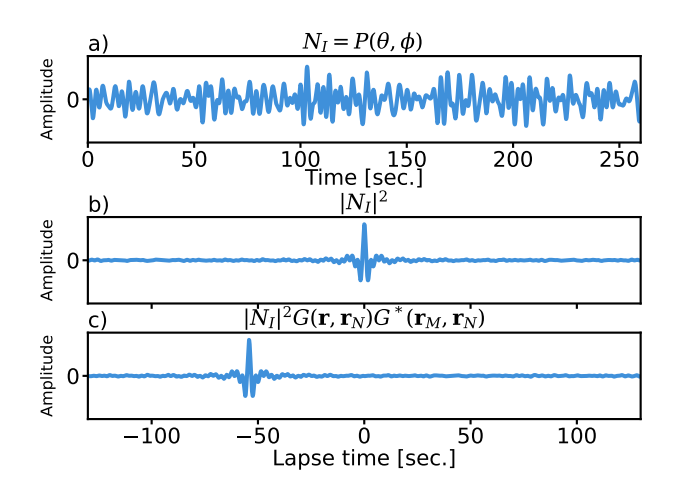


Figure A.6: Contribution to the correlation wavefield by a continuously acting isolated noise source. a) Source term for a secondary microseism source, if all harmonics between 0.1 and 0.3 Hz are excited with a uniformly random phase $\Phi_i \in [0, 2\pi)$ and equal amplitude A = 1 (Equation A.4). b) Auto-correlation of the source term $|N_I|^2$. c) Convolution of $|N_I|^2$ with the same Green's function cross-correlation as in Figure A.3c, i.e., the second term of the correlation wavefield (Equation A.2), with a main arrival and low-amplitude, repeating direct waves throughout the coda.

A.5). Near the main arrival of the isolated source (at ~ -100 sec., after the acausal arrival due to boundary sources) and throughout the coda, repeating direct waves from the isolated noise source location are detected as most coherent. Distinct main arrivals (the "spurious" arrival) have been observed for localised microseism sources before (Zeng and Ni, 2010; Retailleau et al., 2017). These main arrivals must arrive in-between the acausal and causal arrivals of the boundary source contribution (Schippkus et al., 2022). In this study, we do not observe a particularly clear main arrival on field data (Figs. A.1, A.2). Still, the coda of the field data correlation wavefields appears to be dominated by repeating waves from isolated noise sources. Correlation coefficients of the synthetic correlation functions with the beams for each window reach ~ 1 for the main causal arrival, and ~ 0.75 for the acausal arrival due to interference with the isolated source arrival (Figure A.7b). Throughout the coda, correlation coefficients do not exceed 0.75 significantly, because continuously acting boundary sources also induce a repeating contribution in the correlation wavefield. In other words, the best beam does not represent the correlation functions entirely, even under the ideal conditions considered here, i.e., no heterogeneous structure, no dispersion, and no scattering.

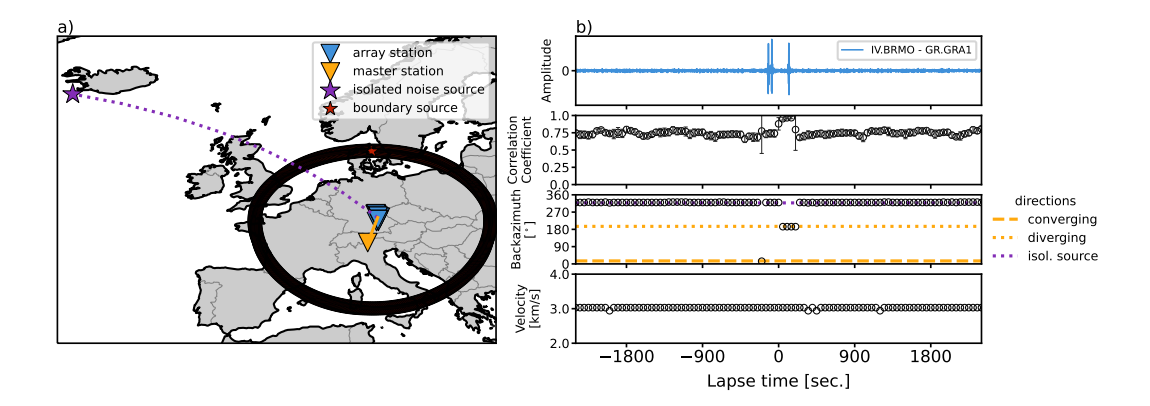


Figure A.7: Same as Figure A.5 but for secondary microseism source terms for both boundary and isolated sources. Both contributions to the correlation wavefield are scaled to have similar amplitudes. Distinct main arrival (the "spurious" arrival) of the isolated noise source at ~ -100 sec. lapse time. For this arrival and throughout the coda, direct waves from the isolated source are detected as most coherent.

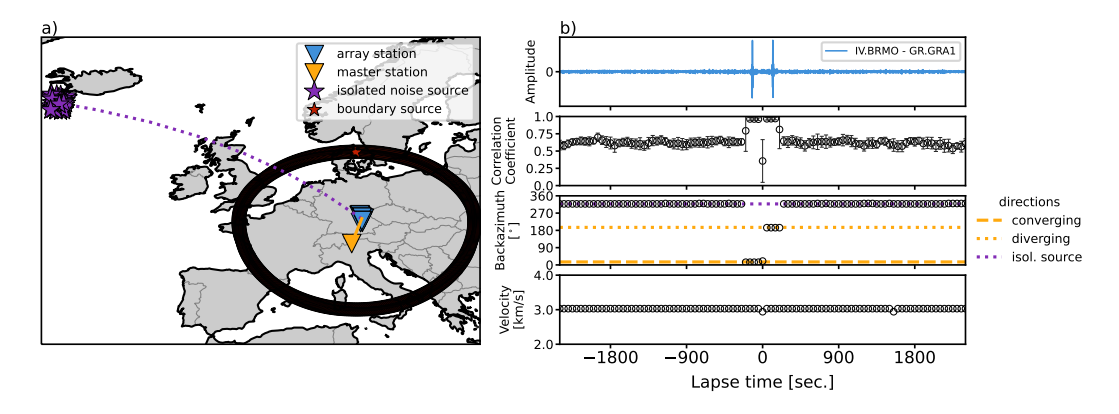


Figure A.8: Same as Figure A.7 but for a cluster of isolated sources. Amplitudes of the summed isolated noise source contribution is scaled to 1/10 of the boundary source contribution. No distinct spurious arrival but coda still dominated by repeating direct waves from the isolated noise source cluster.

To account for the fact we do not observe a distinct main arrival due to an isolated noise source in our field data correlations and to approximate a more realistic scenario by considering an extended source region, we place a cluster of 50 isolated noise sources Southwest of Iceland, each with a random realisation of the source term $P(\theta, \phi)$ and repeat the computations (Figure A.8). The wavefield contributions of those isolated noise sources, where each isolated source produces an additional term in equation (A.2), interfere to mask the main arrival (Figure A.8b). The amplitudes of the summed isolated noise source cluster contribution is scaled to 1/10 of the boundary source contribution. Beamforming correlation functions again detects the converging and diverging

part of the boundary source contribution, as well as the isolated noise source cluster as dominant throughout the coda (Figure A.8b). Correlation coefficients with the beams stabilise at ~ 0.65 in the coda, and are lower than for the case of a single source (Figure A.7b).

Finally, we place a second cluster of 50 isolated noise sources Northwest of the Iberian Peninsula (Figure A.9a) to account for the observation that within the range of directions toward the Northern Atlantic, two distinct directions appear to dominate (Figs. A.1, A.2). Both clusters of isolated noise sources are treated separately and their combined amplitudes are again scaled to 1/10 of the boundary source contribution. Beamforming detects either one of the clusters as dominant, seemingly randomly throughout lapse time (Figure A.9b). Mean correlation coefficients with the beams are ~ 0.55 throughout the coda. This numerical simulation produces beamforming results closely resembling the measurements on field data correlation functions (Figs. A.1, A.2) and confirms that clusters of isolated noise sources produce repeating direct waves.

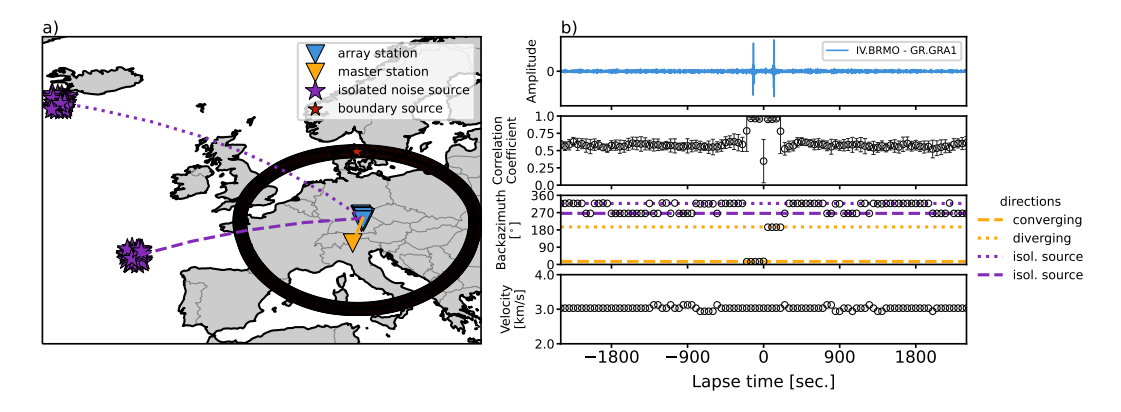


Figure A.9: Same as Figure A.8 but for two clusters of isolated noise sources. The additional cluster is placed Northwest of the Iberian Peninsula. The backazimuth to that cluster is indicated by a purple dashed line (a & b, third panel). Amplitudes of the isolated noise source contribution is scaled to 1/10 of the boundary source contribution. No distinct spurious arrival. Beamforming detects either of the two clusters at a given lapse time in the coda as dominant.

A.1.5 Discussion

In this study, we observe repeating direct waves propagating from isolated noise sources in the coda of correlation functions. We reproduce the observations by numerical modelling of continuously acting isolated sources.

The most significant question our analysis raises is: are repeating direct waves from isolated noise sources more dominant than multiply scattered waves, originating from the master station, also for individual correlation functions? If they were, our observations would have far-reaching implications. Beamforming, however, only shows that the contribution by isolated noise sources is more coherent across an array of stations (Figs. A.1, A.2). It is not surprising that multiply scattered waves can be incoherent across an array. To address this aspect, we compute correlation coefficients of all correlation functions with the beam in each beamforming window. These reach 0.75 to 0.9 (never 1) for the expected stronger, coherent acausal arrival on field data correlations (Figs. A.1, A.2), which indicates that not all factors are accounted for during beamforming, namely heterogeneous structure, scattering, elastic wave propagation, and additional isolated sources. Still, these correlation coefficients provide a benchmark of what can be expected for the most coherent part of the correlation wavefield. In our numerical simulations, correlation coefficients are ~ 1 for the main arrivals without the interference of distinct spurious arrivals (Figs. A.5, A.7, A.8, A.9). Throughout the coda, we observe that correlation coefficients remain nearly constant for both the field data examples (~ 0.4 , Figs. A.1, A.2) and the numerical simulations, decreasing with increasing complexity of the original wavefield from one isolated noise source (~ 0.75 , Figure A.7), to a cluster of sources (~ 0.65 , Figure A.8), to two clusters (~ 0.55 , Figure A.9). Without taking into account the additional factors mentioned above (scattering, heterogeneous structure, or elastic waves), we reproduce a match between the modelled correlation functions and beams, comparable to the field data results. It is therefore reasonable to assume that the coda is not dominated by scattered waves, at least for absolute lapse times larger than a few hundred seconds.

At lapse times close to the direct arrivals from the master station (up to a few hundred seconds), correlation coefficients are higher than for the later coda and a transition to the stable regime observed in the later coda appears to manifest (Figs. A.1, A.2). In the early coda, scattered waves are likely

dominant and thus also coherent in the correlation wavefield, although question arise about the degree of scattering. However, first tests on whether scattered waves are more coherent when the master station is much closer have shown no noticable difference in the beamforming results. The distinction between early coda and late coda arises, because amplitudes of the two correlation wavefield contributions decay for different reasons. Multiply scattered waves originating from the master station decay due to attenuation during wave propagation, whereas repeating direct waves from isolated noise sources decay only due to correlation of the source term with itself through time (Figs. A.3,A.6). As demonstrated above, even under ideal circumstances, amplitudes of repeating direct waves in correlation functions decay due to the finite length of the source and signal considered (Figure A.3).

In the later coda (absolute lapse times larger than a few hundred seconds), the commonly held assumption that the coda of a correlation wavefield is comprised dominantly, or even exclusively, of multiply scattered waves appears to be false. The beams pointing towards isolated noise sources represent a significant fraction of the correlation wavefield coda (Figs. A.1, A.2). Instead of spatially sampling the medium in a statistical manner (Margerin et al., 2016), the late coda, and thus measured velocity changes, may be dominantly sensitive to the path from the isolated noise source to the array station. Here, it is important to be clear about the nature of the coda and measurement principle. In the standard coda wave interferometry model, coda waves originate from the master station, are multiply scattered, and eventually reach the other receiver. A measured velocity change is then sensitive to this entire path. Because there is no clear way to know where exactly the wave has been and thus where the change has happened, recently developed coda wave sensitivity kernels are statistical descriptions of where the wave might have been, depending on the scattering properties of the medium (Margerin et al., 2016). However, if one would repeat the beamforming measurement described above, e.g., daily, to estimate the velocity of seismic waves in the coda, a potential velocity variation of those waves over time would have happened within the array, assuming constant sources. The standard coda wave interferometry measurement, in

contrast, is performed on single correlation functions. If the measurement is performed in some part of the coda where repeating waves by isolated sources dominate, velocity variations may then be sensitive to the entire propagation path from isolated source to receiver, similar to the case where the coda is dominated by scattered waves and the sensitivity is along the path from master station to receiver. The difference here lies in the origin of the correlation wavefield contribution probed during the measurement and the ability to constrain the velocity change spatially. The main hypothesis in this paper is that the repeating waves we observe in beamforming originate from the isolated source, not the master station (Figure A.4).

A similar effect occurs in the presence of a strong nearby scatterer (van Dinther et al., 2021). As the multiply scattered part of the correlation wavefield reaches the strong scatterer, spatial sensitivity focuses along the path between stations and scatterer. In other words, the scatterer "emits" a direct wave, induced by the master station, that is recorded in the coda of the correlation function. This principle is similar to our considerations here, with the major difference that, in the modelling of van Dinther et al. (2021), the direct wave propagating from the scatterer originates from the master station. For isolated noise sources, direct waves originate from the source. The master station has no impact on the isolated source contribution to the correlation wavefield, as long as it coherently records the same isolated noise sources as the array stations, as the two field data examples suggest (Figs. A.1, A.2). We have no reason to suspect a strong scatterer to the West of the Gräfenberg array that could explain our measurements. Instead, our measurements are consistent with repeating direct waves from isolated noise sources, and reproduced by modelling without considering any scatterers. This means that different station pairs do not lead to different spatial sensitivity when recording such repeating direct waves. In some contexts, this may be advantageous by allowing repeated measurement of a repeating or continuous isolated source by considering multiple master stations. In the context of seismic monitoring of relative velocity variations, the impact of such sources has to be carefully considered.

The presence of repeating direct waves in the very late coda (30 minutes and more) furthermore challenges the common assumption that the very late coda of correlation wavefields is dominated by instrument noise and contains no useful signal. The very late coda is commonly used as a noise window for the estimation of signal-to-noise ratios of correlation functions, also for coda windows. We show that the very late coda does instead contain useful information, because repeating direct waves from isolated noise sources are still detected by beamforming (Figs. A.1, A.2). This also suggests amplitudes decay only slowly due to low correlation of the isolated source with itself over time (compared to Figure A.3), at least for the correlation wavefields investigated here, which were stacked over two years.

The early coda of correlation wavefields likely contains a significant contribution of scattered waves, as well as direct repeating waves from isolated noise sources. This suggests great care should be taken in measuring velocity variations and attributing them spatially also for the early coda. Common strategies to measure velocity variations, e.g., the stretching method (Lobkis and Weaver, 2003), assume that absolute timing delays increase with lapse time, because the seismic waves spent more time in the changed medium. For the contribution by repeating direct waves, stretching should not occur since absolute time delays are likely constant throughout the coda, as long as the isolated source does not change. A strategy that involves estimating the degree of stretching throughout the coda may give insight into the dominant regime (scattered waves vs. repeating waves) and whether the measurement approach is applicable. A different strategy to discriminate the correlation wavefield contributions may be to include measurements of wavefield gradients, which allow to separate the seismic wavefield using only single stations Sollberger et al. (2023).

Further questions arise about the temporal sensitivity of measured velocity variations. When considering scattered waves in the coda, velocity variation measurements are usually attributed to the entire time window used for correlation, e.g, a single measurement that represents an entire day. Repeating direct waves from isolated noise sources should in principle allow to improve

temporal resolution, because arrivals at different lapse times likely have different temporal sensitivity in raw signal time domain, i.e., at what points in time the raw signal was recorded. However, it is not immediately obvious what time exactly a specific repeated arrival is sensitive to. This is a target for future studies.

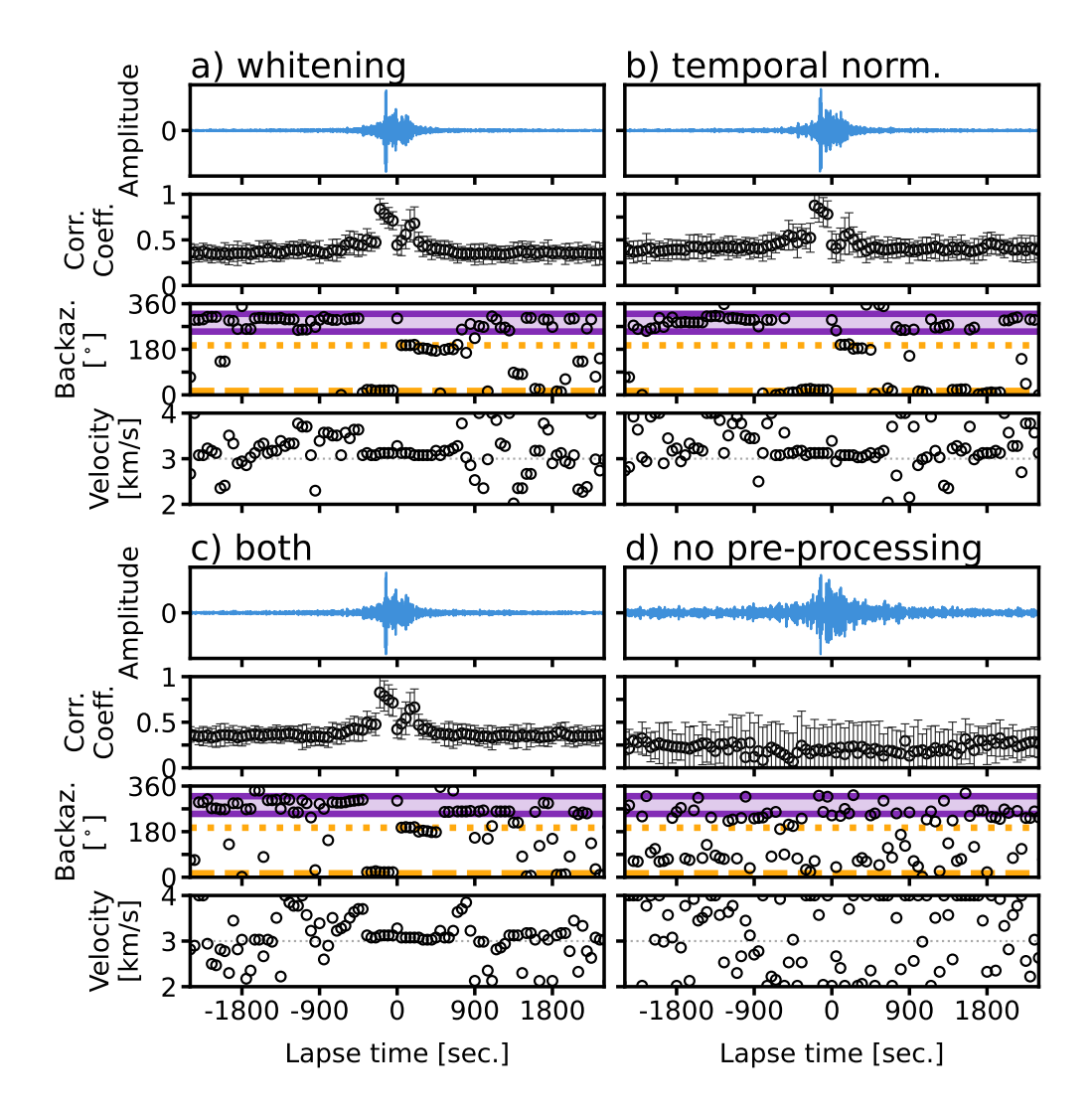


Figure A.10: Impact of pre-processing scheme on the detection of repeating direct waves for master station IV.BRMO. a) Same as Figure A.1b. b) Sample correlation function and beamforming result, if only temporal normalisation is applied. c) Results when both whitening and temporal normalisation are applied. d) Results when neither pre-processing is applied.

Pre-processing of seismic records before cross-correlation plays an important role when investigating cross correlations of ambient seismic noise. We apply spectral whitening, a commonly adopted pre-processing strategy (Bensen et al., 2007). Spectral whitening is the normalisation of the amplitude spectrum

before cross-correlation, often with a water level or smoothed spectrum to avoid introducing artefacts. Whitening is often successful in suppressing the impact of near-monochromatic signals, e.g., in the context of the 26 sec. microseism in the Gulf of Guinea (Bensen et al., 2007; Bruland and Hadziioannou, 2023) or wind turbine noise (Schippkus et al., 2022). On the other hand, whitening will also emphasise signals with relatively low amplitude in the original data. To confirm that our interpretation of the results above is not significantly biased by the processing strategy, we repeat the measurements for master station IV.BRMO (Figure A.1) with temporal normalisation, both whitening and temporal normalisation, and neither pre-processing (Figure A.10). Temporal normalisation (running window average) is performed in a 5 sec. moving window. As long as any processing to stabilise the correlation functions is applied (Figure A.10a-c), the fundamental observation of repeating direct waves remains. Slight differences emerge in the correlation functions themselves, and also which direction and velocity are detected at a given lapse time. Temporal normalisation is commonly applied in studies that measure relative velocity variations, often in its most extreme version one-bit normalisation. Here we demonstrate that common pre-processing schemes produce correlation functions with repeating direct waves. Without any processing, however, results become unstable and beamforming neither detects stable directions of arrival nor gives consistent phase velocity estimates (Figure A.10d). Correlation functions are more stable after such pre-processing, as is commonly observed, because these approaches (in addition to addressing some data glitches) reduce the impact of certain isolated noise sources on the recorded wavefield, in particular from transient high-amplitude sources (e.g., earthquakes) and continuous nearmonochromatic sources (e.g., machinery). The sources that remain as dominant, after this pre-processing is applied, are continuously acting broadband sources (e.g., ocean microseisms) as is confirmed by beamforming (Figs. A.1 & A.2).

The temporal stability of ocean microseism sources that we impose in our modelling has been observed on field data correlations before. Zeng and Ni (2010) computed and stacked correlations over one year that show clear spurious energy due to a localized microseism source in Japan. Similarly, Retailleau

et al. (2017) found localized microseism sources off the coasts of Iceland and Ireland, also in correlations stacked over one year. It may be unintuitive that ocean microseisms, often assumed to be a largely random process, would show any coherence at all. These previous and our results are clear indications that indeed the secondary microseism mechanism generates coherent sources that are somewhat stable over time. We are, however, not aware of a microseism source model that incorporates all these factors satisfactorily. Instead, we follow the current standard formulation, i.e., each frequency is excited with random but constant phase (Gualtieri et al., 2020). Investigations on how varying temporal source stability and stacking influence the beamforming detections or measured velocity changes will likely be part of future work.

It may also be surprising that the highly idealised Earth model employed in our simulations, i.e., Green's functions in an acoustic homogeneous half-space, is sufficient to reproduce our observations on field data to first order. We do not take any elastic wave propagation effects such as scattering into account. This suggests that these effects certainly present in real Earth structure and thus field data may play a less important role than often thought, at least for the specific case investigated here: the nature of the coda of ambient noise correlations.

Machinery- or traffic-based monitoring of velocity variations is likely similarly affected by the findings in this study. Rotating machinery, such as generators in wind turbines (Friedrich et al., 2018; Schippkus et al., 2020; Nagel et al., 2021), likely have source terms that are significantly correlated throughout time due to their mechanism, with higher correlation than ocean microseisms. These sources could produce repeating direct waves with high amplitude. Traffic, e.g., trains repeatedly passing the same spot, resembles repeatedly acting noise sources (as in Figure A.3), although with more complex wavelets and longer intervals. In case of traffic at a regular interval, e.g., trains on a schedule, the late coda of the correlation wavefield could allow to extract their signature reliably. Recently, approaches that identify and select appropriate time windows to use for cross-correlation and subsequent velocity monitoring have emerged

(e.g., Yates et al., 2022; Sheng et al., 2023). These approaches are motivated by the realisation that correlation wavefields can be highly complex and depend significantly on the presence of isolated noise sources, similar to this study. Still, our findings also have impact on these strategies. In time windows where an isolated noise source is known to be particularly active, repeating direct waves may still emerge and coincide with the coda of that source, depending on the source signature and length of time window considered for cross-correlation. Further investigations on this aspect may help improve the accuracy of detected velocity changes in time and space.

A.1.6 Conclusion

Continuously acting isolated noise sources generate repeating direct waves that may dominate the coda of correlation wavefields, as observed on field data correlations (Figs. A.1, A.2) and reproduced by numerical simulations (Figs. A.3-A.9). In the simulations, we start from the established concept of an isolated noise source (Schippkus et al., 2022) that repeatedly excites a wavelet to illustrate the fundamental principle of how repeated direct waves emerge in correlation functions (Figs. A.3, A.5). To better reproduce the measurements on field data correlations, we model an isolated secondary microseism source, starting with one source (Figure A.7), which shows a distinct main arrival of that source (the "spurious arrival") that is not always observed clearly on field data correlations. With a cluster of isolated noise sources, mimicking an extended source region, this main arrival disappears due to interference between the sources (Figure A.8). Finally, we model two clusters to show that either may be detected at a given lapse time (Figure A.9), reliably reproducing the observations on our field data correlation wavefields (Figs. A.1, A.2). Throughout our modelling, we keep the numerical setup as simple as possible to emphasise the impact of only the isolated noise sources, i.e., we exclude any influence due to heterogeneous Earth structure, any elastic wave propagation effects such as multiple wave types or conversion between them, and importantly do not include any scattering.

Our results suggest that the coda of correlation wavefields should not be assumed to be mainly comprised of scattered waves, which originated from the master station. Instead, repeating direct waves from isolated noise sources may dominate. There is likely a transition in dominating regime from scattered waves (in the early coda) to repeating direct waves (in the late coda). This occurs, because amplitudes of scattered waves decay due to attenuation, whereas repeating direct waves decay slower only due to the auto-correlation of the source term throughout time. This has implications for ambient noise correlation based monitoring applications, commonly assuming multiply scattered waves, and raises questions about the validity of such measurements, in particular about the spatial sensitivity.

This study also opens up new opportunities for future research. In the presence of a continuously acting isolated noise source, the very late coda of correlation wavefields retains the source signature and is not dominated by instrument noise. This in principle allows to extract seismic waves repeatedly propagating along the same path, undisturbed by other contributions, which may be an attractive target for monitoring applications. The spatial distribution of isolated noise sources, however, severely limits the spatial sensitivity of the very late correlation wavefield coda.

Data availability and Resources

This manuscript is fully reproducible. All computed correlation functions and code necessary to produce all figures are hosted on Github and Zenodo (Schippkus, 2023). Seismograms used in this study to compute correlation functions are provided by the network operators of the German Regional Seismic Network (GR, Federal Institute for Geosciences and Natural Resources, 1976), Polish Seismological Network (PL, Polish Academy of Sciences (PAN) Polskiej Akademii Nauk, 1990), and Italian National Seismic Network (IV, Istituto Nazionale di Geofisica e Vulcanologia (INGV), 2005). We rely on open-source software for our computations and visualisations (Hunter, 2007; Met Office,

2010; Krischer et al., 2015; Harris et al., 2020; Virtanen et al., 2020). Color sequences are designed to be accessible (Petroff, 2021).

Acknowledgements

The authors thank Joshua Russel and one anonymous reviewer for their insightful comments that helped improve the manuscript, as well as the handling editor Lise Retailleau. The authors acknowledge funding provided by the Emmy Noether program (HA7019/1-1) of the German Research Foundation (DFG). The authors acknowledge funding provided by the European Union's Horizon 2020 research and innovation programme under the Marie Skłodowska-Curie grant agreement No. 955515 (SPIN ITN).

A.2 Seasonality of microseisms in southern California from 6C ground motions

Le Tang¹, Heiner Igel¹, Jean-Paul Montagner², Celine Hadziioannou³, Mahsa Safarkhani³, Frank Vernon⁴

- 1 Department of Earth and Environmental Sciences, Ludwig-Maximilians-Universität München, 80333, Munich, Germany
- 2 Institut de Physique du Globe de Paris, Université de Paris, 75238, Paris, France
- 3 Institute of Geophysics, University of Hamburg, 20146, Hamburg, Germany
- 4 Institute of Geophysics and Planetary Physics, University of California San Diego, La Jolla, CA, USA

Corresponding author: tangle0129@gmail.com

This paper is available on https://essopenarchive.org/doi/full/10.22541/essoar.172901301.13982448.

Author Contribution: Mahsa Safarkhani: Methodology, Formal Analysis, Investigation, Data Curation, Writing - Review and Editing, Visualization

- A single 6C observation is capable of revealing the seasonality of microseismic sources.
- Array-derived rotational motions are highly sensitive to atmospheric pressureinduced ground deformation.
- The secondary microseismic Love waves show significant seasonal changes in the southern California region.

Abstract

Ocean waves interact with the solid Earth, generating two dominant signals called microseisms, which carry information about energy exchange between different Earth systems. Here, we show that a single 6C observation can simultaneously reveal seasonal azimuthal variations of the Rayleigh and Love waves. We employ rotational motions at the Pinon Flat Observatory to investigate two dominant microseismic sources: primary (10-20s) and secondary (3-10s) microseisms. Our results indicate that secondary microseismic Rayleigh waves show minor seasonal changes. In contrast, secondary microseismic Love waves demonstrate significant seasonality. The notable difference offers new insights into the Love wave generation mechanism, suggesting that ocean bathymetry may be crucial in generating Love waves near this region. Additionally, we find that the rotational motion of primary microseisms recorded by a seismic array is more sensitive to ground deformation caused by changes in atmospheric pressure. It provides valuable insights for future joint observations of different Earth systems.

Plain Language Summary The ubiquitous ambient seismic noise recorded by seismographs with a period of 3-20s can be explained by the interaction between ocean waves and the solid Earth. The most convincing mechanism indicates that the interaction between two opposite ocean waves generates a vertical force that causes vertical vibrations on the seafloor. Therefore, it is reasonable to observe Rayleigh waves in the secondary microseismic noise (3-10s), but it cannot explain the observed secondary microseismic Love waves. To

better understand the generation mechanisms of these two different vibrations, we employ the rotational ground motion to locate the source of microseismic noise. Theoretically, the vertical component of rotation is only sensitive to SH-type waves, while the horizontal component only records the SV-type waves. The combination of translational motions and rotational motions provides the feasibility of estimating wave propagation directions at a single seismometer, making it easy to track the noise source, especially the Love waves, which are not yet fully understood.

A.2.1 Introduction

The interaction between ocean waves and the solid Earth contributes to the generation of two ubiquitous dominant microseisms Longuet-Higgins (1950); Obrebski et al. (2012); Stutzmann et al. (2012); Ardhuin et al. (2015, 2019); Gualtieri et al. (2020): primary microseismic noise (10-20s) and secondary microseismic noise (3-10s). It is currently widely accepted that ocean waves directly interact with the seafloor in very shallow water and can explain the generation mechanism of primary microseismic Rayleigh and Love waves Nishida et al. (2008); Fukao et al. (2010); Saito (2010); Gualtieri et al. (2021b) at the period of around 10-20s, and the origin of secondary microseismic Rayleigh waves is due to the interaction of two opposite swells, which can produce secondorder pressures that interact with the seafloor anywhere Longuet-Higgins (1950); Obrebski et al. (2012). Theoretically, Rayleigh waves should dominate secondary microseismic events because of the vertical force loaded by the ocean waves on the seafloor. However, it cannot explain the generation mechanism of secondary microseismic Love waves. The current hypotheses for the mechanism of the secondary microseismic Love waves suggest that the presence of bathymetric inclines and topographic coupling enables leading to the splitting of the vertical secondary-order pressure force in a component tangent to inclines which can be responsible for the Love waves Rind and Down (1979); Gualtieri et al. (2020, 2021b); Le Pape et al. (2021). In addition, the lateral heterogeneity within the Earth may also lead to the generation of Love waves due to scattering

effects Rind and Down (1979); Ziane and Hadziioannou (2019); Gualtieri et al. (2020). Despite this, seismologists have been debating the origin of secondary microseismic Love waves for decades. To better understand the generation mechanisms of these two different vibrations, especially the Love waves, accurately locating and tracking microseismic sources has always been a big challenge.

Northern Hemisphere storms have stronger winter peaks compared to Southern Hemisphere storms Colosi et al. (2021), and the seasonality of storms suggests that the interaction between ocean waves and the solid Earth follows seasonal variations. It is expected and understandable that the microseismic source shows seasonality Schulte-Pelkum et al. (2004); Tanimoto et al. (2006); Grob et al. (2011); Schimmel et al. (2011); Stutzmann et al. (2012); Juretzek and Hadziioannou (2016); Tanimoto et al. (2016a); Shabtian et al. (2024). Due to their different generation mechanisms, the azimuth of the primary microseismic Rayleigh waves has strong seasonal variations, while the azimuth variation of the secondary microseismic Rayleigh waves is not significant in the southern California region Stehly et al. (2006). It is not clear whether the seasonal variation of secondary microseismic Love waves is as slight as that of Rayleigh waves in this region, but its seasonal observation is crucial for the study of the Love wave generating mechanism.

In the past few years, the emergence of rotational instruments such as ring lasers Schreiber et al. (2014); Igel et al. (2005, 2021) or fibre-optic gyros Schreiber et al. (2009) techniques made it possible to directly measure the rotational ground motion. Previous studies demonstrate the possibility of estimating the microseismic noise source direction based on 6C (three-component translation and three-component rotation) observations Hadziioannou et al. (2012). In addition, the 6C ground motion can naturally separate the microseismic Rayleigh waves into the horizontal rotational components and separate the microseismic Love waves into the vertical rotational component Hadziioannou et al. (2012); Tanimoto et al. (2015, 2016b); Gualtieri et al. (2020); Tang and Fang (2021, 2023); Tang et al. (2024b), thus playing its great advantage of

improving the Love wave source measurements. Therefore, we aim to track the seasonal variation of noise sources combining the 6C ground motion, rather than using the conventional noise source imaging approaches Gerstoft et al. (2006); Gerstoft and Tanimoto (2007); Iyer (1958); Schimmel et al. (2011); Stehly et al. (2006). Improving estimates of microseismic sources through 6C observations can provide more evidence for the current generation mechanism. In particular, it can provide actual observational evidence for the two hypotheses of the generation mechanism of Love waves, and which hypothesis is dominant in a specific area. This allows us to better understand how the coupling and energy exchange between the movement of ocean water and the solid Earth are achieved.

A.2.2 Methods

A.2.2.1 Azimuth estimation of surface waves from a single 6C observation

Previous studies have shown that a single 6C observation can estimate the arrival azimuth of an S-type plane wave Igel et al. (2007); Hadziioannou et al. (2012); Yuan et al. (2021). Theoretically, it is possible to obtain the azimuth of the surface wave by finding the maximum correlation coefficient between the acceleration (m/s^2) and the rotation rate (rad/s) in the azimuth domain. However, from the observation point of view, since the waveform is affected by noise, the azimuth corresponding to the maximum correlation coefficient is not necessarily the correct azimuth. The azimuth can also be estimated by calculating only the change in the sign of the correlation coefficient (see Figures S1-S3). After the coordinate system is defined, a grid search is performed in the azimuth domain. The angle in the middle of the positive correlation coefficient region indicates the propagation direction of the surface wave (see Figure 1a). For a given noise window with N sampling points, the backazimuth

 Ψ of Rayleigh waves can be expressed as:

$$\Omega_T(\psi) = \Omega_E \cos(\psi) - \Omega_N \sin(\psi); \psi \in [0, 2\pi]$$
(A.5)

$$r(\psi) = \frac{\sum_{i=1}^{N} (A_{z_i} - \overline{A_z})(\Omega_{T_i} - \overline{\Omega_T})}{\sqrt{(\sum_{i=1}^{N} (A_{z_i} - \overline{A_z})^2)(\sum_{i=1}^{N} (\Omega_{T_i} - \overline{\Omega_T})^2)}}; min(\frac{\partial r}{\partial \psi}) \mid_{\psi = \psi_1}; max(\frac{\partial r}{\partial \psi}) \mid_{\psi = \psi_0}$$
(A.6)

where ψ is the backazimuth from 0 to 2π . Ω_N and Ω_E represent the rotational rate in the north and east components, respectively. Ω_T represents the rotated horizontal rotational rate at a certain ψ .

$$\begin{cases}
\Psi = (\psi_0 + \psi_1)/2; & \psi_0 <= \psi_1 \\
\Psi = (\psi_0 + \psi_1)/2 - \pi; & \psi_0 > \psi_1, (\psi_0 + \psi_1)/2 > \pi \\
\Psi = (\psi_0 + \psi_1)/2 - \pi; & \psi_0 > \psi_1, (\psi_0 + \psi_1)/2 < \pi
\end{cases} (A.7)$$

r is the classical Pearson correlation coefficient between vertical acceleration A_z and transverse rotation rate Ω_T , while $\overline{A_z}$ and $\overline{\Omega_T}$ are their mean values. ψ_0 and ψ_1 are the maximum and minimum values of the first-order partial derivative of r with respect to ψ , respectively. Ψ is the estimated backazimuth.

For Love waves, Ω_T , Ω_E , Ω_N , and A_z are replaced by A_T (transverse acceleration), $-A_E$ (acceleration in the east component), $-A_N$ (acceleration in the north component), and Ω_z (vertical rotation rate), respectively.

A.2.2.2 Azimuthal seismic anisotropy from 6C amplitude measurements

Our recent papers Tang et al. (2023b,a, 2024b) demonstrate that the amplitude ratio of acceleration to rotation rate or strain rate is equal to the analytical azimuth-dependent phase velocity of the corresponding surface waves Smith and Dahlen (1973). The dispersion equation of the Rayleigh wave from the

amplitude ratio can be expressed as Tang et al. (2023b):

$$\left|\frac{A_{z}(\omega,\psi)}{\Omega_{T}(\omega,\psi)}\right| = c_{R0}(\omega) + \frac{1}{2c_{R0(\omega)}} \left[R_{1}(\omega) + R_{2}(\omega)\cos(2\psi) + R_{3}(\omega)\sin(2\psi) + R_{4}(\omega)\cos(4\psi) + R_{5}(\omega)\sin(4\psi)\right]$$
(A.8)

where $A_z(\omega, \psi)$ is the vertical acceleration and $\Omega_T(\omega, \psi)$ is the transverse rotational velocity. ψ is the backazimuth of the wavenumber vector measured clockwise from the north direction. $c_{R0}(\omega)$ is the phase velocity of the Rayleigh wave for the isotropic medium considered as a reference model. $R_i(\omega)$ (i = 1, 2, 3, 4, 5) are respectively depth integration functions that involve some elastic parameters and eigenfunctions, where we used a simple integration expression derived by montagner1986simple, whose explicit expressions can be found in Equations (2), (4), and (5) of montagner1986simple. Equation (4) provides a method for estimating phase velocities in anisotropic media which only depends on amplitude information.

A.2.3 Data

Considering that broadband rotational seismometers with sufficient sensitivity have not been permanently deployed widely, we select three-component broadband seismometers at Pinon Flat Observatory (PFO) in southern California as the reference 6C station (see Figure 1b) to retrieve rotational ground motions using the ADR approach Spudich et al. (1995); Spudich and Fletcher (2008); Tang et al. (2023a, 2024b). The ambient noise data comes from the PY seismic networks Vernon, F. (2014), IRIS data center. We select 8 three-component stations (see Figure 1b) and use four-year ambient noise data from January 2016 to January 2020 to investigate the seasonal variation of microseismic noise sources. In the following air-pressure data analysis, we use the co-located pressure station near the PY.BPH03 station (see Figure 1b). Figure 1b shows the geometry of seismic stations and the black triangles are the distributions of 3C stations, where the aperture of the seismic array is about 500m. The period range of wavefield gradients from the virtual 6C station is about 3-50s Donner et al. (2017), allowing the retrieval of rotational motions from two

dominant microseismic noise data (5-10s: Secondary microseismic noise. 10-20s: Primary microseismic noise). We calculate the azimuth of the microseismic noise source with a 10s moving window. The choice of this window is a trade-off between computational effort and result smoothness. A smaller window will increase computational effort and impair the correct calculation of waveform cross-correlation, while a larger window will make the result smoother and reduce the angle estimate and time resolution. In each 10s waveform window, we search for its incident azimuth Ψ in the azimuth range of 0-2 π based on Equations (1-3) and estimate the local velocity using the Equation (4). To eliminate the interference of other waves as much as possible, we set a threshold here, that is, when the maximum correlation coefficient r of this time window is larger than 0.8, the waveform of this time window is considered to be the signal of interest, otherwise this window is skipped.

A.2.4 Results

A.2.4.1 Atmospheric pressure effect on array-derived rotational motions

We divide the one-year microseismic data into northern hemisphere winter (September-December and January-February) and summer (March-August) to examine the seasonal variations of microseismic sources. Figure 1c shows the power spectral density (PSD) of the array-derived 6C observations in winter (see Figure S4 for the PSD in summer) at the PFO array, where 'L' means that the Love wave dominate in the microseismic noise data and 'R' indicates Rayleigh waves. The primary microseismic noise (10–20s) marked by 'Pm' and the secondary microseismic noise (5–10s) marked by 'Sm' in Figure 1c can be clearly identified from the PSD of the acceleration (A). In addition, the PSD of three-component rotation shows that the secondary (5-10s) microseismic Rayleigh and Love waves show obvious peaks at 7s in both winter and summer (see Figure 1c and Figure S4). However, compared with the acceleration, the PSDs in the primary microseisms and longer period range show an unfavorable

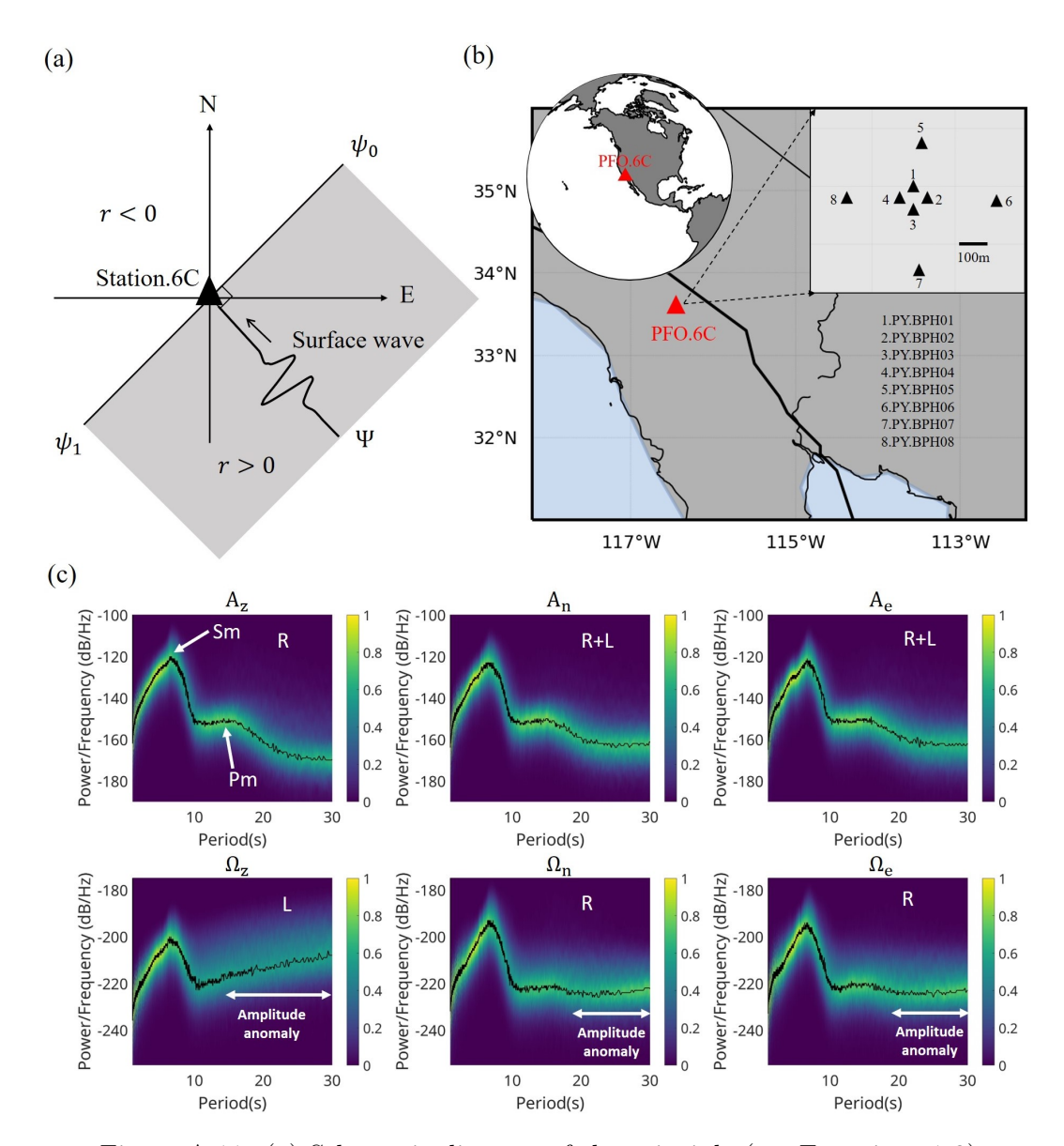


Figure A.11: (a) Schematic diagram of the principle (see Equations 1-3) of azimuth estimation for a single 6C station. r is the Pearson correlation coefficient between vertical acceleration and transverse rotation rate. ψ_0 and ψ_1 are the maximum and minimum values of the first-order partial derivative of r with respect to ψ , respectively. Ψ is the real backazimuth of surface waves. (b) Distributions of selected 8 broadband seismic arrays in the Pinon Flat Observatory. The small array can be regarded as a virtual 6C station. The maximum aperture of this array is about 500m. (c) PSD of 6C microseisms in the winter (2018.September-2018.December and 2018.January-2018.February). The double white arrows indicate the identifiable period range of the amplitude anomaly on PSD. 'R' and 'L' represent the Rayleigh and Love wave, respectively. 'Pm' and 'Sm' represent the primary microseisms and secondary microseisms, respectively.

trend in rotational motions (the amplitude is too large), which is marked by white double arrows in Figure 1c. Theoretically, the PSDs of rotational motions should have similar patterns as the acceleration. For Rayleigh waves recorded in horizontal rotational components, its PSD is mainly contaminated above 20s (see Ω_n and Ω_e in Figure 1c). Therefore, the peak of the primary microseismic Rayleigh wave (10-20s) is still visible, and the summer value is relatively weak (see Figure S4). Compared with Rayleigh waves, the PSD of Love waves in the vertical rotation component is more seriously contaminated starting from 15s (see Figure 1c), making it difficult to distinguish the primary microseismic Love waves.

In theory, the lateral heterogeneity within the seismic array can also lead to amplitude anomalies when using the ADR method. Considering that the PFO region is relatively homogeneous and the wavelength (>15km) of microseismic noises is much larger than the aperture size (about 0.5km) of the PFO array, indicates that the heterogeneity effect probably is not the main reason. It has been demonstrated that the ambient seismic noise at periods of 20-100s is mostly generated by wind-related surface pressure change when surface pressure is large Tanimoto and Wang (2021). To investigate whether the rotation amplitude anomalies are related to the pressure-induced ground deformation, we filter the seismic noise and pressure data to a given frequency range and compare their PSDs. Figure 2a shows the scatter density plot (each data point represents the PSD of one-hour time window) of the PSD calculated using two months data (June to July 2018) in the period range of 10–20s. It shows that the coherence between acceleration and pressure is smaller than 0.1 (see Figure 2a), indicating the acceleration of primary microseisms is less affected by the air pressure-induced noise.

In contrast, the rotational motions of 10-20s are highly related to the pressure data, especially the Love wave (see Figure 2a and 2b) in the vertical rotational motion, whose coherence is larger than 0.6, implying that the three-components rotation is more sensitive to pressure-induced ground deformation than translations. As shown in Figure 2b, the small coherence between acceleration and

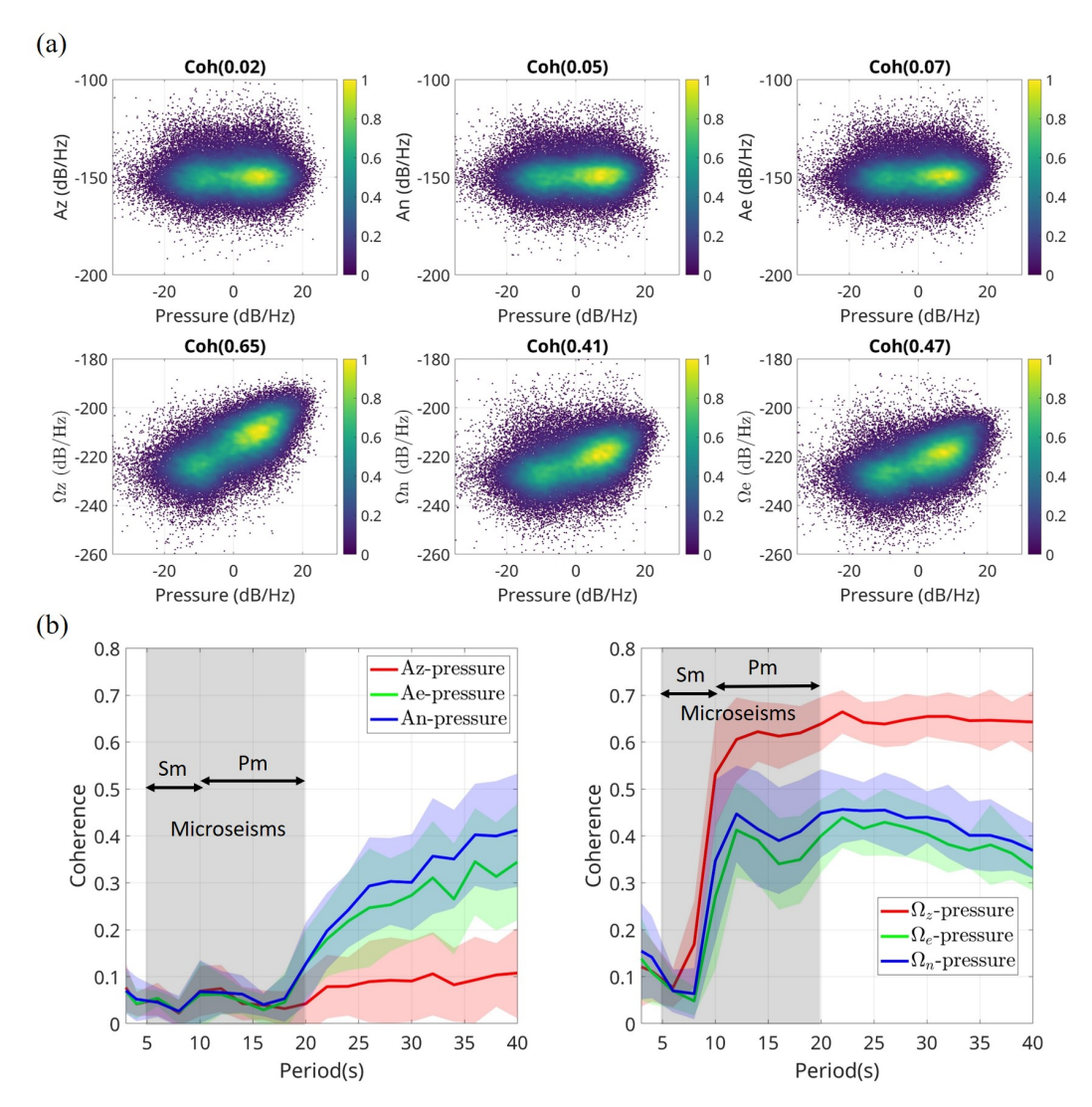


Figure A.12: Air pressure effect on the amplitude of microseisms. (a) The scatter density spectra between the pressure PSD (dB/Hz) and the seismic noise PSD (dB/Hz) of two months data (2018.June-2018.July) in the period range of 10-20s. The coherence (Coh<0.1) between pressure and acceleration (A) is much smaller than the coherence (Coh>0.4) between pressure and rotational rate (Ω). (b) Coherence comparison between acceleration-pressure (left panel) and rotation-pressure (right panel) in different periods (3-40s). In the left panel, red, green, and blue lines represent the vertical, east, and north acceleration components, respectively. In the right panel, red, green, and blue lines represent the vertical, east, and north rotational components, respectively. 'Sm' and 'Pm' with arrows represent the period range of the secondary microseismic noise and the primary microseismic noise.

pressure suggests that the pressure effect on acceleration can be negligible in the two dominant microseismic noise range. However, the rotational component is significantly affected for periods longer than 10s (Figure 2b), indicating that the PSD anomaly on rotations is highly related to the atmospheric pressure. It suggests that the rotational motion of secondary microseisms is more reliable, whereas the results of primary microseisms must be carefully evaluated when estimating the direction of the noise source.

A.2.4.2 Seasonal azimuth variation of microseismic sources

Figures 3(a-d) shows the backazimuth density spectrum of microseismic noise sources estimated by Equations (1-3) from January 2016 to January 2020. As shown in Figure 3a, the secondary microseismic Rayleigh waves are mostly distributed between 200 and 250 degrees, while the winter noise source is slightly shifted to the northwest direction, and has an obvious seasonal cycle. Although a high correlation coefficient threshold (see the Data section) is set to evaluate each time window when estimating the noise azimuth, the error caused by the overlap of noise sources cannot be completely eliminated. Compared with the slight seasonal variation of the secondary microseismic Rayleigh wave in Figure 3a, the seasonal variation of the secondary microseismic Love wave (Figure 3b) is obvious. It is mainly distributed between 275-315 degrees in winter and between 210-270 degrees in summer. In addition, there is also some energy in the azimuth range of 120-180 degrees (Figure 3b), which indicates that secondary Love waves have few noise sources coming from this direction.

As illustrated in Figure 2b, the amplitude of the primary microseisms seems to be severely contaminated by atmospheric pressure-induced ground deformation, especially Love waves. It is worth investigating how the pressure-induced ground deformation affects the backazimuth estimation. The coherence of the primary microseismic Rayleigh wave is below 0.5, probably can lead to a reliable solution. Therefore, we also filter the seismic noise data to 10–20s and calculate the backazimuth using Equations (1–3) with the same moving time window. Figure 3c shows that the primary microseismic Rayleigh waves

(10–20s) have strong seasonal backazimuth variations, while the winter noise mainly comes from two dominant directions, 0–45 and 270–350 degrees, and the summer noise is around 200–270 degrees, which is in agreement with the results by stehly2006study. The primary Love wave in Figure 3d shows a complex noise distribution, which appears in almost all backazimuths. It indicates that the main source comes from around 300-350 degrees, and there is also a recognizable energy cycle at around 135 degrees, and slight seasonal changes are visible.

However, this can be an error affected by atmospheric pressure because of the contamination of the primary Love wave (see Figure 1c and Figure 2b).

A.2.5 Discussion

A.2.5.1 Local seismic anisotropy by seasonal azimuth variations

As shown in Equation (4), a single 6C observation enables estimating the local seismic anisotropy by employing the azimuth-dependent amplitude ratio between acceleration and rotation Tang et al. (2023b,a, 2024b). Therefore, the obvious seasonal variation of microseisms in Figures 3(a-d) makes it possible to extract the azimuth-dependent seismic phase velocity to constrain the Earth's anisotropy. Considering that the amplitude of the primary microseismic surface waves is contaminated by pressure-induced ground deformation (see Figure 1c and Figure 2), and the Love wave is easily contaminated by coupled waves in general anisotropic media Tang et al. (2023b), we aim to measure the phase velocity of secondary microseismic Rayleigh waves. The black data points in Figures 3(e-f) represent the daily backazimuth and phase velocity changes. Their mean value (red line: backazimuth, blue line: velocity) obtained by a three-month time window shows consistent seasonal disturbances. This indicates that the observed velocity changes in Figure 3f are probably associated with the noise source change in Figure 3e. Although seasonal temperature changes Richter et al. (2014) and fluctuations in groundwater levels Mao et al. (2022) can also lead to velocity variations, these factors appear insufficient to

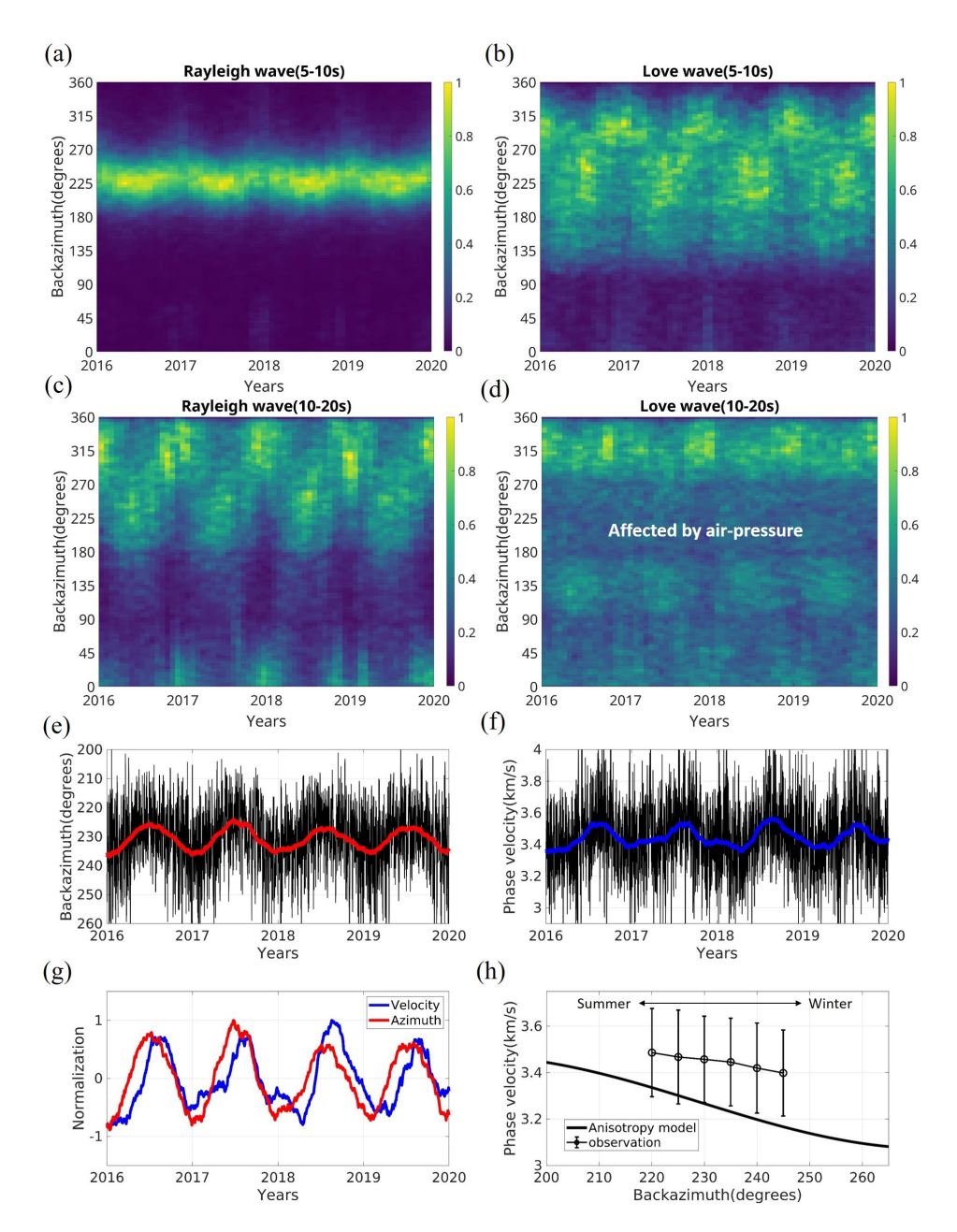


Figure A.13: Seasonal variations in microseismic backazimuth and velocity from 2016 to 2020 using the array-derived 6C observation. (a) and (b) represent the seasonal backazimuth variation of the secondary microseismic Rayleigh and Love wave (5-10s), respectively. (c) and (d) represent the seasonal backazimuth variation of the primary microseismic Rayleigh and Love wave (10-20s), respectively. (e) and (f) represent the backazimuth and phase velocity of secondary microseismic Rayleigh wave (5-10s), respectively, where the black data points are obtained by using Equations (1-4) with a one-day smoothing window. Here we only keep the backazimuth between 200 and 260 degrees and velocity between 2.8 and 4.0 km/s. The red and blue lines in (e-g) are the smoothing result using the black data points with a three-month time moving window. (h) The anisotropy model is obtained by tang2024seismic using the 6C cross-correlation method. The observation data represents the phase velocity variation with a 10 degrees smoothing window based on the black data points of (e-f).

explain the velocity fluctuations of about 0.4 km/s in the upper crust. To better illustrate that the seasonality of seismic velocity is related to azimuths, we compare the estimated velocity with the local anisotropy model of the Rayleigh waves (5-10s), which is obtained by the cross-correlation function method Tang et al. (2024b). The observed results (see Figure 3h) show that the azimuth is smaller and the phase velocity is larger in summer, while the opposite is true in winter, and the trend is consistent with the azimuth anisotropy model (black line in Figure 3h). Although the extracted velocities deviate from the model and have large uncertainties, the local strong anisotropy Tang et al. (2024b) can explain the velocity variation of about 0.3 km/s in the small azimuth range of 220-250 degrees. Consequently, the seasonal change in velocity is mainly due to the azimuthal anisotropy caused by the change in the azimuth of the noise source, providing information on the anisotropy of the upper crust.

A.2.5.2 Origin of microseismic Rayleigh and Love wave sources

We compare our results with those of a relatively large array-based beamforming approach Juretzek and Hadziioannou (2016), where the aperture size of the selected seismic array is about 180km (see Figures S5-S7) and project the dominant backazimuth of the noise sources for both approaches in the global map shown in Figure 4 (see Figures S5-S7 for the detailed beamforming results). As illustrated in Figure 4, the dominant primary and secondary microseismic Rayleigh waves are consistent with the results from the "classic" array-beamforming methods. It demonstrates the reliability of the 6C method and suggests that the effects of atmospheric pressure can be neglected when estimating seasonal Rayleigh wave sources. The generation mechanism of the secondary microseismic Rayleigh waves at a backazimuth of about 200-250 degrees (Figure 4a) in southern California has been supported by simulations and observations over a certain period of time. It is mainly generated by the continuous interaction of two opposite swells about 2000km west of southern California Obrebski et al. (2012), which exerts strong second-order pressure on the seafloor (the black pentagram in Figure 4a and Figure 4e indicates

the approximate source position). The generation of primary microseisms is due to the direct interaction between ocean waves in shallow waters and the seafloor Ardhuin et al. (2011, 2015, 2019); Fukao et al. (2010); Saito (2010), and is therefore strongly related to the seasonal changes in global ocean waves Colosi et al. (2021). It indicates that the primary microseismic Rayleigh waves mainly come from three directions (Figure 4b), among which the sources around 4-45 degrees are generated by the interaction between Atlantic ocean waves and its nearby seafloor, and the sources around 220-270 degrees and 280-350 degrees are excited by the interaction between the Pacific ocean waves and the seafloor of the western north American plate Stehly et al. (2006). Although the primary microseismic Love wave is inevitably affected by the air pressure (see Figure 2b), its source region (around 290-340 degrees in Figure 4d) seems to be similar to the results (around 290-335 degrees in Figure 4h) of the beamforming method in winter. However, it is difficult to compare the 6C results in summer with the beamforming results because the low energy (Figure 3d) and strong atmospheric pressure effect (Figure 2b) make it unreliable.

As shown in Figures 4c and 4g, the backazimuth of secondary microseismic Love wave source from 6C method and beamforming method is consistent, but they differ slightly in summer. However, the result of the beamforming method (see Figure S6) shows that there are stable sources coming from 110-150 degrees in both winter and summer (grey zone in Figure 4g). Although there is also some energy around 120-180 degrees from the 6C method (see Figure 3b), we cannot simply explain this phenomenon and more observations are needed. The generation mechanism of secondary microseismic Love waves has always been controversial. Previous studies Rind and Down (1979); Gualtieri et al. (2020); Le Pape et al. (2021) have shown that it can be generated by the horizontal force split from the interaction between the second-order pressure of waves in any sea area and the inclined seabed, or it can be converted in a heterogeneous medium Ziane and Hadziioannou (2019). Both hypotheses can explain the secondary microseismic Love waves around 210-270 degrees in summer (Figure 4c), because there is a large number of Rayleigh wave sources at around 200-250 degrees (see Figure 4a), which can produce scattering and

conversion. However, a considerable number of secondary microseismic Love wave sources are observed around 275-315 degrees, and it seems difficult to convert the Rayleigh wave sources around 220-270 degrees into Love wave sources in winter. The possible reason is that the strong ocean waves from the north Pacific in winter Colosi et al. (2021) and the ocean waves reflected from the coast generate pressure, which interacts with the inclined seabed near the coast, and the split horizontal force promotes the generation of Love waves. However, these observations and hypotheses need to be combined with accurate velocity models and ocean wave action models (e.g. Wavewatch III Tolman et al. (2009)) to provide more evidence by simulating the complex interaction between ocean waves and the solid Earth Gualtieri et al. (2020). Besides, in further studies, we need to deploy more seismic arrays or available rotational seismometers to accurately locate the source region.

A.2.6 Conclusion

We observe for the first time the seasonal angular variation of the microseismic noise source through the 6C ground motion, which specifically allows us to track the secondary microseismic Love wave. Since rotational motion can automatically distinguish Love waves, it is crucial to estimate the source of Love waves and study their generation mechanism. A single 6C seismic station or a relatively small array can offer improved angular resolution for estimating microseismic sources. This advancement presents a new observational technology for future studies of microseismic source mechanisms in various regions worldwide, particularly in isolated islands in the ocean. We find that the azimuth of the microseismic source remains relatively stable over the four-year time series near the southern California region and secondary Rayleigh waves consistently produce stable microseismic signals at an azimuth of approximately 225 degrees. This stability makes them suitable as a fixed source to study some physical parameters (e.g. anisotropy) of the Earth. The significant difference between secondary microseismic Rayleigh waves and Love waves indicates that ocean bathymetry may dominate this region's generation of Love waves. In

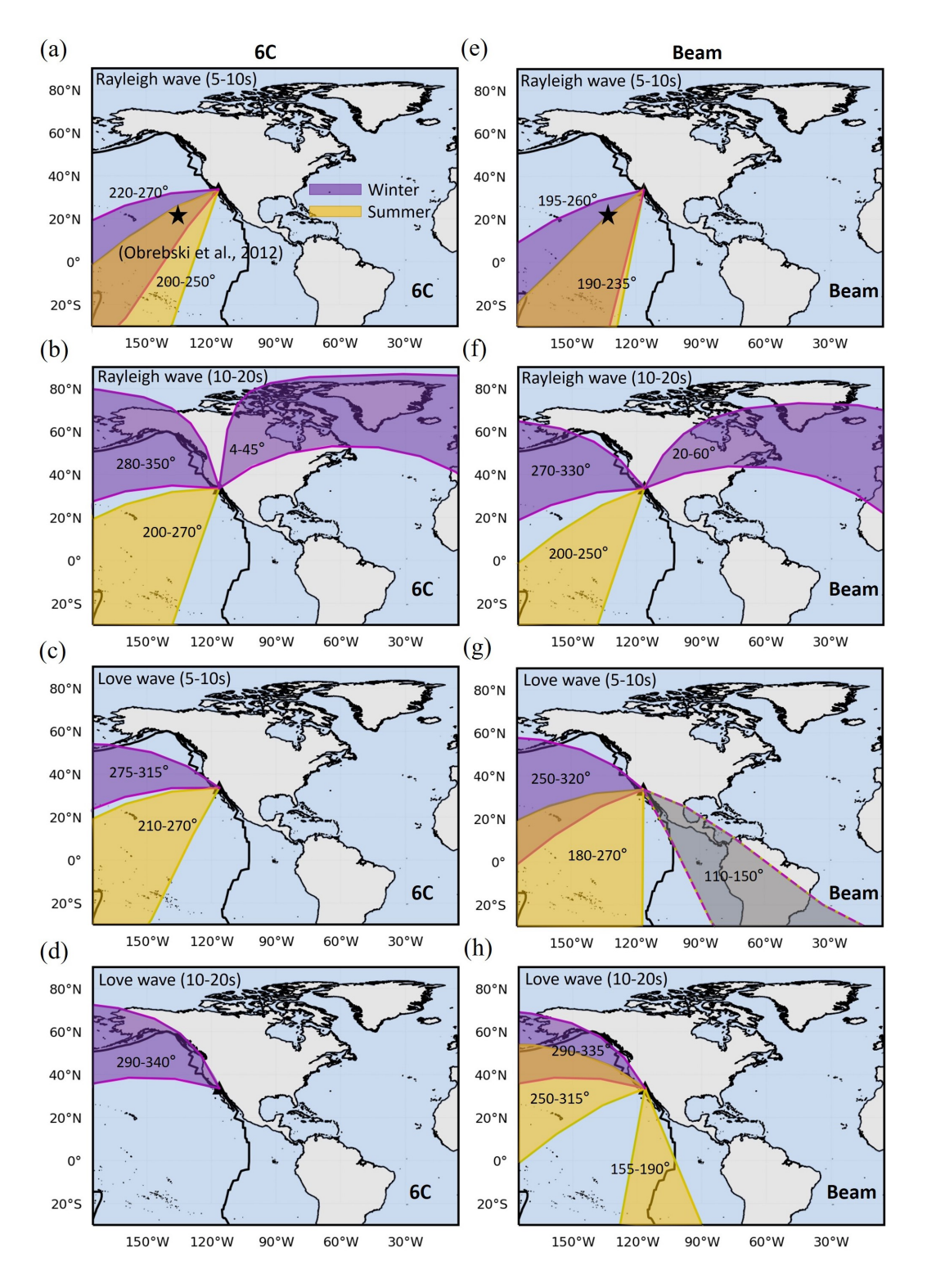


Figure A.14: Projection of dominant microseismic noise sources in 2016-2017. (a-d) represent the noise source estimated using the 6C method based on the PFO.6C array. (e-h) represent the noise source estimated using the beamforming method based on a large seismic array (see Figures S5-S7, the aperture is about 180km). The yellow and purple shaded zones represent the noise source projections in summer and winter, respectively. The grey shaded zone in (g) indicates the overlap of the yellow and purple shaded zones. The black pentagram in Figure 4a and Figure 4e indicates the location of the main secondary microseismic Rayleigh wave source obtained by combining observations and numerical simulations Obrebski et al. (2012).

132

contrast, the contribution of seismic wave conversion only accounts for a small proportion. Additionally, our findings indicate that the rotational motion, or wavefield gradient, estimated by the regional array is more sensitive to ground deformation caused by atmospheric pressure than the translational component for periods longer than 10 seconds. While this sensitivity impacts the estimation of the source of the primary microseisms, it could enhance the connection between observations from different systems on Earth.

Acknowledgments

This work is funded by the European Union's Horizon 2020 research and innovation program under the Marie Skłodowska-Curie grant agreement No 955515 (www.spin-itn.eu). Heiner Igel is grateful for the Cecil and Ida Green visiting scholarship at the Institute of Geophysics and Planetary Physics of the University of Southern California at La Jolla in 2022 and 2023. The authors are grateful to Christoph Schröer for some initial beamforming analysis. We thank the editor Dr. Germán Prieto, one anonymous associate editor and two anonymous reviewers for their constructive comments that help us improve the manuscript.

Open Research

The ambient noise data for the 6C method is publicly available and accessed from the PY network Vernon, F. (2014), where the three-component stations are PY.BPH01, PY.BPH02, PY.BPH03, PY.BPH04 PY.BPH05 PY.BPH06, PY.BPH07, and PY.BPH08. The ambient noise data for the beamforming appproach is publicly available and accessed from the AZ Vernon, F. (1982), CI California Institute of Technology and United States Geological Survey Pasadena (1926) and PY Vernon, F. (2014) networks. The array-derived rotation (ADR) code and noise source estimation code are available from tangle0129₂024₁3832770.

References

- Aki, K. and Richards, P. G. (2002). *Quantitative seismology*. University Science Books.
- Ardhuin, F. (2018). Large-scale forces under surface gravity waves at a wavy bottom: A mechanism for the generation of primary microseisms. *Geophysical Research Letters*, 45(16):8173–8181.
- Ardhuin, F., Gualtieri, L., and Stutzmann, E. (2015). How ocean waves rock the earth: Two mechanisms explain microseisms with periods 3 to 300 s. *Geophysical Research Letters*, 42(3):765–772.
- Ardhuin, F., Gualtieri, L., Stutzmann, E., Nakata, N., and Fichtner, A. (2019). Physics of ambient noise generation by ocean waves. *Seismic ambient noise*, pages 69–108.
- Ardhuin, F., Stutzmann, E., Schimmel, M., and Mangeney, A. (2011). Ocean wave sources of seismic noise. *Journal of Geophysical Research: Oceans*, 116(C9).
- Baggeroer, A. B., Kuperman, W. A., and Schmidt, H. (1988). Matched field processing: Source localization in correlated noise as an optimum parameter estimation problem. J. Acoust. Soc. Am., 83(2):571–587.
- Bensen, G., Ritzwoller, M., Barmin, M., Levshin, A. L., Lin, F., Moschetti, M., Shapiro, N., and Yang, Y. (2007). Processing seismic ambient noise data to obtain reliable broad-band surface wave dispersion measurements. Geophysical journal international, 169(3):1239–1260.

- Bernard, P. (1990). Historical sketch of microseisms from past to future. *Physics* of the earth and planetary interiors, 63(3-4):145–150.
- Bernauer, F., Wassermann, J., and Igel, H. (2012). Rotational sensors—a comparison of different sensor types. *Journal of seismology*, 16:595–602.
- Bodin, P., Gomberg, J., Singh, S., and Santoyo, M. (1997). Dynamic deformations of shallow sediments in the valley of mexico, part i: Three-dimensional strains and rotations recorded on a seismic array. *Bulletin of the Seismological Society of America*, 87(3):528–539.
- Bonnefoy-Claudet, S., Cotton, F., and Bard, P.-Y. (2006). The nature of noise wavefield and its applications for site effects studies: A literature review. *Earth-Science Reviews*, 79(3-4):205–227.
- Brenguier, F., Campillo, M., Hadziioannou, C., Shapiro, N. M., Nadeau, R. M., and Larose, E. (2008). Postseismic relaxation along the San Andreas fault at Parkfield from continuous seismological observations. *science*, 321(5895):1478–1481.
- Bromirski, P. D. and Duennebier, F. K. (2002). The near-coastal microseism spectrum: Spatial and temporal wave climate relationships. *Journal of Geophysical Research: Solid Earth*, 107(B8):ESE–5.
- Bruland, C. and Hadziioannou, C. (2023). Gliding tremors associated with the 26 second microseism in the Gulf of Guinea. *Communications Earth & Environment*, 4(1):1–9.
- California Institute of Technology and United States Geological Survey Pasadena (1926). Southern california seismic network.
- Campillo, M. (2006). Phase and correlation in random's eismic fields and the reconstruction of the green function. *Pure and applied geophysics*, 163:475–502.
- Campillo, M. and Paul, A. (2003). Long-range correlations in the diffuse seismic coda. *Science*, 299(5606):547–549.

- Capon, J. (1969). High-resolution frequency-wavenumber spectrum analysis. *Proceedings of the IEEE*, 57(8):1408–1418.
- Cessaro, R. K. (1994). Sources of primary and secondary microseisms. *Bulletin* of the Seismological Society of America, 84(1):142–148.
- Chevrot, S., Sylvander, M., Benahmed, S., Ponsolles, C., Lefèvre, J., and Paradis, D. (2007). Source locations of secondary microseisms in western europe: Evidence for both coastal and pelagic sources. *Journal of Geophysical Research: Solid Earth*, 112(B11).
- Claerbout, J. F. (1968). Synthesis of a layered medium from its acoustic transmission response. *Geophysics*, 33(2):264–269.
- Clarke, D., Zaccarelli, L., Shapiro, N., and Brenguier, F. (2011). Assessment of resolution and accuracy of the moving window cross spectral technique for monitoring crustal temporal variations using ambient seismic noise. *Geophysical Journal International*, 186(2):867–882.
- Colombi, A., Chaput, J., Brenguier, F., Hillers, G., Roux, P., and Campillo, M. (2014). On the temporal stability of the coda of ambient noise correlations. Comptes Rendus. Géoscience, 346(11-12):307–316.
- Colosi, L. V., Villas Bôas, A. B., and Gille, S. T. (2021). The seasonal cycle of significant wave height in the ocean: Local versus remote forcing. *Journal of Geophysical Research: Oceans*, 126(8):e2021JC017198.
- Davy, C., Stutzmann, E., Barruol, G., Fontaine, F. R., and Schimmel, M. (2015). Sources of secondary microseisms in the indian ocean. *Geophysical Journal International*, 202(2):1180–1189.
- Delaney, E., Ermert, L., Sager, K., Kritski, A., Bussat, S., and Fichtner, A. (2017). Passive seismic monitoring with nonstationary noise sources. *Geophysics*, 82(4):KS57–KS70.
- Derode, A., Larose, E., Tanter, M., De Rosny, J., Tourin, A., Campillo, M., and Fink, M. (2003). Recovering the Green's function from field-field correlations in an open scattering medium (L). J. Acoust. Soc. Am., 113(6):2973–2976.

- Dewdney, P. E., Hall, P. J., Schilizzi, R. T., and Lazio, T. J. L. (2009). The square kilometre array. *Proceedings of the IEEE*, 97(8):1482–1496.
- Donaldson, C., Caudron, C., Green, R. G., Thelen, W. A., and White, R. S. (2017). Relative seismic velocity variations correlate with deformation at Kīlauea volcano. *Sci. Adv.*, 3(6):e1700219.
- Donner, S., Lin, C.-J., Hadziioannou, C., Gebauer, A., Vernon, F., Agnew, D. C., Igel, H., Schreiber, U., and Wassermann, J. (2017). Comparing direct observation of strain, rotation, and displacement with array estimates at piñon flat observatory, california. Seismological Research Letters, 88(4):1107–1116.
- Ebeling, C. W. (2012). Inferring ocean storm characteristics from ambient seismic noise: A historical perspective. In *Advances in geophysics*, volume 53, pages 1–33. Elsevier.
- Essen, H.-H., Krüger, F., Dahm, T., and Grevemeyer, I. (2003). On the generation of secondary microseisms observed in northern and central europe. *Journal of Geophysical Research: Solid Earth*, 108(B10).
- Federal Institute for Geosciences and Natural Resources (1976). German Regional Seismic Network (GRSN).
- Federal Institute for Geosciences and Natural Resources (BGR), Germany (1976). German Regional Seismic Network (GRSN).
- Fichtner, A., Bowden, D., and Ermert, L. (2020). Optimal processing for seismic noise correlations. *Geophysical Journal International*, 223(3):1548–1564.
- Friedrich, A., Krüger, F., and Klinge, K. (1998). Ocean-generated microseismic noise located with the gräfenberg array. *Journal of seismology*, 2:47–64.
- Friedrich, T., Zieger, T., Forbriger, T., and Ritter, J. R. R. (2018). Locating wind farms by seismic interferometry and migration. *Journal of Seismology*, 22(6):1469–1483.

- Froment, B., Campillo, M., Roux, P., Gouedard, P., Verdel, A., and Weaver, R. L. (2010). Estimation of the effect of nonisotropically distributed energy on the apparent arrival time in correlations. *Geophysics*, 75(5):SA85–SA93.
- Fukao, Y., Nishida, K., and Kobayashi, N. (2010). Seafloor topography, ocean infragravity waves, and background love and rayleigh waves. *Journal of Geophysical Research: Solid Earth*, 115(B4).
- Gal, M., Reading, A., Ellingsen, S., Koper, K., and Burlacu, R. (2017). Full wavefield decomposition of high-frequency secondary microseisms reveals distinct arrival azimuths for rayleigh and love waves. *Journal of Geophysical Research: Solid Earth*, 122(6):4660–4675.
- Gal, M., Reading, A. M., Nakata, N., Gualtieri, L., and Fichtner, A. (2019). Beamforming and polarization analysis. *Seismic ambient noise*, pages 32–72.
- Gerstoft, P., Fehler, M. C., and Sabra, K. G. (2006). When katrina hit california. Geophysical Research Letters, 33(17).
- Gerstoft, P., Shearer, P. M., Harmon, N., and Zhang, J. (2008). Global P, PP, and PKP Wave Microseisms Observed from Distant Storms. *Geophys. Res. Lett.*, 35(23).
- Gerstoft, P. and Tanimoto, T. (2007). A year of microseisms in southern california. *Geophysical Research Letters*, 34(20).
- Goldstein, P. and Snoke, A. (2005). Sac availability for the iris community. IRIS Newsletter, 15(2):1–6.
- Gouédard, P., Stehly, L., Brenguier, F., Campillo, M., Colin de Verdière, Y., Larose, E., Margerin, L., Roux, P., Sánchez-Sesma, F. J., Shapiro, N. M., and Weaver, R. L. (2008). Cross-correlation of random fields: Mathematical approach and applications. *Geophysical Prospecting*, 56(3):375–393.
- Grob, M., Maggi, A., and Stutzmann, E. (2011). Observations of the seasonality of the antarctic microseismic signal, and its association to sea ice variability. *Geophysical Research Letters*, 38(11).

- Groos, J. and Ritter, J. (2009). Time domain classification and quantification of seismic noise in an urban environment. *Geophysical Journal International*, 179(2):1213–1231.
- Gualtieri, L., Bachmann, E., Simons, F., and Tromp, J. (2021a). Generation of secondary microseism Love waves: effects of bathymetry, 3-D structure and source seasonality. *Geophys. J. Int.*, 226(1):192–219.
- Gualtieri, L., Bachmann, E., Simons, F. J., and Tromp, J. (2020). The origin of secondary microseism love waves. *Proceedings of the National Academy of Sciences*, 117(47):29504–29511.
- Gualtieri, L., Bachmann, E., Simons, F. J., and Tromp, J. (2021b). Generation of secondary microseism love waves: Effects of bathymetry, 3-d structure and source seasonality. *Geophysical Journal International*, 226(1):192–219.
- Gualtieri, L., Stutzmann, E., Juretzek, C., Hadziioannou, C., and Ardhuin, F. (2019). Global scale analysis and modelling of primary microseisms. Geophysical Journal International, 218(1):560–572.
- Guillemot, A., van Herwijnen, A., Larose, E., Mayer, S., and Baillet, L. (2021).
 Effect of Snowfall on Changes in Relative Seismic Velocity Measured by
 Ambient Noise Correlation. The Cryosphere, 15(12):5805–5817.
- Gutenberg, B. (1936). On microseisms. Bulletin of the Seismological Society of America, 26(2):111–117.
- Gutenberg, B. (1958). Two types of microseisms. *Journal of Geophysical Research*, 63(3):595–597.
- Hadziioannou, C., Gaebler, P., Schreiber, U., Wassermann, J., and Igel, H. (2012). Examining ambient noise using colocated measurements of rotational and translational motion. *Journal of seismology*, 16:787–796.
- Hadziioannou, C., Larose, E., Baig, A., Roux, P., and Campillo, M. (2011). Improving temporal resolution in ambient noise monitoring of seismic wave speed. J. Geophys. Res., 116(B7).

- Hadziioannou, C., Larose, E., Coutant, O., Roux, P., and Campillo, M. (2009).
 Stability of monitoring weak changes in multiply scattering media with ambient noise correlation: Laboratory experiments. J. Acoust. Soc. Am., 125(6):3688–3695.
- Harris, C. R., Millman, K. J., van der Walt, S. J., Gommers, R., Virtanen, P., Cournapeau, D., Wieser, E., Taylor, J., Berg, S., Smith, N. J., Kern, R., Picus, M., Hoyer, S., van Kerkwijk, M. H., Brett, M., Haldane, A., del Río, J. F., Wiebe, M., Peterson, P., Gérard-Marchant, P., Sheppard, K., Reddy, T., Weckesser, W., Abbasi, H., Gohlke, C., and Oliphant, T. E. (2020). Array programming with NumPy. Nature, 585(7825):357–362.
- Hasselmann, K. (1963). A statistical analysis of the generation of microseisms. Reviews of Geophysics, 1(2):177–210.
- Haubrich, R. A. (1965). Earth noise, 5 to 500 millicycles per second: 1. spectral stationarity, normality, and nonlinearity. *Journal of Geophysical Research*, 70(6):1415–1427.
- Haubrich, R. A. and McCamy, K. (1969). Microseisms: Coastal and pelagic sources. *Reviews of Geophysics*, 7(3):539–571.
- Hillers, G., Ben-Zion, Y., Campillo, M., and Zigone, D. (2015). Seasonal Variations of Seismic Velocities in the San Jacinto Fault Area Observed with Ambient Seismic Noise. *Geophys. J. Int.*, 202(2):920–932.
- Hillers, G., Graham, N., Campillo, M., Kedar, S., Landès, M., and Shapiro, N. (2012). Global oceanic microseism sources as seen by seismic arrays and predicted by wave action models. *Geochemistry, Geophysics, Geosystems*, 13(1).
- Huang, B.-S. (2003). Ground rotational motions of the 1999 chi-chi, taiwan earthquake as inferred from dense array observations. *Geophysical Research Letters*, 30(6).
- Hunter, J. D. (2007). Matplotlib: A 2D graphics environment. Computing in Science & Engineering, 9(3):90–95.

- Igel, H., Cochard, A., Wassermann, J., Flaws, A., Schreiber, U., Velikoseltsev, A., and Pham Dinh, N. (2007). Broad-band observations of earthquakeinduced rotational ground motions. *Geophysical Journal International*, 168(1):182–196.
- Igel, H., Nader, M.-F., Kurrle, D., Ferreira, A. M., Wassermann, J., and Schreiber, K. U. (2011). Observations of earth's toroidal free oscillations with a rotation sensor: The 2011 magnitude 9.0 tohoku-oki earthquake. Geophysical Research Letters, 38(21).
- Igel, H., Schreiber, K. U., Gebauer, A., Bernauer, F., Egdorf, S., Simonelli, A., Liny, C.-J., Wassermann, J., Donner, S., Hadziioannou, C., Yuan, S., Brotzer, A., Kodet, J., Tanimoto, T., Hugentobler, U., and R. Wells, J.-P. (2021). Romy: A multi-component ring laser for geodesy and geophysics. Geophysical Journal International.
- Igel, H., Schreiber, U., Flaws, A., Schuberth, B., Velikoseltsev, A., and Cochard, A. (2005). Rotational motions induced by the m8. 1 tokachi-oki earthquake, september 25, 2003. Geophysical research letters, 32(8).
- Igel, J. K. H., Bowden, D. C., and Fichtner, A. (2023). SANS: Publicly Available Daily Multi-Scale Seismic Ambient Noise Source Maps. J. Geophys. Res. Solid Earth, 128(1):e2022JB025114.
- Instituto Português do Mar e da Atmosfera, I.P. (IPMA), Portugal (2006). Portuguese National Seismic Network.
- Istituto Nazionale di Geofisica e Vulcanologia (INGV) (2005). Rete Sismica Nazionale (RSN).
- Istituto Nazionale di Geofisica e Vulcanologia (INGV), Italy (2005). Rete Sismica Nazionale (RSN).
- Iyer, H. (1958). A study on the direction of arrival of microseisms at kew observatory. *Geophysical Journal International*, 1(1):32–43.

- Juretzek, C. and Hadziioannou, C. (2016). Where do ocean microseisms come from? a study of love-to-rayleigh wave ratios. *Journal of Geophysical Research: Solid Earth*, 121(9):6741–6756.
- Juretzek, C. and Hadziioannou, C. (2017). Linking source region and ocean wave parameters with the observed primary microseismic noise. Geophys. J. Int., 211(3):1640–1654.
- Kedar, S., Longuet-Higgins, M., Webb, F., Graham, N., Clayton, R., and Jones, C. (2008). The origin of deep ocean microseisms in the north atlantic ocean. Proceedings of the Royal Society A: Mathematical, Physical and Engineering Sciences, 464(2091):777-793.
- Kislov, K. and Gravirov, V. (2021). Rotational seismology: Review of achievements and outlooks. *Seismic Instruments*, 57:187–202.
- Koper, K. D. and de Foy, B. (2008). Seasonal anisotropy in short-period seismic noise recorded in south asia. Bulletin of the Seismological Society of America, 98(6):3033-3045.
- Krischer, L., Megies, T., Barsch, R., Beyreuther, M., Lecocq, T., Caudron, C., and Wassermann, J. (2015). Obspy: A bridge for seismology into the scientific python ecosystem. Comput. Sci. Discov., 8(1):014003.
- Landès, M., Hubans, F., Shapiro, N. M., Paul, A., and Campillo, M. (2010).
 Origin of deep ocean microseisms by using teleseismic body waves. *Journal of Geophysical Research: Solid Earth*, 115(B5).
- Larose, E., Derode, A., Clorennec, D., Margerin, L., and Campillo, M. (2005).
 Passive retrieval of rayleigh waves in disordered elastic media. *Physical Review E—Statistical, Nonlinear, and Soft Matter Physics*, 72(4):046607.
- Larose, E., Margerin, L., Derode, A., van Tiggelen, B., Campillo, M., Shapiro, N., Paul, A., Stehly, L., and Tanter, M. (2006). Correlation of random wavefields: An interdisciplinary review. *Geophysics*, 71(4):SI11–SI21.

- Le Pape, F., Craig, D., and Bean, C. J. (2021). How deep ocean-land coupling controls the generation of secondary microseism love waves. *Nature Communications*, 12(1):2332.
- Lecocq, T., Longuevergne, L., Pedersen, H. A., Brenguier, F., and Stammler, K. (2017). Monitoring Ground Water Storage at Mesoscale Using Seismic Noise: 30 Years of Continuous Observation and Thermo-Elastic and Hydrological Modeling. Sci. Rep., 7(1):14241.
- Lepore, S. and Grad, M. (2018). Analysis of the primary and secondary microseisms in the wavefield of the ambient noise recorded in northern Poland. *Acta Geophys.*, 66:915–929.
- Lin, C.-J., Huang, H.-P., Pham, N. D., Liu, C.-C., Chi, W.-C., and Lee, W. H. (2011). Rotational motions for teleseismic surface waves. *Geophysical Research Letters*, 38(15).
- Lin, F.-C., Moschetti, M. P., and Ritzwoller, M. H. (2008). Surface wave tomography of the western united states from ambient seismic noise: Rayleigh and love wave phase velocity maps. *Geophysical Journal International*, 173(1):281–298.
- Lindner, F., Wassermann, J., and Igel, H. (2021). Seasonal Freeze-Thaw Cycles and Permafrost Degradation on Mt. Zugspitze (German/Austrian Alps) Revealed by Single-Station Seismic Monitoring. *Geophys. Res. Lett.*, 48(18):e2021GL094659.
- Liu, Z., Huang, J., He, P., and Qi, J. (2018). Ambient Noise Monitoring of Seismic Velocity Around the Longmenshan Fault Zone From 10 Years of Continuous Observation. J. Geophys. Res. Solid Earth, 123(10):8979–8994.
- Lobkis, O. I. and Weaver, R. L. (2001). On the emergence of the green's function in the correlations of a diffuse field. *The Journal of the Acoustical Society of America*, 110(6):3011–3017.
- Lobkis, O. I. and Weaver, R. L. (2003). Coda-Wave Interferometry in Finite

- Solids: Recovery of P -to- S Conversion Rates in an Elastodynamic Billiard. *Phys. Rev. Lett.*, 90(25):254302.
- Longuet-Higgins, M. S. (1950). A theory of the origin of microseisms. *Philosophical Transactions of the Royal Society of London. Series A, Mathematical and Physical Sciences*, 243(857):1–35.
- Lu, Y., Pedersen, H. A., Stehly, L., and AlpArray Working Group (2022). Mapping the Seismic Noise Field in Europe: Spatio-Temporal Variations in Wavefield Composition and Noise Source Contributions. *Geophys. J. Int.*, 228(1):171–192.
- Lu, Y., Stehly, L., Paul, A., and the AlpArray Working Group (2018). High-Resolution Surface Wave Tomography of the European Crust and Uppermost Mantle from Ambient Seismic Noise. Geophys. J. Int., 214(2):1136–1150.
- Maass, R., Schippkus, S., Hadziioannou, C., Schwarz, B., Jousset, P., and Krawczyk, C. (2024). Stacking of Distributed Dynamic Strain Reveals Link Between Seismic Velocity Changes and the 2020 Unrest in Reykjanes. *J. Geophys. Res. Solid Earth*, 129(6):e2023JB028320.
- Mao, S., Lecointre, A., van der Hilst, R. D., and Campillo, M. (2022). Space-Time Monitoring of Groundwater Fluctuations with Passive Seismic Interferometry. *Nature Communications*, 13(1):4643.
- Margerin, L., Planès, T., Mayor, J., and Calvet, M. (2016). Sensitivity kernels for coda-wave interferometry and scattering tomography: Theory and numerical evaluation in two-dimensional anisotropically scattering media. Geophysical Journal International, 204(1):650–666.
- Met Office (2010). Cartopy: A Cartographic Python Library with a Matplotlib Interface. Exeter, Devon.
- Mikesell, T. D., Malcolm, A. E., Yang, D., and Haney, M. M. (2015). A Comparison of Methods to Estimate Seismic Phase Delays: Numerical Examples for Coda Wave Interferometry. *Geophys. J. Int.*, 202(1):347–360.

- Nagel, S., Zieger, T., Luhmann, B., Knödel, P., Ritter, J., and Ummenhofer, T. (2021). Ground motions induced by wind turbines. Civil Engineering Design, 3(3):73–86.
- Nakata, N., Gualtieri, L., and Fichtner, A. (2019). Seismic ambient noise. Cambridge University Press.
- Nishida, K., Kawakatsu, H., Fukao, Y., and Obara, K. (2008). Background love and rayleigh waves simultaneously generated at the pacific ocean floors. *Geophysical Research Letters*, 35(16).
- Obermann, A., Froment, B., Campillo, M., Larose, E., Planès, T., Valette, B., Chen, J. H., and Liu, Q. Y. (2014). Seismic noise correlations to image structural and mechanical changes associated with the Mw 7.9 2008 Wenchuan earthquake. *Journal of Geophysical Research: Solid Earth*, 119(4):3155–3168.
- Obermann, A., Planès, T., Hadziioannou, C., and Campillo, M. (2016). Lapse-Time-Dependent Coda-Wave Depth Sensitivity to Local Velocity Perturbations in 3-D Heterogeneous Elastic Media. *Geophys. J. Int.*, 207(1):59–66.
- Obermann, A., Planès, T., Larose, E., Sens-Schönfelder, C., and Campillo, M. (2013). Depth sensitivity of seismic coda waves to velocity perturbations in an elastic heterogeneous medium. *Geophys. J. Int.*, 194(1):372–382.
- Obrebski, M., Ardhuin, F., Stutzmann, E., and Schimmel, M. (2012). How moderate sea states can generate loud seismic noise in the deep ocean. *Geophysical Research Letters*, 39(11).
- Obrebski, M., Ardhuin, F., Stutzmann, E., and Schimmel, M. (2013). Detection of microseismic compressional (p) body waves aided by numerical modeling of oceanic noise sources. *Journal of Geophysical Research: Solid Earth*, 118(8):4312–4324.
- Pancha, A., Webb, T., Stedman, G., McLeod, D., and Schreiber, K. (2000).
 Ring laser detection of rotations from teleseismic waves. *Geophysical Research Letters*, 27(21):3553–3556.
- Petroff, M. A. (2021). Accessible Color Sequences for Data Visualization.

- Planès, T., Larose, E., Margerin, L., Rossetto, V., and Sens-Schönfelder, C. (2014). Decorrelation and phase-shift of coda waves induced by local changes: Multiple scattering approach and numerical validation. Waves in Random and Complex Media, 24(2):99–125.
- Polish Academy of Sciences (PAN) Polskiej Akademii Nauk (1990). Polish Seismological Network.
- Qin, T. and Lu, L. (2024). Improved beamforming schemes for estimation of multimode surface wave dispersion curves from seismic noise with reducing effect of the irregular array geometry and/or anisotropic source distribution. Geophysical Journal International, 237(1):250–270.
- Reseau sismologique et géodésique français (RESIF), France (1995). Epos-France Broad-band network (RLBP).
- Retailleau, L., Boué, P., Stehly, L., and Campillo, M. (2017). Locating Microseism Sources Using Spurious Arrivals in Intercontinental Noise Correlations.

 Journal of Geophysical Research: Solid Earth, 122(10):8107–8120.
- Retailleau, L. and Gualtieri, L. (2019). Toward high-resolution period-dependent seismic monitoring of tropical cyclones. *Geophysical Research Letters*, 46(3):1329–1337.
- Richter, T., Sens-Schönfelder, C., Kind, R., and Asch, G. (2014). Comprehensive Observation and Modeling of Earthquake and Temperature-Related Seismic Velocity Changes in Northern Chile with Passive Image Interferometry. *J. Geophys. Res. Solid Earth*, 119(6):4747–4765.
- Rind, D. and Down, W. (1979). Microseisms at palisades: 2. rayleigh wave and love wave characteristics and the geologic control of propagation. *Journal of Geophysical Research: Solid Earth*, 84(B10):5632–5642.
- Rost, S. and Thomas, C. (2002). Array seismology: Methods and applications. Reviews of geophysics, 40(3):2–1.

- Roux, P., Sabra, K. G., Kuperman, W. A., and Roux, A. (2005). Ambient noise cross correlation in free space: Theoretical approach. *Journal of the Acoustical Society of America*, 117:79–84.
- Roux, P., Wathelet, M., and Roueff, A. (2011). The San Andreas Fault revisited through seismic-noise and surface-wave tomography. *Geophys. Res. Lett.*, 38(13).
- Ruigrok, E., Gibbons, S., and Wapenaar, K. (2017). Cross-correlation beamforming. *J. Seismol.*, 21:495–508.
- Sabra, K. G., Gerstoft, P., Roux, P., Kuperman, W., and Fehler, M. C. (2005).
 Extracting time-domain green's function estimates from ambient seismic noise. Geophysical research letters, 32(3).
- Safarkhani, M. and Shirzad, T. (2019). Improving c 1 and c 3 empirical green's functions from ambient seismic noise in nw iran using rms ratio stacking method. *Journal of Seismology*, 23:787–799.
- Saito, T. (2010). Love-wave excitation due to the interaction between a propagating ocean wave and the sea-bottom topography. *Geophysical Journal International*, 182(3):1515–1523.
- Schimmel, M., Stutzmann, E., Ardhuin, F., and Gallart, J. (2011). Polarized earth's ambient microseismic noise. *Geochemistry, Geophysics, Geosystems*, 12(7).
- Schippkus, S. (2023). Schipp/repeating direct waves.
- Schippkus, S., Garden, M., and Bokelmann, G. (2020). Characteristics of the Ambient Seismic Field on a Large-N Seismic Array in the Vienna Basin. Seismological Research Letters, 91(5):2803–2816.
- Schippkus, S., Safarkhani, M., and Hadziioannou, C. (2023). Continuous isolated noise sources induce repeating waves in the coda of ambient noise correlations. *Seismica*, 2(2).

- Schippkus, S., Snieder, R., and Hadziioannou, C. (2022). Seismic interferometry in the presence of an isolated noise source. *Seismica*, 1(1).
- Schippkus, S., Zigone, D., Bokelmann, G. H. R., and the AlpArray Working Group (2018). Ambient-Noise Tomography of the Wider Vienna Basin Region. Geophys. J. Int., 215(1):102–117.
- Schreiber, K., Gebauer, A., Igel, H., Wassermann, J., Hurst, R. B., and Wells, J.-P. R. (2014). The centennial of the sagnac experiment in the optical regime: From a tabletop experiment to the variation of the earth's rotation. Comptes Rendus Physique, 15(10):859–865.
- Schreiber, K., Velikoseltsev, A., Carr, A., and Franco-Anaya, R. (2009). The application of fiber optic gyroscopes for the measurement of rotations in structural engineering. *Bulletin of the Seismological Society of America*, 99(2B):1207–1214.
- Schreiber, K. U., Stedman, G. E., Igel, H., and Flaws, A. (2006). Ring laser gyroscopes as rotation sensors for seismic wave studies. *Earthquake source asymmetry, structural media and rotation effects*, pages 377–390.
- Schulte-Pelkum, V., Earle, P. S., and Vernon, F. L. (2004). Strong directivity of ocean-generated seismic noise. *Geochemistry, Geophysics, Geosystems*, 5(3).
- Schweitzer, J., Fyen, J., Mykkeltveit, S., Gibbons, S. J., Pirli, M., Kühn, D., and Kværna, T. (2012). Seismic arrays. In *New manual of seismological observatory practice 2 (NMSOP-2)*, pages 1–80. Deutsches GeoForschungsZentrum GFZ.
- Sens-Schönfelder, C. and Larose, E. (2010). Lunar noise correlation, imaging and monitoring. *Earthquake Science*, 23(5):519–530.
- Sens-Schönfelder, C. and Wegler, U. (2006). Passive image interferometry and seasonal variations of seismic velocities at Merapi Volcano, Indonesia. *Geophys. Res. Lett.*, 33(21).

- Shabtian, H. S., Eilon, Z. C., and Tanimoto, T. (2024). Seasonality of california central coast microseisms. *Bulletin of the Seismological Society of America*, 114(2):873–881.
- Shapiro, N. M. and Campillo, M. (2004). Emergence of broadband rayleigh waves from correlations of the ambient seismic noise. *Geophysical Research Letters*, 31(7).
- Shapiro, N. M., Campillo, M., Stehly, L., and Ritzwoller, M. H. (2005). High-resolution surface-wave tomography from ambient seismic noise. *Science*, 307(5715):1615–1618.
- Shearer, P. M. (2019). Introduction to seismology. Cambridge university press.
- Sheng, Y., Mordret, A., Brenguier, F., Boué, P., Vernon, F., Takeda, T., Aoki, Y., Taira, T., and Ben-Zion, Y. (2023). Seeking Repeating Anthropogenic Seismic Sources: Implications for Seismic Velocity Monitoring at Fault Zones. Journal of Geophysical Research: Solid Earth, 128(1).
- Sheng, Y., Nakata, N., and Beroza, G. C. (2018). On the Nature of Higher-Order Ambient Seismic Field Correlations. *J. Geophys. Res. Solid Earth*, 123(9):7969–7982.
- Shirzad, T., Safarkhani, M., and Assumpção, M. S. (2022). Extracting reliable empirical green's functions using weighted cross-correlation functions of ambient seismic noise in west-central and southern brazil. *Geophysical Journal International*, 230(2):1441–1464.
- Shirzad, T. and Shomali, Z. H. (2014). Shallow crustal radial anisotropy beneath the Tehran basin of Iran from seismic ambient noise tomography. *Phys. Earth Planet. Inter.*, 231:16–29.
- Smith, M. L. and Dahlen, F. (1973). The azimuthal dependence of love and rayleigh wave propagation in a slightly anisotropic medium. *Journal of Geophysical Research*, 78(17):3321–3333.
- Snieder, R. (2004). Extracting the green's function from the correlation of coda waves: A derivation based on stationary phase. *Physical Review E*, 69(4).

- Snieder, R., Grêt, A., Douma, H., and Scales, J. (2002). Coda wave interferometry for estimating nonlinear behavior in seismic velocity. *Science*, 295(5563):2253–2255.
- Snieder, R., Wapenaar, K., and Larner, K. (2006). Spurious multiples in seismic interferometry of primaries. *GEOPHYSICS*, 71(4):SI111–SI124.
- Sodankylä Geophysical Observatory / University Of Oulu, Finland (1980). Northern Finland Seismological Network.
- Soergel, D., Pedersen, H. A., Bodin, T., Paul, A., Stehly, L., and AlpArray Working Group (2023). Bayesian Analysis of Azimuthal Anisotropy in the Alpine Lithosphere from Beamforming of Ambient Noise Cross-Correlations. *Geophys. J. Int.*, 232(1):429–450.
- Sollberger, D., Bradley, N., Edme, P., and Robertsson, J. O. A. (2023). Efficient wave type fingerprinting and filtering by six-component polarization analysis. *Geophysical Journal International*, 234(1):25–39.
- Sollberger, D., Igel, H., Schmelzbach, C., Edme, P., Van Manen, D.-J., Bernauer, F., Yuan, S., Wassermann, J., Schreiber, U., and Robertsson, J. O. (2020). Seismological processing of six degree-of-freedom ground-motion data. Sensors, 20(23):6904.
- Spudich, P. and Fletcher, J. B. (2008). Observation and prediction of dynamic ground strains, tilts, and torsions caused by the m w 6.0 2004 parkfield, california, earthquake and aftershocks, derived from upsar array observations. Bulletin of the Seismological Society of America, 98(4):1898–1914.
- Spudich, P., Steck, L. K., Hellweg, M., Fletcher, J., and Baker, L. M. (1995). Transient stresses at parkfield, california, produced by the m 7.4 landers earthquake of june 28, 1992: Observations from the upsar dense seismograph array. *Journal of Geophysical Research: Solid Earth*, 100(B1):675–690.
- Stehly, L., Campillo, M., Froment, B., and Weaver, R. L. (2008). Reconstructing green's function by correlation of the coda of the correlation (c3) of ambient seismic noise. *Journal of Geophysical Research: Solid Earth*, 113(B11).

- Stehly, L., Campillo, M., and Shapiro, N. (2006). A study of the seismic noise from its long-range correlation properties. *Journal of Geophysical Research:* Solid Earth, 111(B10).
- Stehly, L., Fry, B., Campillo, M., Shapiro, N. M., Guilbert, J., Boschi, L., and Giardini, D. (2009). Tomography of the alpine region from observations of seismic ambient noise. *Geophysical Journal International*, 178(1):338–350.
- Steim, J. (2015). Theory and observations-Instrumentation for global and regional seismology. Elsevier.
- Steinmann, R., Hadziioannou, C., and Larose, E. (2021). Effect of Centimetric Freezing of the near Subsurface on Rayleigh and Love Wave Velocity in Ambient Seismic Noise Correlations. *Geophys. J. Int.*, 224(1):626–636.
- Strollo, A., Cambaz, D., Clinton, J., Danecek, P., Evangelidis, C. P., Marmureanu, A., Ottemöller, L., Pedersen, H., Sleeman, R., Stammler, K., et al. (2021). Eida: The european integrated data archive and service infrastructure within orfeus. Seismol. Res. Lett., 92(3):1788–1795.
- Stutzmann, E., Ardhuin, F., Schimmel, M., Mangeney, A., and Patau, G. (2012).

 Modelling long-term seismic noise in various environments. *Geophysical Journal International*, 191(2):707–722.
- Stutzmann, E., Schimmel, M., Patau, G., and Maggi, A. (2009). Global climate imprint on seismic noise. *Geochemistry, Geophysics, Geosystems*, 10(11).
- Suryanto, W., Igel, H., Wassermann, J., Cochard, A., Schuberth, B., Vollmer, D., Scherbaum, F., Schreiber, U., and Velikoseltsev, A. (2006). First comparison of array-derived rotational ground motions with direct ring laser measurements. Bulletin of the Seismological Society of America, 96(6):2059–2071.
- Takeo, M. (1998). Ground rotational motions recorded in near-source region of earthquakes. *Geophysical Research Letters*, 25(6):789–792.
- Tang, L. and Fang, X. (2021). Generation of 6-c synthetic seismograms in stratified vertically transversely isotropic media using a generalized reflection

- and transmission coefficient method. Geophysical Journal International, 225(3):1554–1585.
- Tang, L. and Fang, X. (2023). Application of six-component ambient seismic noise data for high-resolution imaging of lateral heterogeneities. Geophysical Journal International, 232(3):1756–1784.
- Tang, L., Igel, H., and Montagner, J.-P. (2023a). Anisotropy and deformation processes in southern california from rotational observations. *Geophysical Research Letters*, 50(23):e2023GL105970.
- Tang, L., Igel, H., and Montagner, J.-P. (2023b). Single-point dispersion measurement of surface waves combining translation, rotation and strain in weakly anisotropic media: theory. Geophysical Journal International, 235(1):24–47.
- Tang, L., Igel, H., Montagner, J.-P., Hadziioannou, C., Safarkhani, M., and Vernon, F. L. (2024a). Seasonality of microseisms in southern california from 6c ground motions. *Authorea Preprints*.
- Tang, L., Igel, H., Montagner, J.-P., and Vernon, F. (2024b). Seismic anisotropy from 6c ground motions of ambient seismic noise. *Journal of Geophysical Research: Solid Earth*, 129(6):e2024JB028959.
- Tanimoto, T., Hadziioannou, C., Igel, H., Wasserman, J., Schreiber, U., and Gebauer, A. (2015). Estimate of rayleigh-to-love wave ratio in the secondary microseism by colocated ring laser and seismograph. Geophysical Research Letters, 42(8):2650–2655.
- Tanimoto, T., Hadziioannou, C., Igel, H., Wassermann, J., Schreiber, U., Gebauer, A., and Chow, B. (2016a). Seasonal variations in the Rayleigh-to-Love wave ratio in the secondary microseism from colocated ring laser and seismograph. J. Geophys. Res. Solid Earth, 121(4):2447–2459.
- Tanimoto, T., Ishimaru, S., and Alvizuri, C. (2006). Seasonality in particle motion of microseisms. *Geophysical Journal International*, 166(1):253–266.

- Tanimoto, T., Lin, C.-J., Hadziioannou, C., Igel, H., and Vernon, F. (2016b). Estimate of rayleigh-to-love wave ratio in the secondary microseism by a small array at piñon flat observatory, california. *Geophysical research letters*, 43(21):11–173.
- Tanimoto, T. and Wang, J. (2021). Incorporating wind information in the inversion of co-located pressure and seismic data for shallow elastic structure.

 Journal of Geophysical Research: Solid Earth, 126(5):e2020JB021162.
- Toksöz, M. N. and Lacoss, R. T. (1968). Microseisms: Mode structure and sources. *Science*, 159(3817):872–873.
- Tolman, H. L. (2014). User Manual and System Documentation of WAVE-WATCH III R © Version 4.18. NOAA / NWS / NCEP / MMAB Technical Note 316, 194.
- Tolman, H. L. et al. (2009). User manual and system documentation of wavewatch iii tm version 3.14. *Technical note*, MMAB contribution, 276(220).
- Tsai, V. C. (2009). On establishing the accuracy of noise tomography traveltime measurements in a realistic medium. *Geophysical Journal International*, 178(3):1555–1564.
- Tsai, V. C. (2010). The relationship between noise correlation and the Green's function in the presence of degeneracy and the absence of equipartition. *Geophys. J. Int.*, 182(3):1509–1514.
- Uthaman, M., Singh, C., Singh, A., Jana, N., Dubey, A. K., Sarkar, S., and Tiwari, A. K. (2022). Spatial and temporal variation of the ambient noise environment of the sikkim himalaya. *Scientific Reports*, 12(1):274.
- van Dinther, C., Margerin, L., and Campillo, M. (2021). Implications of Laterally Varying Scattering Properties for Subsurface Monitoring With Coda Wave Sensitivity Kernels: Application to Volcanic and Fault Zone Setting. *Journal of Geophysical Research: Solid Earth*, 126(12).
- Van Trees, H. L. (2002). Optimum array processing: Part IV of detection, estimation, and modulation theory. John Wiley & Sons.

- Vernon, F. (1982). Anza regional network.
- Vernon, F. (2014). Piñon flats observatory array.
- Virtanen, P., Gommers, R., Oliphant, T. E., Haberland, M., Reddy, T., Cournapeau, D., Burovski, E., Peterson, P., Weckesser, W., Bright, J., van der Walt, S. J., Brett, M., Wilson, J., Millman, K. J., Mayorov, N., Nelson, A. R. J., Jones, E., Kern, R., Larson, E., Carey, C. J., Polat, İ., Feng, Y., Moore, E. W., VanderPlas, J., Laxalde, D., Perktold, J., Cimrman, R., Henriksen, I., Quintero, E. A., Harris, C. R., Archibald, A. M., Ribeiro, A. H., Pedregosa, F., van Mulbregt, P., and SciPy 1.0 Contributors (2020). SciPy 1.0: Fundamental algorithms for scientific computing in python. Nature Methods, 17:261–272.
- Wang, Q.-Y. and Yao, H. (2020). Monitoring of Velocity Changes Based on Seismic Ambient Noise: A Brief Review and Perspective. Earth Planet. Phys., 4(5):532–542.
- Wapenaar, K. (2004). Retrieving the elastdynamic green's function of an arbitrary inhomogeneous medium by cross correlation. *Phys. Rev. Lett.*, 93(254301):1–4.
- Wapenaar, K., Draganov, D., Snieder, R., Campman, X., and Verdel, A. (2010).
 Tutorial on seismic interferometry: Part 1—basic principles and applications.
 Geophysics, 75(5):75A195–75A209.
- Wapenaar, K. and Fokkema, J. (2006). Green's function representations for seismic interferometry. *Geophysics*, 71(4):SI33–SI46.
- Wapenaar, K., Fokkema, J., and Snieder, R. (2005). Retrieving the Green's function in an open system by cross correlation: A comparison of approaches (L). *J. Acoust. Soc. Am.*, 118(5):2783–2786.
- Weaver, R. L. and Lobkis, O. I. (2001). Ultrasonics without a source: Thermal fluctuation correlations at mhz frequencies. *Physical Review Letters*, 87(13):134301.

- Weaver, R. L. and Lobkis, O. I. (2004). Diffuse fields in open systems and the emergence of the green's function (l). The Journal of the Acoustical Society of America, 116(5):2731–2734.
- Wegler, U. and Sens-Schönfelder, C. (2007). Fault zone monitoring with passive image interferometry. *Geophysical Journal International*, 168(3):1029–1033.
- Yang, Y. and Ritzwoller, M. H. (2008). Characteristics of ambient seismic noise as a source for surface wave tomography. Geochemistry, Geophysics, Geosystems, 9(2).
- Yao, H. and Van Der Hilst, R. D. (2009). Analysis of ambient noise energy distribution and phase velocity bias in ambient noise tomography, with application to se tibet. *Geophysical Journal International*, 179(2):1113–1132.
- Yao, H., van Der Hilst, R. D., and De Hoop, M. V. (2006). Surface-wave array tomography in SE Tibet from ambient seismic noise and two-station analysis—I. Phase velocity maps. *Geophys. J. Int.*, 166(2):732–744.
- Yates, A., Caudron, C., Lesage, P., Mordret, A., Lecocq, T., and Soubestre, J. (2022). Assessing similarity in continuous seismic cross-correlation functions using hierarchical clustering: Application to Ruapehu and Piton de la Fournaise volcanoes. *Geophysical Journal International*, 233(1):472–489.
- Yuan, S., Gessele, K., Gabriel, A.-A., May, D. A., Wassermann, J., and Igel, H. (2021). Seismic source tracking with six degree-of-freedom ground motion observations. *Journal of Geophysical Research: Solid Earth*, 126(3):e2020JB021112.
- Zeng, X. and Ni, S. (2010). A persistent localized microseismic source near the Kyushu Island, Japan. *Geophysical Research Letters*, 37(24).
- Zhang, J., Gerstoft, P., and Shearer, P. M. (2010). Resolving p-wave travel-time anomalies using seismic array observations of oceanic storms. *Earth and Planetary Science Letters*, 292(3-4):419–427.

- Zhang, R., Boué, P., Campillo, M., and Ma, J. (2023). Quantifying P-wave Secondary Microseisms Events: A Comparison of Observed and Modelled Backprojection. *Geophys. J. Int.*, 234(2):933–947.
- Zhang, S., Feng, L., and Ritzwoller, M. H. (2020). Three-Station Interferometry and Tomography: Coda versus Direct Waves. *Geophys. J. Int.*, 221(1):521–541.
- Ziane, D. and Hadziioannou, C. (2019). The contribution of multiple scattering to love wave generation in the secondary microseism. Geophysical Journal International, 217(2):1108–1122.